Relative Cross Section Measurement of the Inclusive Charged Current Multiple Pion Production to Inclusive Charged Current from ν_μ at the Near Detector of the T2K Experiment

Scott Davis

A dissertation
submitted in partial fulfillment of the
requirements for the degree of

Doctor of Philosophy

University of Washington

2014

Reading Committee:

Richard J. Wilkes, Chair

Jason Detwiler

Nikolai Tolich

Program Authorized to Offer Degree:
Physics

University of Washington

Abstract

Relative Cross Section Measurement of the Inclusive Charged Current Multiple Pion Production to Inclusive Charged Current from ν_μ at the Near Detector of the T2K Experiment

Scott Davis

Chair of the Supervisory Committee:
Professor Richard J. Wilkes
Physics

The Tokai-to-Kamiokande (T2K) experiment is an off-axis, long baseline neutrino oscillation experiment based in Japan. One of the largest sources of systematic uncertainty in the oscillation analysis is the uncertainty on neutrino cross sections. In this thesis, we use the π^0 detector (PØD) of the T2K Near Detector to measure one cross section of muon neutrinos. The PØD is a scintillator based detector with a precision water target which allows for a measurement with water and without water. In particular, we measured the relative cross section of charged current multiple pion production to inclusive charged current production. The analysis is performed with a multi-variate template fit using two Monte Carlo neutrino generators, NEUT and GENIE. The relative ratio for NEUT(GENIE) is $0.126 \pm 0.024^{+0.022}_{-0.021}(0.100 \pm 0.018^{+0.018}_{-0.017})$ for the Water-In configuration and $0.104 \pm 0.029^{+0.030}_{-0.035}(0.121 \pm 0.021^{+0.034}_{-0.036})$ for the Water-Out configuration. The prospects for a precision water cross section measurement are also discussed.

TABLE OF CONTENTS

LIST OF FIGURES

LIST OF TABLES

ACKNOWLEDGMENTS

Many people were involved in support of this thesis. An obvious starting point is the many people involved in the T2K collaboration. Many software and hardware components were constructed by many different people which may not have a direct role on an analysis, but indirectly support the entire experiment. Without the work of all members, there would be no beam, no detectors, no Monte Carlo, and no analysis software. In addition, I would like to thank that various members of the PØD group who helped construct the PØD and provided support. Many people were involved in construction and design of the PØD water system as well as helping with my analysis. I would like to thank Bruce Berger, Dmitriy Beznosko, Kevin Connolly, Chang Kee Jung, Kendall Mahn, Kevin McFarland, Dan Ruterboris, Ian Taylor, Walter Toki, Tomasz Wachala, and Alfons Weber for their help with my analysis. I would like to thank Bruce Berger, Hans Berns, Norm Buchanan, Alex Clifton, Kevin Connolly, Mike Dziomba, Dave Forbush, Damon Hansen, James Imber, Jay Hyun Jo, Rob Johnson, Alysia Marino, Clark McGrew, Vittorio Paolone, Paul Rojas, Walter Toki, and Dave Warner for their help with the PØD water system, both in technical design, support, and labor over the years. In particular, I would like to thank Toshifumi Tsukamoto for being our liason with the facility management. I would also like to thank Tim Durkin, Nick Hastings, Phil Litchfield, and Roberto Sacco for making life in Tokai more intresting during the long trips. I would like to offer special thanks to my advisor, Jeff Wilkes, for all his support over the years and for offering me the chance of a lifetime. Finally, I would like to thank my family and friends for their support through the many years to help me continue on to my goal. In particular, I would like to thank Shannon for putting up with my long hours working in seattle or traveling to Japan.

DEDICATION

To my grandfather, Frank

Chapter 1

INTRODUCTION

Occasionally in particle physics, an oddity can lead to a large discovery which creates a rich field to explore. A small discrepancy in a model or experiment can lead to more experiments with better precision which can lead to finding cracks in the current understanding of physics leading to new ideas about the operation of the universe. Neutrinos offer a good example starting from a particle proposed to preserve energy and momentum in beta decays but later evolving into complex particles whose interactions could have profound implications on matter formation.

Neutrinos are one of the core particles in the Standard Model (see Figure 1.1). In the minimal model, neutrinos are represented as massless particles which are coupled to leptons. Neutrinos interact only through the weak interactions and have a very small cross section. Because of the low rate of interactions, neutrino went undetected and unknown until the middle of the 20th century. Once neturinos were discovered, additional experiments near the end of the 20th century have discovered that neutrinos do actually have a small amount of mass. This discovery has lead to the possiblity of CP violation in neutrino interactions and opened to door to many other questions about the property of neutrinos.

Neutrinos were first proposed in December 1930 by Wolfgang Pauli. At the time, nuclear beta decay was known in which a nucleus transition to one with a lower mass while emitting an electron which should have a specific energy. However, experiments found the electron had a spectrum of kinetic energy which was less than expected from a simple decay to two-bodies (see Figure 1.2(a)). As a solution, Pauli proposed that instead of a two-body decay, there was a third particle which would be a light, neutral particle. This particle was named neutrino by Enrico Fermi in 1934[44] because the heavier neutron had been found by James Chadwick in 1932. Fred Reines and Clyde Cowan later discovered the electron neutrino using inverse beta decay measured at Savannah River reactor in 1956[37]. This

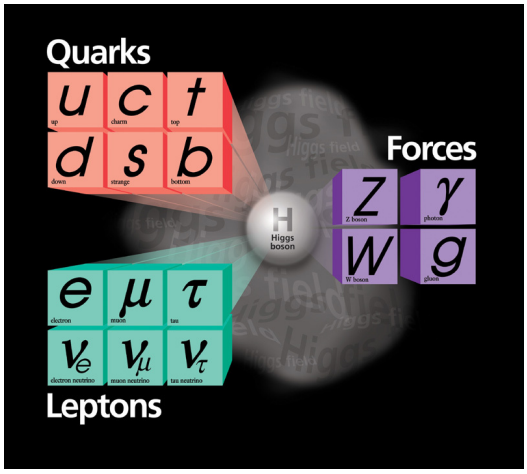

Figure 1.1: The Standard Model (image courtesy of Fermilab Visual Media Services)

lead to experiments at Brookhaven National Laboratory that examined if neutrinos from pion decay would also cause inverse beta decay in 1962[38]. These experiments lead to the idea that neutrinos were associated with a certain lepton flavor, such as electron, muon, or later tau. Upon the discovery of the particles associated with the weak force, $W^{\pm}$ and Z^0, becay decay could be fully understood (see Figure 1.2(b)).

Initially, the neutrino was thought to have a degenerate mass and flavor state, resulting in stable flavor states. However, observations using a Chlorine experiment located in the Homestake mine in South Dakota[40][39][36] questioned this interpretation. This experiment looked for the conversion of chlorine to argon via inverse beta decay in order to measure the flux of neutrinos coming from the sun. The experiment found a deficiency in electron neutrinos compared to expectations. This issue was resolved by Super-Kamiokande in 1998[47] and Sudbury Neutrino Observatory (SNO) in 2001[18] with the discovery of neutrino oscillation. Super-Kamiokande discovered that muon neutrinos coming from the atmosphere were oscillating into different flavors based on the distance traveled while SNO found the total solar neutrino flux was as predicted, but that the electron neutrino flux was less than expected, showing that electron neutrino were oscillating to other neutrinos.

Neutrino oscillation is predicated on the mass eigenstates and flavor eigenstates not be-

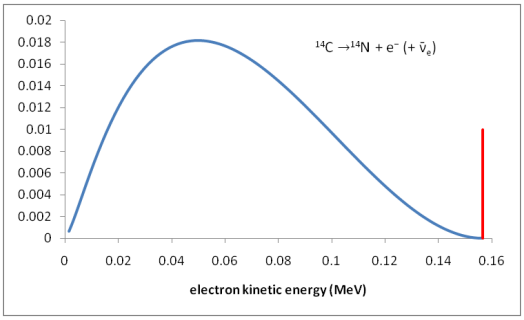

(a) Energy of the electron from beta decay. The red line represents the energy without a neutrino while the blue curve represents the energy distribution with a neutrino.

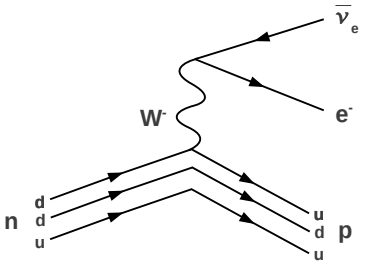

(b) Feynmann diagram of Beta Decay

Figure 1.2: Beta Decay

ing simultaneous eigenstates of the Hamiltonian. Whereas the weak interaction interacts with the flavor state, a flavor state is a superposition of mass eigenstates. This oscillation parametrization was first proposed by Pontecorvo[68][69] and expanded on by Maki, Nakagawa, and Sakata[63] as a unitary matrix transformation from the mass eigenstates to flavor eigenstates in a similar fashion to quark mixing. The transformation for neutrinos is shown in Equation 1.1 in which α corresponds to the flavor state while i corresponds to the mass state. This matrix (PMNS matrix), shown in Equation 1.2 allows mixing between the two states through the off diagonal elements. The PMNS matrix is parametrized by three angles, θ_{12}, θ_{13}, θ_{23}, a CP violation phase, δ, and two Majorana phases, α_1 and α_2. The value of δ determines the amount of CP violation in the neutrino sector, while the value of the Majorana phases can change the rate of certain decays, such as neutrino-less double beta decay.

$$|\nu_\alpha\rangle = \sum_i U_{\alpha i} |\nu_i\rangle \tag{1.1}$$

$$U = \begin{pmatrix} 1 & 0 & 0 \\ 0 & \cos\theta_{23} & \sin\theta_{23} \\ 0 & -\sin\theta_{23} & \cos\theta_{23} \end{pmatrix} \times \begin{pmatrix} \cos\theta_{13} & 0 & \sin\theta_{13}e^{-i\delta} \\ 0 & 1 & 0 \\ -\sin\theta_{13}e^{i\delta} & 0 & \cos\theta_{13} \end{pmatrix} \times \begin{pmatrix} \cos\theta_{12} & \sin\theta_{12} & 0 \\ -\sin\theta_{12} & \cos\theta_{12} & 0 \\ 0 & 0 & 1 \end{pmatrix} \times \begin{pmatrix} e^{i\alpha_1/2} & 0 & 0 \\ 0 & e^{i\alpha_2/2} & 0 \\ 0 & 0 & 1 \end{pmatrix} \tag{1.2}$$

The probability of a neutrino of flavor α oscillating to flavor β after traveling a given distance, L, and with energy, E, is given in Equation 1.3 assuming ultrarelativistic neutrinos and a neutrino mass, m_j. The probability is a function of the parameters of the PMNS matrix as well as the neutrino energy, E, the distance the neutrino traveled, L, and the difference between the square of the mass as defined in Equation 1.4. Matter effects such as the MSW effect[82][65] can affect oscillation by changing the "effective" mass of the neutrino through weak coupling with dense enough matter as seen in the sun. Note that the majorina phase has no effect on neutrino oscillation, while the CP violation phase can change the oscillation probability.

$$|\langle\nu_\beta|\nu_\alpha\rangle|^2 = |\sum_j U^*_{\alpha j} U_{\beta j} e^{-im_j^2 L/2E}|^2 \tag{1.3}$$

$$\Delta m^2_{ij} = m^2_i - m^2_j \tag{1.4}$$

If the distance from a production point of a neutrino flavor is known, and the energy measured, then the parameters can be measured by looking at either the appearance or disappearance of certain neutrinos. An example of the probability of survival is shown in Equation 1.5[7] and the probability of appearance is shown in Equation 1.6[9]. In both equations, small extra terms such as the solar term and matter effect are suppressed.

$$P(\nu_\mu \to \nu_\mu) \simeq 1 - 4\cos^2\theta_{13}\sin^2 2\theta_{23}[1 - \cos^2\theta_{13}\sin^2\theta_{23}]\sin^2\frac{|\Delta m^2_{23}|L}{4E} \tag{1.5}$$

$$P(\nu_\mu \to \nu_e) \simeq \sin^2\theta_{23}\sin^2 2\theta_{13}\sin^2\frac{|\Delta m^2_{13}|L}{4E} - \frac{\sin 2\theta_{12}\sin 2\theta_{23}}{2\sin\theta_{13}}\sin\frac{|\Delta m^2_{12}|L}{4E}\sin^2 2\theta_{13}\sin^2\frac{|\Delta m^2_{13}|L}{4E}\sin\delta_{CP} \tag{1.6}$$

One way to measure an oscillation parameter is to fit the measured data, either number of events or a spectrum, to a model which is dependant on the oscillation paramter. The fit can be used to determine the best fit point and error contours. However, there are many elements that have to go into the predictive model such as the knowledge of the neutrino flux, any background processes which may simulate the data, and detector efficencies. One example is the uncertainity in the model's description of cross sections. For example, in Super-Kamiokande, a ν_μ may interact with water and produce a single π^0. The π^0 will decay into two photons. If one of the photons is not detected, this event may appear to be an ν_e event due to the appearance only only one electron. The uncertainity of the model's cross section of this event leads directly into an uncertainty in the size of the expected background, which can affect the total spectrum or number of predicted ν_e events. To give an example, the total systematic error in T2K's ν_e appearance measurement in 2011[3] was 17.5% (for $\sin^2 2\theta_{13}$ of 0.1) with the cross section systematic error being the largest error of 10.5%. T2K's ν_e appearance measurement in 2012[6] was 10.0% with the cross section systematic error of 7.7%. The smaller errors were due to several analysis improvements including a combined fit using external data sources, flux measurements, and cross section measurements in the experiement. However, the cross section uncertainty was still the largest systematic error.

One additional complication from neutrino oscillation measurements is that the energy of the neutrino must be known. However, it is currently not possible to produce a mono-energetic neutrino beam, so instead the neutrino energy must be measured. Because this is a measurement, the detector effects must be unfolded or accounted for. In addition, the neutrino cross sections need to be well understood in order to understand how a neutrino interacts with a detection medium. For example, neutrino interactions inside nuclei need better measurements in order to correctly compensate for nuclear interactions in order to determine neutrino energy.

The easiest way to determine a neutrino energy is to do a calorimetric measurements of neutrino interactions in which all particles are contained. However, this is not often practical, so most experiments look for simple interactions to allow for kinematic reconstruction of the neutrino energy. For example, one way to measure a neutrino energy is to look for an event in which the neutrino converts into its paired lepton (charge current interaction) with either no visible outgoing particles or a well reconstructed proton track. If one assumes an elastic interaction and assuming that the proton recoil is very small, one can reconstruct the neutrino energy from the lepton kinematics. However, if there are multple nucleons ejected, or there are interactions inside the nucleus which can mask pion production, then there may be missing energy which will give the wrong reconstructed neutrino energy. In order to improve the neutrino energy measurements needed for oscillation measurements, improved cross sections measurements on different media are needed.

Modern neutrino oscillation experiments often use a pair of detectors, one nearby the production point and one further away, in order to reduce systematics by making similar measurements at both detectors. In addition, the near detector for an experiment can also be used for cross section measurements as the neutrino flux is higher closer to the production point. By using the same beam, the cross section measurements will sample approximately the same energy spectrum that the oscillation analysis samples. This allows for cross section measurements that are similar at the near and far detector.

This thesis will discuss one such oscillation experiment, the T2K experiment. As part of the T2K experiment, a near detector was constructed which contains several sub-detectors which were designed to measure cross sections. One sub-detector, the PØD, was designed to detect neutrino interactions on water. Because the far detector for T2K is Super-Kamiokande, which is a water Cherenkov detector, cross section measurements on water are needed. As part of the construction of the PØD, a target water system was designed to measure the water mass to 1%. Using the PØD, we measured one specific cross section, the production of multiple pions from ν_μ interactions. Specifically, we measured the relative ratio of charged-current inclusive multiple pion production to charged-current inclusive production. Further details are explained in the following chapters.

Chapter 2

OVERVIEW OF THE T2K EXPERIMENT

2.1 Introduction

This chapter presents an overview of the T2K experiment[4]. The T2K experiment is a long-baseline, off-axis neutrino oscillation experiment that is based in Japan. The experiment was designed to look for ν_e appearance in a ν_μ beam. ν_e appearance is coupled to the last unknown mixing angle, θ_{13}. In addition, the experiment can look for ν_μ disappearance which is coupled to θ_{23} and $|\Delta m^2_{23}|$. θ_{23} and $|\Delta m^2_{23}|$ and known from several other experiments[13][81] with the best fit value for θ_{23} being maximal[32].

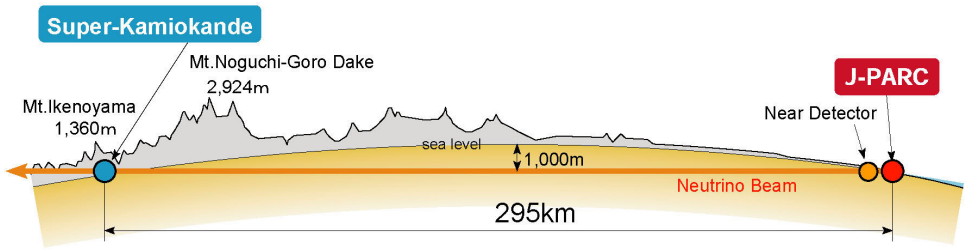

(a)

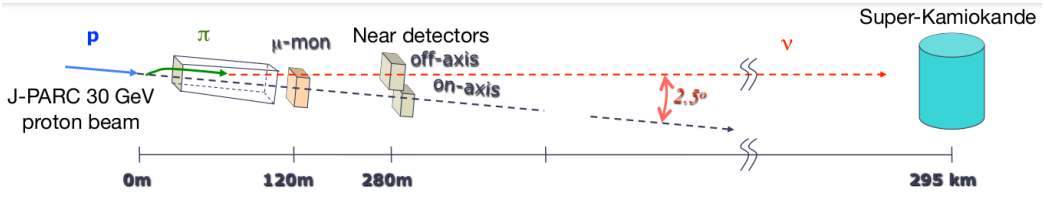

(b)

Figure 2.1: Schematic of the T2K experiment. Image courtesy of the T2K collaboration.

The T2K experiment consists of three separate components: the neutrino beamline, the near detector complex (ND280), and the far detector (Super-Kamiokande) as shown

Figure 2.2: Pictorial Schematic of the T2K experiment. Image courtesy of the T2K collaboration.

in Figures 2.1 and 2.2. The beamline and near detector complex are located in Tokai-mura in the Ibaraki prefecture in Japan while the far detector is located in Hida-shi in the Gifu prefecture in Japan. In general, neutrinos are produced in the beamline from pion decay in which the pions are created by bombarding a target with protons. The pions are "focused" using magnets in order to produce a neutrino beam consisting of mostly ν_μ. A near detector complex is used to measure several neutrino beam parameters, measure neutrino cross sections, and to measure the data to Monte Carlo ratio. This complex, which is 280 meters from the target, consists of two detectors, ND280-OA and INGRID[1]. Approximately 295 kilometers from the target is the far detector, Super-Kamiokande. One could measure the number of ν_e observed at the far detector and compare to the predicted number based on different θ_{13} values and the predicted ν_μ flux in order to find the best value of θ_{13}.

[1]The near detector complex is called ND280 which consists of two sub-detectors. One of the subdetectors is called the ND280 off-axis detctor, ND280-OA. Note that ND280 refers to the complex while ND280-OA refers to one sub-detector in the complex

2.2 Beamline

This section presents an overview of the neutrino beamline[74, 57, 55]. The neutrino beamline follows the standard strategy used in most long-baseline neutrino experiments. Neutrinos are produced by bombarding a target with protons in order to produce $\pi^{\pm}$s. The $\pi^{\pm}$s decay mainly into muons, ν_μ, and $\bar{\nu}_\mu$ depending on the pion charge. Magnet fields are used to focus the preferred charged pions and defocus the others to attempt to make a pure beam. Hadrons and muons with less than 5 GeV of momentum are stopped by a beam dump while higher momentum hadrons and muons continue beyond the dump before decaying. Muons from the pions also decay into ν_μ and $\bar{\nu}_e$ or $\bar{\nu}_\mu$ and ν_e as well. These neutrinos, as well as neutrinos coming from kaons which may be produced at the target, represent a background ν_e flux which must be understood and accounted for. This background is constrained by using Monte Carlo as well as measurements done in other experiements[11] and experiments using the near detector complex.

As mentioned in Chapter 1, the probability of appearance and disappearance is a factor of distance traveled over neutrino energy. The distance between the neutrino production point and the far detector is fixed, so there exists a certain neutrino energy which would maximize neutrino oscillation. Due to relativistic kinematics, the neutrinos from the pion decay have a lower maximum allowed energy as the decay neutrino travels at a larger angle from the direction of the parent pion. In other words, as one looks at neutrinos which are traveling at a larger angle from the parent pion, the mean neutrino energy will be lower. This effect is shown in Figure 2.3 in which the on-axis beam (neutrinos which travel in the direction of the pion) at the T2K experiment have a peak energy around 1.0 GeV while neutrinos that are 2.0 ° off-axis have a peak around 0.8 GeV and neutrinos that are 2.5 ° off-axis have a peak energy around 0.6 GeV. Note that the energy distribution narrows as one goes further off-axis, but the flux also decreases as well. As the probability of ν_μ survival has a minimum at 0.6 GeV at 295 km, the T2K experiment is designed so that the far detector samples neutrinos which are 2.5 ° off-axis. The T2K experiment is the first experiment designed to use the off-axis part of the neutrino beam.

Pions in the T2K beamline are produced by bombarding a graphite target with 30

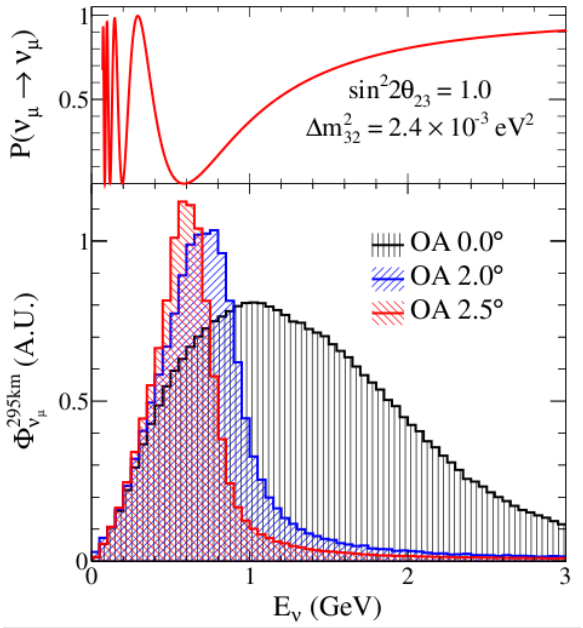

Figure 2.3: Upper plot represents the probability of ν_μ survival as a function of neutrino energy with a fixed distance while the lower plot represents ν_μ flux as a function of neutrino energy at Super-Kamiokande for the on-axis beam, 2.0 ° and 2.5 ° off-axis. Image courtesy of the T2K collaboration.

GeV protons produced by the Japan Proton Accelerator Research Complex (J-PARC). J-PARC[4] is a multi-use facility designed to supply high and low energy protons to various experiment complexes as shown in Figure 2.4(a). The proton beam starts off as H^- ions which are accelerated by a linear accelerator (LINAC) up to 400 MeV. The ions are then stripped by foils to protons and enter a Rapid-Cycling Synchrotron (RCS) which accelerates the protons up to 3 GeV. At this point, 5% of the beam is supplied to the Main Ring (MR) while the rest go to the Material and Life Science Facility (MLF) for low energy experiments. The MR accelerates the protons up to 30 GeV. At this point, there are eight bunches in the ring (six before June 2010). A spill is defined as a set of eight bunches, and there are approximately 3×10^{14} protons per spill with a spill width of approximately 5 μsec with 2 seconds between spills.

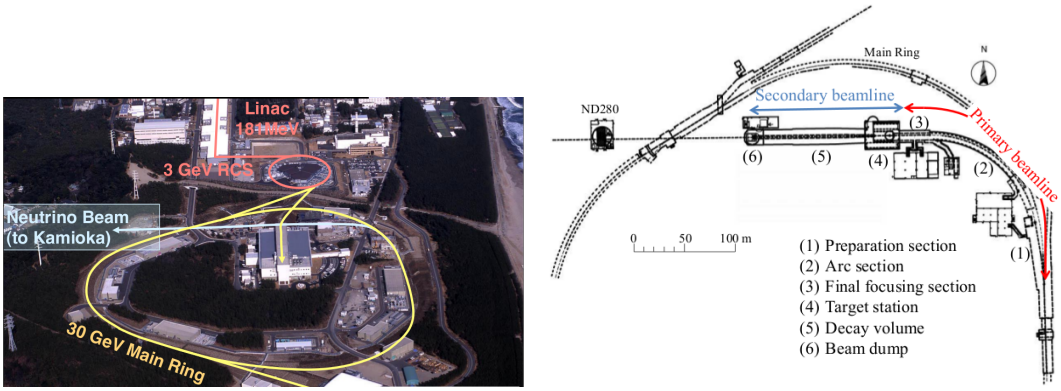

(a) Image of J-PARC showing the LINAC, RCS, and MR

(b) Schematic of the T2K neutrino beamline

Figure 2.4: J-PARC and T2K beamline. Image courtesy of the T2K collaboration.

Using a set of kicker magnets, a spill is extracted into the neutrino beamline shown in Figure 2.4(b). The proton beam is guided to the secondary beamline which contains the target. The beamline uses a combination of normal conducting magnets, superconducting steering magnets, and superconducting combined function magnets (SCFMs) in order to steer the beam. Along the beamline are a series of beam monitors such as current transformers (CTs), electrostatic monitors (ESMs), segmented secondary emission moni-

tors (SSEMs) and beam loss monitors (BLMs). These detectors measure parameters such as beam intensity, position, profile, and loss. The University of Washington was responsible for supplying a series of 160 MHz Flash ADC boards in order digitize the pulse area from these sensors.

The secondary beamline is a helium filled vessel which contains the target, a series of magnetic horns, and an optical transition radiation monitor (OTR). The secondary beamline is approximately 1500 m^3, cooled with water through coils on the surface of the vessel, and filled with helium at atmospheric pressure in order to prevent pion absorption as well as production of tritium and NO_x. The proton beam can be monitored before hitting the target by using the OTR. The OTR is a foil that can be placed in the beamline with the incidental light observed for the beam profile. The target is a 914 mm long, 26 mm diameter cylinder made of graphite in a 0.3 mm thick titanium case. The target is cooled by the helium gas and is located in the bore of the first magnetic horn. There are three magnetic horns designed to focus one polarity of charge pions and defocus the other. The horns are made of an aluminum alloy with the conductor as thin as possible to avoid pion absorption, but still remain rigid while under a maximum design of 320 kA operation corresponding to 2.1 T. Currently, the horn operates at 250 kA due to the Main Ring operating below the maximum design power. At the end of the secondary beamline is a beam dump and a muon monitor using ionization chambers and silicon photodiodes in order to observe the muon direction from the decayed pions.

One important element of the T2K neutrino beamline is the GPS time synchronization system. A custom Local Time Clock (LTC) board uses a commercial Rubidium clock as a time base and uses two independent GPS receivers as a reference. With this system, a time stamp is associated to each spill. An identical system exists at the far detector, Super-Kamiokande. The time and spill information is sent to Super-Kamiokande which uses the time of the spill in order to establish a window during data taking in which a neutrino from J-PARC may arrive and interact. Using this GPS timing effectively removes cosmic ray backgrounds at Super-Kamiokande because of the very small window, 1 msec, in which to look for events from J-PARC compared to the 2 second delay between spills. This system is accurate to about 50 nsec, but the system is being upgraded using improved GPS elements

and a Cesium clock in order to get accuracy to a few nsec for neutrino time of flight (ToF) measurements. The University of Washington was responsible for a similar system deployed in K2K, an earlier experiment using a neutrino beam from Tsukuba to Super-Kamiokande in Japan, and continues maintaining and expanding the GPS system for T2K.

2.3 Near Detector Complex

The near detector complex contains two suites of detectors designed to monitor neutrino beam energy, direction, and overall quality as well as constrain Monte Carlo predictions as well as measure cross sections to limit backgrounds. This complex is explained in full detail in chapter 3.

2.4 Super-Kamiokande

This section presents an overview of Super-Kamiokande[48]. Super-Kamiokande is a 50 kTon water Chrenkov detector about 1 km under Mt. Ikenoyama, 295 km west of J-PARC. The detector is in a cylindrical cavern which is 41 m deep and has a 39 m diameter as shown in Figure 2.5(a). The interior is divided into an inner detector (ID) and outer detector (OD). The ID is centered at the center of the cavity and is 36.2 m high with a diameter of 33.8 m. The OD surrounds the ID and is about 2 m thick. The ID has 11,129 inward-facing 50 cm diameter photo-multiplier tubes (PMTs) while the OD has 1,885 outward-facing 20 cm diameter PMTs. The ID has 40% PMT coverage while the OD has less than 1%. However, the OD is designed to act as a veto while the ID is designed to have enough resolution to measure physical quantities. The two detectors are separated by a stainless steel structure in which the inner surface (facing the ID) is lined with black plastic to prevent scattering while the outer surface (facing the OD) is lined with reflective Tyvek® in order to increase the light yield for the OD. During the T2K running periods, Super-Kamiokande was in the SK-IV configuration. This configuration corresponds to a fully instrumented detector with upgraded PMT electronics which removes DAQ deadtime.

Super-Kamiokande detects particles by looking for Chrenkov radiation coming from charged particles traveling above the Chrenkov threshold. The radiation is emitted in a cone centered on the particle's path with an angle from the path depending on the velocity

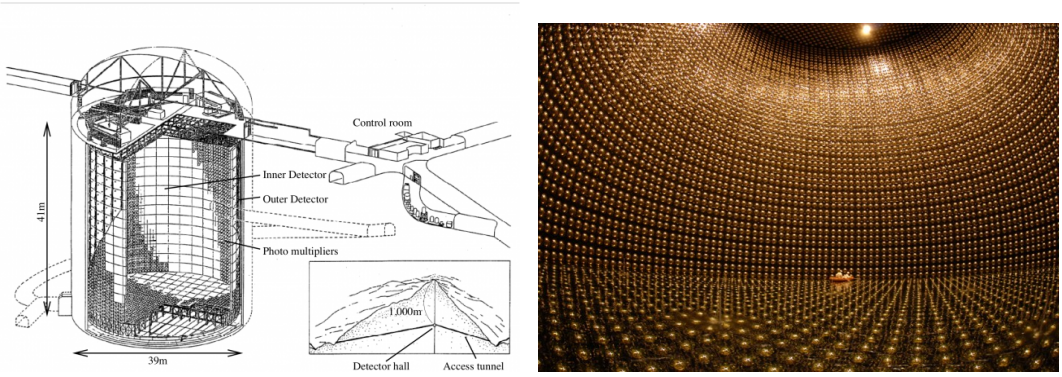

(a) Super-Kamiokande Schematic (b) Photo of the interior of Super-Kamiokande

Figure 2.5: Super-Kamiokande. Image courtesy of the T2K collaboration.

of the particle as shown in Figure 2.6(a). This angle is often used for velocity or energy measurements or used for Particle ID. One way to determine a particle's identification is to look at the shape of the Chrenkov cone. For example, a muon tends to travel in a relatively straight path while an electron has a higher probability of scattering due to the mass difference between the two particles. This results in a muon having a very clean ring, while an electron's erratic path creates a "fuzzy" ring as shown in Figure 2.6(b).

The dominant interaction of neutrinos from J-PARC in Super-Kamiokande is the Charged-Current Quasi-Elastic (CCQE) interaction. In this interaction, the neutrino interacts with a nucleon and converts to the associated lepton. By using the sharpness of the ring, Super-Kamiokande can be used to distinguish if these leptons are muons or electrons and can determine the flavor of neutrino which is reaching Super-Kamiokande from J-PARC.

2.5 Current Results

The T2K experiment started data taking in January of 2010 and continues to collect data with total beam power increasing with every year as shown in figure 2.7. Data taken from January of 2010 until March 2011 was analyzed and results were first announced on June 15 of 2011. The results indicated that θ_{13} was non-zero with a confidence of 2.5 σ as 6 ν_e events were found when 1.5$\pm$0.3 ν_e events were expected with θ_{13} equal to zero[3]. This was

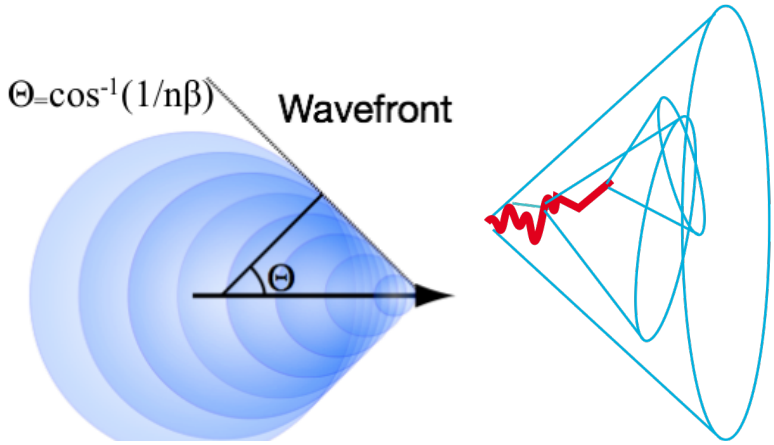

(a) Diagram showing a representation of the Chrenkov light cone.

(b) Diagram showing a "fuzzy" ring due to multiple light cones from electron scattering.

Figure 2.6: Chrenkov Radiation Diagrams. Image courtesy of the T2K collaboration.

the first indication of ν_e appearance from a ν_μ beam. This result was confirmed with $\bar{\nu}_e$ disappearance from reactor experiments such as Daya Bay[23] and RENO[19] experiments in 2012.

Due to the Great Tohoku Earthquake, data taking was delayed until the spring of 2012, but with additional data, results were also announced in the summer of 2012 in which 11 ν_e events were found when 3.2±0.4 ν_e events were expected with θ_{13} equal to zero[6]. This result indicated that θ_{13} was non-zero with a confidence of 3.1 σ resulting in the first evidence of ν_e appearance in a ν_μ beam.

On July 19, 2013, results were released using data taken until April 2013. With this additional data, 28 ν_e events were found when when 4.9±0.6 ν_e events were expected with θ_{13} equal to zero[9]. This result indicated that θ_{13} was non-zero with a confidence of 7.3 σ resulting in the first clear observation ($> 5\ \sigma$) of ν_e appearance in a ν_μ beam. The possible values of θ_{13} as a function of δ_{CP} are shown in Figure 2.8(a). In addition, by combining this result with the results fro other experiments and marginalizing θ_{13}, θ_{23}, and $|\Delta m^2_{23}|$, one

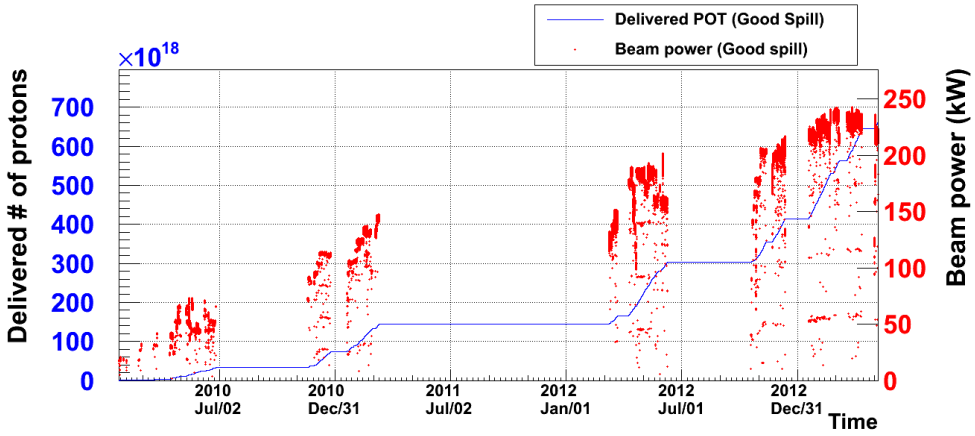

Figure 2.7: Amount of Data Collected. The total accumulated data in Protons-On-Target (POT) is represented on the left axis while the right axis represents the beam power in Kilowatts. Image courtesy of the T2K collaboration.

can find the best fit value for δ_{CP} as shown in Figure 2.8(b). The most recent data tends to favor a δ_{CP} of $-\frac{\pi}{2}$ although a δ_{CP} of 0 is allowed.

In addition to ν_e appearance, T2K can measure ν_μ disappearance as well. The first results were announced in the summer of 2012[5] which can be compared to measurements made by using $\nu_\mu$from the atmosphere and the MINOS experiment. With additional data from 2013, refined results were announced in 2013[7]. The contours for $\sin^2(2\theta_{23})$ and $|\Delta m^2_{23}|$ are shown in Figure 2.9(a) and the reconstructed energy spectrum for the data, no oscillation hypothesis, and best fit are shown in Figure 2.9(b).

2.6 Future Plans

With precision measurements of θ_{13}, the initial goal of T2K is resolved, but there are many other measurements that can be improved on or simply have not been attempted. The obvious measurement is to determine δ_{CP} as θ_{13} is not small. δ_{CP} enters into the probability of ν_e appearance as well as a difference between ν_e and $\bar{\nu}_e$ appearance as a small correction.

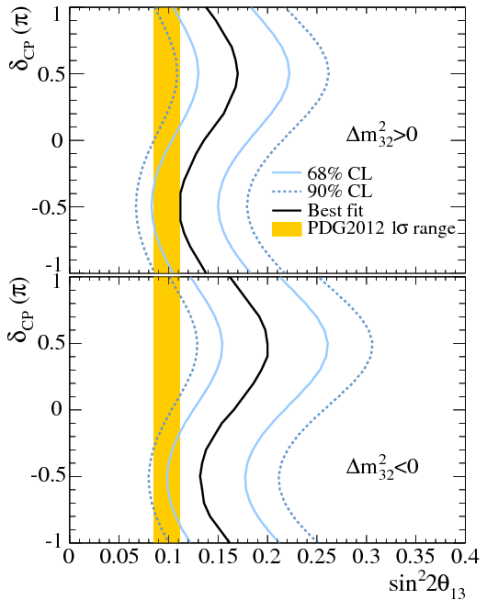

(a) θ_{13} contours as a function of δ_{CP}.

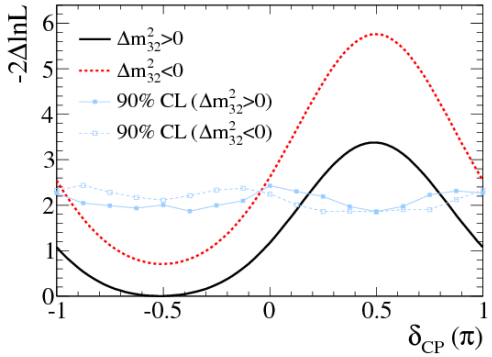

(b) Change in Best Fit Likelihood as a function of δ_{CP}. 90% confidence levels found using the Feldman-Cousins method[43]

Figure 2.8: Results of ν_e appearance released in 2013.

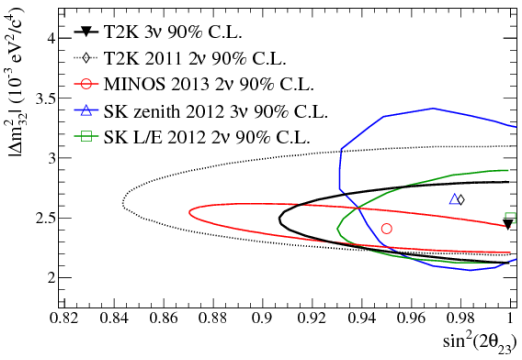

(a) $\sin^2(2\theta_{23})$ Contours

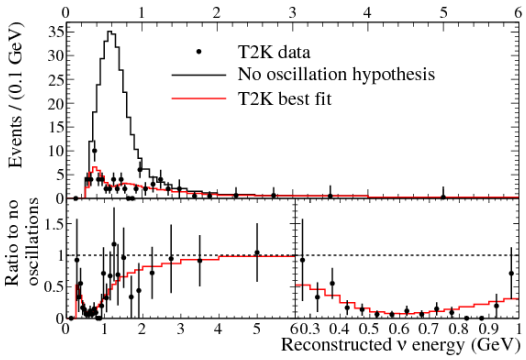

(b) ν_μ Reconstructed Energy Spectrum

Figure 2.9: $\nu_\mu$disappearance results in 2013.

Because the ν_μ beam comes from selecting the appropriate $\pi^\pm$ using magnetic horns, T2K can produce a beam of either ν_μ or $\bar{\nu}_\mu$. The T2K collaboration is working on a plan to mix ν_μ and $\bar{\nu}_\mu$ beam time in order to look for oscillation differences as well as a plan to work with other experiments, such as NOνA[31] in order to perform a joint fit to not only examine δ_{CP} but also which octant θ_{23} is in. Future upgrades of T2K, such as T2KK[53] using Hyper Kamiokande[2], would use higher beam power and may have a second far detector to look for differences between oscillation maxima to help look for δ_{CP} corrections.

In addition, neutrino cross sections are not well understood at various energies, especially anti-neutrino cross sections. Measurement of various neutrino interactions on various materials will give a clearer understanding of these cross sections as well as probe nuclear and hadronic physics since these neutrino interactions take place inside nuclei.

Chapter 3

OVERVIEW OF NEAR DETECTOR COMPLEX

This chapter presents an overview of the near detector complex[76]. This includes two suites of detectors, INGRID and the off-axis near detector (ND280-OA) which are both located in a 17.5 meter diameter, 37 meter deep pit shown in Figure 3.1(a). ND280-OA consists of a set of sub-detectors including the Pi-Zero Detector (PØD)[30], a set of three Time Projection Chambers (TPCs)[12], a set of two Fine-Grained Detectors (FGDs)[21], a set of Electron Calorimeters (ECals), and the Side Muon Range Detector (SMRD)[27]. All sub-detectors are located in the former UA1 magnet[28][29] which was donated from CERN and provides a 0.2 T magnetic field. The sub-detectors are shown in Figures 3.1(b) and 3.2 in which the UA1 magnet is opened. The two detectors in the pit are aligned so that the center of the INGRID is aligned with the on-axis neutrino beam while ND280-OA is aligned with the off-axis neutrino beam that is directed at Super-Kamiokande.

3.1 Detector Technology

In the detectors in the near detector complex, two different technologies are in use in order to detect particles. Part of ND280-OA is a set of three Time Projection Chambers (TPCs), which are explained in Section 3.5 while all other detectors use scintillators and light detection technology. The scintillator detectors in ND280-OA and INGRID are mostly based on using plastic scintillator bars with wavelength-shifting (WLS) fibers which run to a photodiode. The photodiode is connected to a capacitor which is read out by the DAQ. INGRID, PØD, FGD, and the ECals use extruded polystyrene bars doped with 1% PPO and 0.03% POPOP by weight which produces a peak emission light of 420 nm. The bars are coated with a thin coating of polystyrene with 20% TiO_2 in order to reflect light into the bar to maximize collection into the WLS fibers. The SMRD scintillator is similar, but has a different shape as it must fit in narrow slots inside the UA-1 magnet. The SMRD

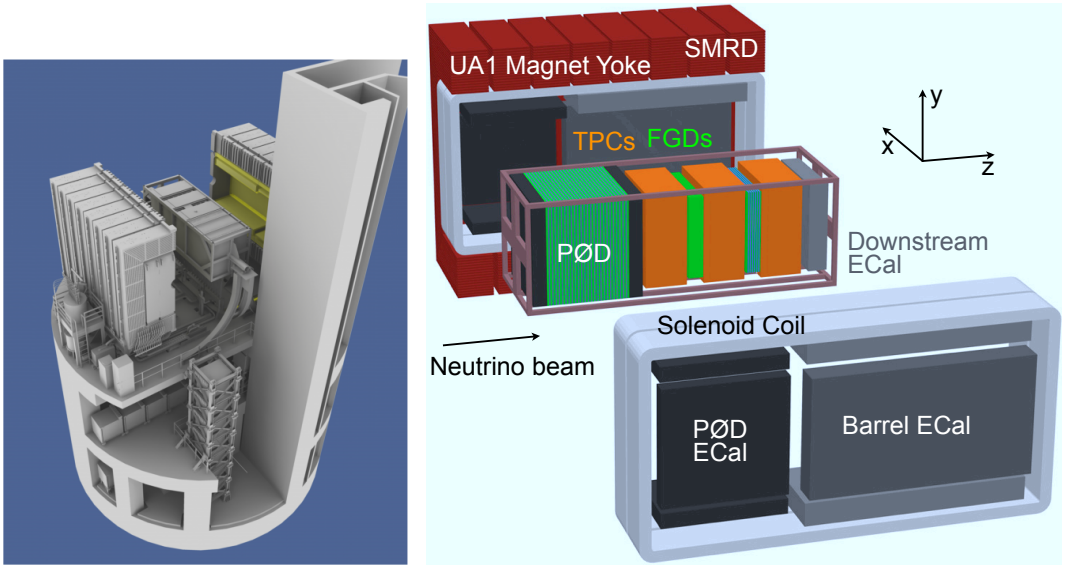

(a) Model of the Near Detector Complex. The neutrino beam starts roughly from the lower right corner of the picture and goes to the upper left corner.

(b) ND280-OA Schematic.

Figure 3.1: Near Detector Complex and ND280-OA. Image courtesy of the T2K collaboration.

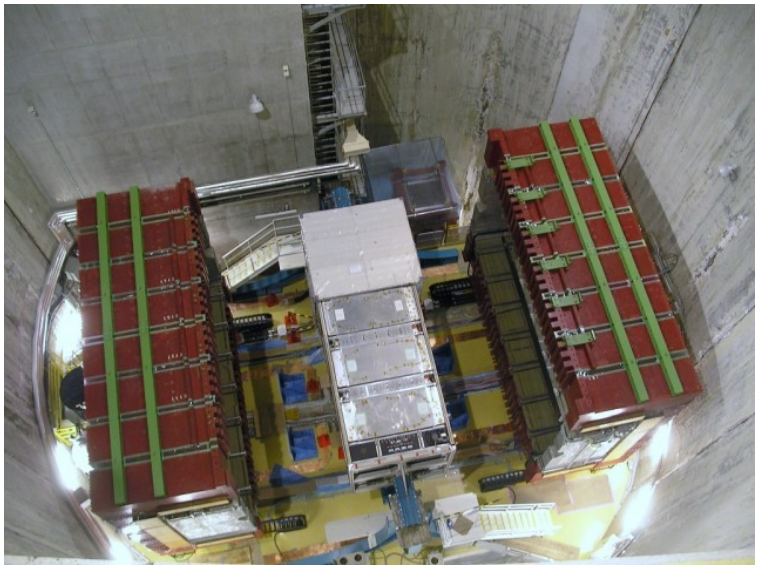

Figure 3.2: Picture of ND280-OA from above with the magnet open. The neutrino beam starts from the top of the pictures and moves towards the bottom of the picture.

scintillator is polystyrene and dimethylacetamide with POPOP and para-terphenyl. The WLS fibers are 1 mm diameter Kuraray Y-11 fibers which have an absorption specturm centered at 430 nm and emission centered at 476 nm with little cross-over. The fibers in the PØD and FGD are mirrored at one end while the fibers in the ECal and SMRD have detectors on both ends.

Because many detectors are located inside a magnetic field with limited space, photo-multiplier tubes (PMTs) would not be useful. Instead, the detector design chosen would be a device with multiple avalanche photo-diodes on a single chip[72]. The specific detector chosen was the Hamamatsu Multi-Pixel Photon Counter (MPPC). Each detector has 667 pixels covering a total area of 1.3 by 1.3 mm^2 with each pixel having a size of 50 by 50 μm^2 as shown in Figure 3.3. The pixel is held at about 70 V, which is 0.8-1.5 V above the breakdown voltage. Given that the pixel capacitance is 90 fF, the gain is around 10^6. The photon detection efficiency at 525 nm is 26 to 30% for the detector with a dark rate at 25 °C of 1.35 MHz.

Each pixel operates in Geiger mode in which a single photo-electron produces a cascade,

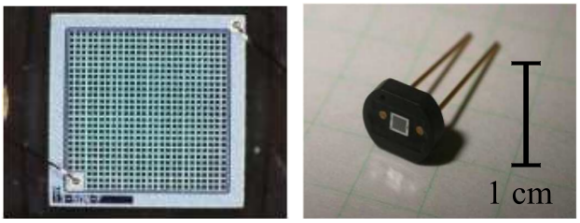

Figure 3.3: Photographs of the MPPC in which the left photograph is a zoom-in of the light-sensitive area. Image courtesy of the T2K collaboration.

which means that each pixel sends a binary signal corresponding to on or off. A fired pixel corresponds to one photo-electron (p.e). The total signal from the MPPC represents how many pixels on the MPPC are on, not the amount of light on a single pixel. However, the number of fired pixels can be correlated to the amount of light intensity. A pixel may cascade without light either through thermal excitation (dark noise), excitation from an adjacent pixel (crosstalk), or impurities in the silicon which cause a delayed secondary cascade after a proper cascade (afterpulsing). In order to prevent a cascade to be self-sustaining, a passive quenching resistive circuit is used. In this case, as the signal current increases, the voltage drop across a resistor in series with the bias voltage increases, causing the voltage across the photodiode to drop and stopping the cascade. The result is that a pixel has a recovery time constant of 19 ns, although afterpulsing has a recovery time constant of 85 ns[33]. A typical MPPC spectrum taken over time is shown in Figure 3.4 in which the MPPC is not exposed to light in order to find the dark noise.

3.2 Data Acquisition and Electronics

The overview of the entire data acquisition system and electronics is shown in Figure 3.5. The MPPCs on the PØD, ECal, SMRD, and INGRID use the same readout electronics. The MPPCS are connected via microcoax cables to a custom built Trip-T front-end board (TFB) which contains four Trip-T ASICs[61]. The MPPC signal is split to separate channels to represent a high and low-gain channel to increase the range of the electronics. In general, 10 ADC count on the high-gain channel corresponds to one p.e. (one fired pixel) while the

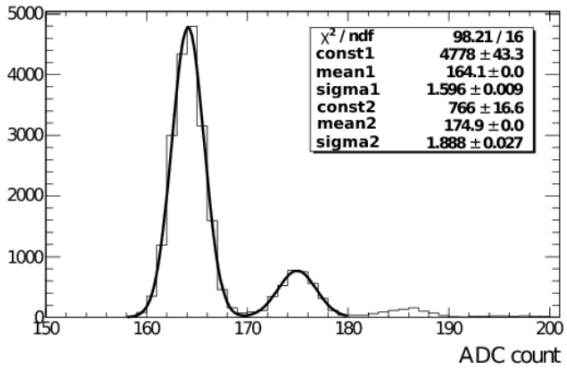

Figure 3.4: Dark Noise Output Spectrum of an MPPC. The first peak corresponds to the the output voltage with no pixels fired (called the pedestal). The next peak is one pixel firing (one p.e peak) and the next peak corresponds to two pixels firing. The distance between the peaks is corresponds to the gain in ADC counts. Image courtesy of the T2K collaboration.

low-gain channel has a maximum ADC at 500 p.e. The Trip-T chip integrates the total charge accumulated in a channel over a certain time window and can store 23 integration cycles. In addition, the high gain signals are sent to a discriminator, where the signals are time stamped with an accuracy of 2.5 ns and the signals are sent off to a Cosmic Trigger Module (CTM) to trigger the read out of the detector for various cosmic ray geometries. After the cycles are recorded, the data is digitized using two dual-channel 10 bit ADCs and sent off to back-end boards.

The back-end boards are a series of custom built Readout Merger Modules (RMMs) which act as data collectors and trigger boards. Each RMM can read up to 48 TFBs using Cat 5e cables and is connected by optical links via RocketIO to other RMM modules which act as triggers and clocks. One RMM acts as the Master Clock Module (MCM) which receives signals from the accelerator, GPS clock (used for time stamping), and the CTM in order to determine when to trigger the detector. The MCM is then connected to several Slave Clock Modules (SCMs) which effectively trigger each sub-detector as each sub-detector tends to have one SCM. The FGD and TPC have their own custom electronics

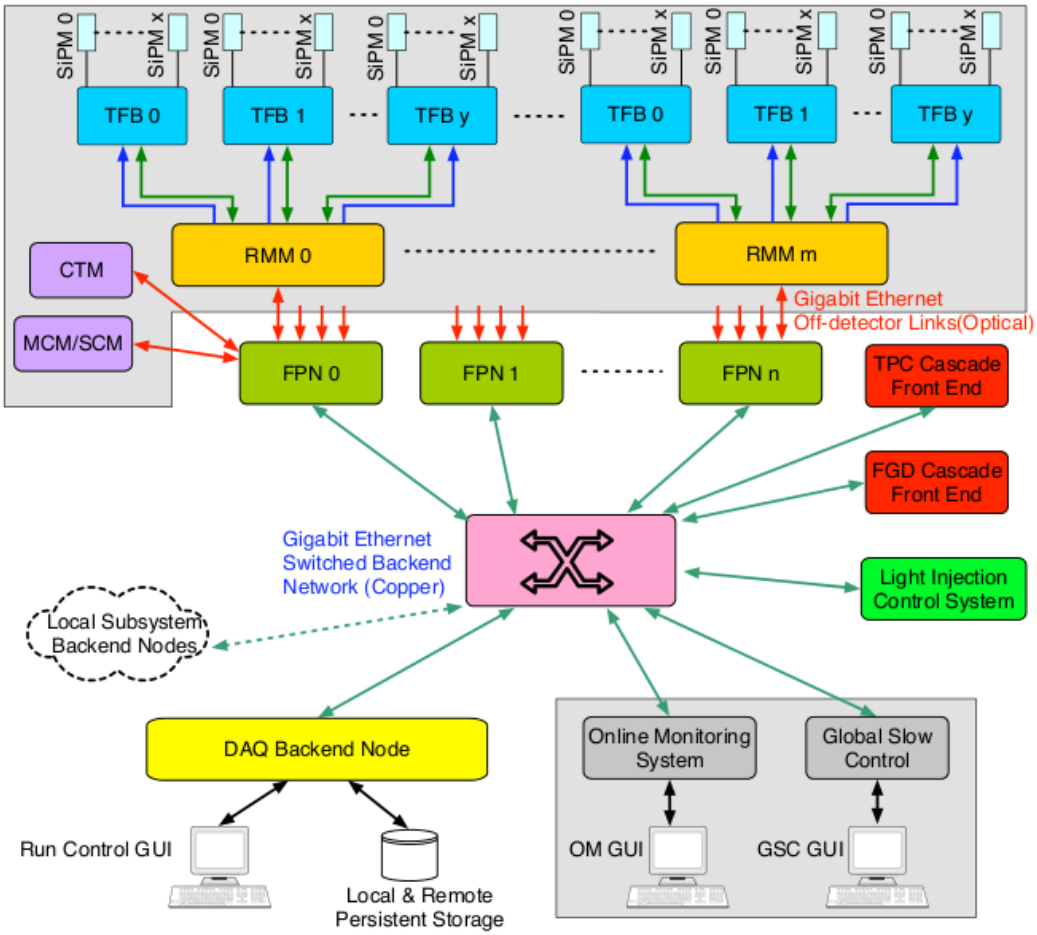

Figure 3.5: Schematic of the readout electronics and data acquisition system for the near detector complex. Image courtesy of the T2K collaboration.

which is based on the custom built "AFTER" ASIC. The data is digitized and stored as a waveform sampled at 50 MHz and stored in a capacitor array which is read out via optical fiber links to data collector cards (DCCs). The DCCs then communicate with a SCM which communicates with all SCMs, as well as the MCM and CTM.

The data acquisition system is split into two parts: the DAQ and the global slow control (GSC). The DAQ is responsible for recording the main detector data, storing the data, and supplying online information. The GSC is responsible for monitoring environmental and safety parameters. Both systems use the MIDAS framework[73] which allows a common C++ architecture as well as a built in web interface for control as well as display. The back-end systems communicate with the DAQ through the Front-end Processing Nodes (FPNs) which are PCs running Scientific Linux. The FPNs also interface with other PCs that run processes related to the GSC as well process operator displays and light injection systems used by the PØD and ECal for calibration and timing purposes. These systems also interact with the Online DataBase (ODB) which is a MySQL database containing parameters for running and storing GSC data. Finally, an event builder process combines information from the various FPNs and writes the data to a local buffer. The buffer is written to a local RAID before a custom achiever process sends the data to the KEK HPSS storage which in turn distributes to other sites in the world.

3.3 INGRID

INGRID (Interactive Neutrino GRID) is a detector consisting of several modules constructed into a cross centered on the neutrino beam with a few off-center modules as shown in Figure 3.6. The main purpose of INGRID is to monitor the neutrino beam direction as well as intensity in order to track the stability of the neutrino beam. There are 14 modules in the cross (7 horizontal and 7 vertical modules) and two off-center modules which are located diagonal to the center of the cross. A module is composed of 9 iron plates and 11 scintillator planes in which the iron and scintillator are interweaved except for the last 2 scintillator planes which have no iron plates due to weight limitations. The iron plates are 124.0 cm by 124.0 cm with a thickness of 6.5 cm. The scintillator planes are constructed from two sets of 24 scintillator bars in which one set is horizontal and the other set is vertical. The bars

are 5.0 cm wide, 1 cm thick, and 120.3 cm long. The exterior of the module has four veto planes (one on the top, one on the bottom, and one on each side) which are composed of 22 scintillator bars to veto out through going particles. A schematic of the modules is shown in Figure 3.7(a).

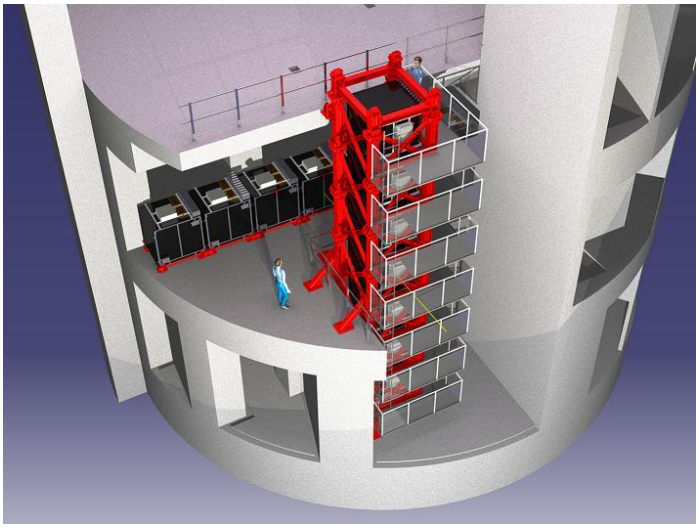

Figure 3.6: Schematic of INGRID. Image courtesy of the T2K collaboration.

In addition, an extra module, called the Proton Module, was added to detect neutrino interactions in which a muon and a proton are produced from a neutrino interaction. The purpose of this measurement is an independent confirmation of Monte Carlo as well as beam quality purposes. This module is similar to other modules, but lacks iron plates and has smaller scintillator bars for better tracking. The modules was placed at the beam center between the vertical and horizontal modules. An example neutrino event is shown in Figure 3.7(b).

3.4 Overview of the Pi-Zero Detector (PØD)

The PØD is the first sub-detector in the off-axis near detector (ND280-OA) that the neutrino beam will encounter. The main purpose of the PØD is to measure π^0 production from neutrino interactions with water in order to reduce background uncertainty at Super-

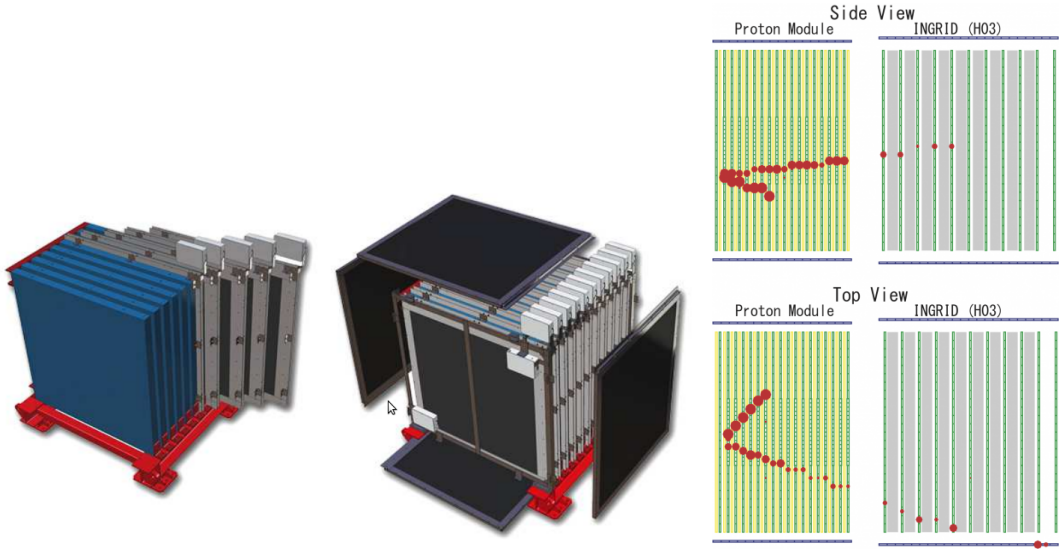

(a) Schematic of the INGRID Modules

(b) Event Display from INGRID Proton Module

Figure 3.7: INGRID Modules. Image courtesy of the T2K collaboration.

Kamiokande. However, other interactions on water can be studied for improved, or in some cases the first, cross section measurements. In addition, the large mass of the PØD makes it a target and as a time-zero calibration point for other detectors in ND280-OA (see Figure 3.8 for an example of events starting in the PØD and continuing to other parts of ND280-OA).

The structure of the PØD is a set of sandwiched scintillator planes interweved with either brass or lead or water. The PØD is divided into four subregions, called Super-PØDules: the Upstream ECal (USECAL), the Upstream Water Target (USWT), the Central Water Target (CWT), and the Central ECal (CECAL) as shown in Figures 3.9(a), 3.9(b), 3.10(a), 3.10(b). The USWT and CWT together represent the PØD Water Target (WT). Each Super-PØDule contains a set of scintillator layers (called PØDules) stacked together along the neutrino beam axis along with inert layers in between. In the ECals, the inert material is a lead sheet to help photon conversion, while in the WT the inert material is a brass sheet for photon conversion and then a water layer in order to produce neutrino interactions on water. Brass is used instead of lead in the WT in order to keep the inert mass of water and

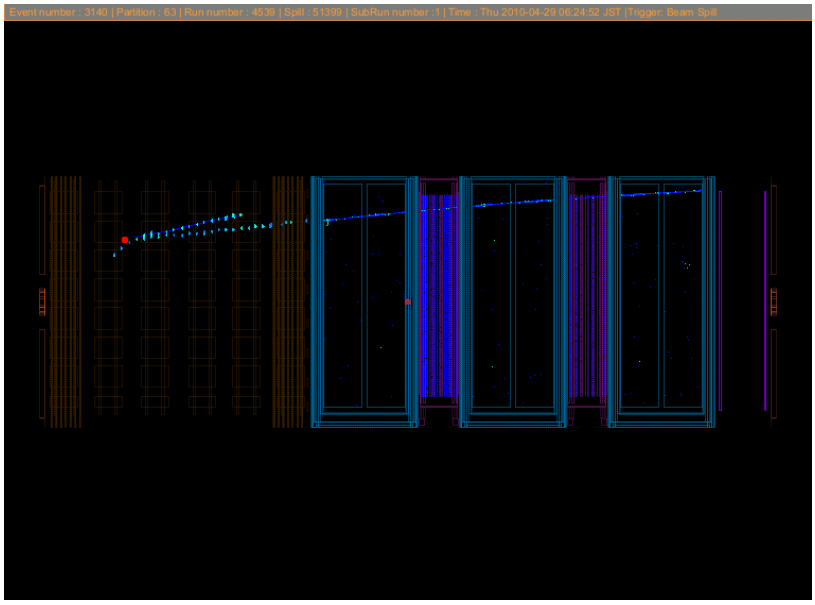

Figure 3.8: Example of a candidate neutrino interaction in the PØD with daughter particles traveling through the FGD and TPC. Image courtesy of the T2K collaboration.

brass similar to the inert mass of lead.

A PØDule is the base construction element of the PØD consisting of 2 layers of scintillator bars in which each layer is orthogonal to the other. There are 134 horizontal bars which are 2133 mm long and 126 vertical bars which are 2272 mm long in each PØDule. 40 PØDules make up the entire PØD resulting in about 10,400 total MPPCs. Unlike other sub-detectors, the bars in the PØD are triangular, not rectangular in shape. A bar has a height of 17 mm and a width of 33 mm. This shape allows bars to overlap, allowing some positioning information based on the amount of light (or charge) deposited in either bar as shown in Figure 3.11. Aside from the shape, the bars are similar to scintillator used in other parts of the detector as described in Section 3.1. There are seven PØDules in each of the two ECal Super-PØDules interweaved with stainless steel covered lead sheets that are 4.5 mm thick (0.7 radiation lengths for an electron with an energy of >10 MeV). The USWT has 13 PØDules interweaved with 13 brass sheets which are 1.28 mm thick (0.1 radiation lengths) and 13 water target layers. The CWT contains only 12 PØDules, 12 brass sheets,

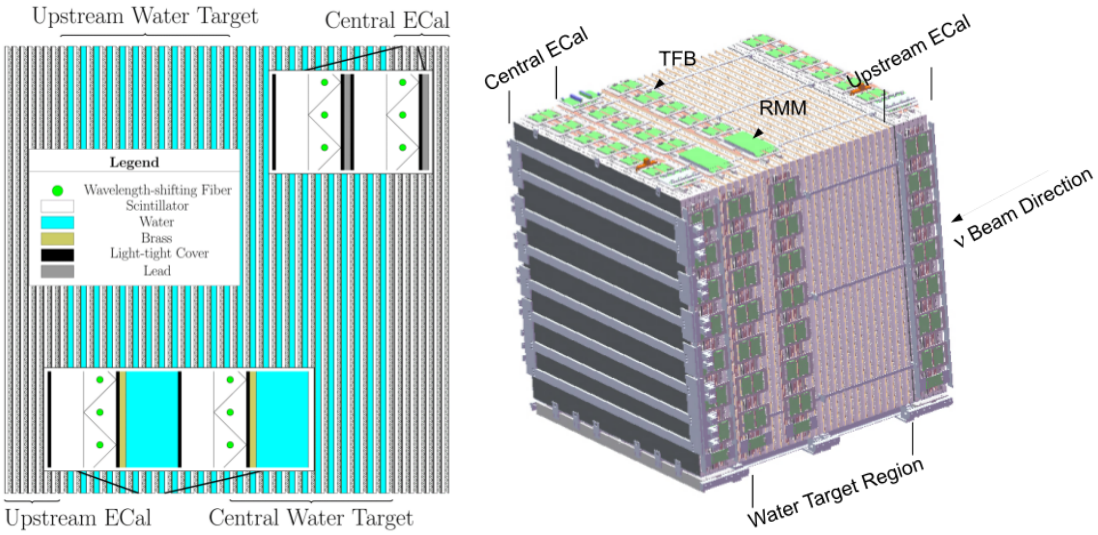

(a) Schematic of the PØD.

(b) Model of the PØD.

Figure 3.9: PØD Schematics. Image courtesy of the T2K collaboration.

(a) Photograph of the Upsteam ECal (USECAL) and Central ECal (CECAL) of the PØD before installation

(b) Photograph of the PØD installed in the basket.

Figure 3.10: PØD Photographs

and 12 water target layers. A water target layers is a High Density Polyethylene (HDPE) frame which supports two HDPE water bags that are nominally 28 mm thick when full. The water system for the PØD is fully described in Chapter 4. The size of the PØD active region is 2103 mm in width by 2239 mm in height by 2400 mm in length with an estimated mass of 15,800 kg with water and 12,900 kg with no water. The ECals are about 4.9 radiation lengths in depth, while the Water Targets are about 1.4(2.3) radiation lengths when empty(full).

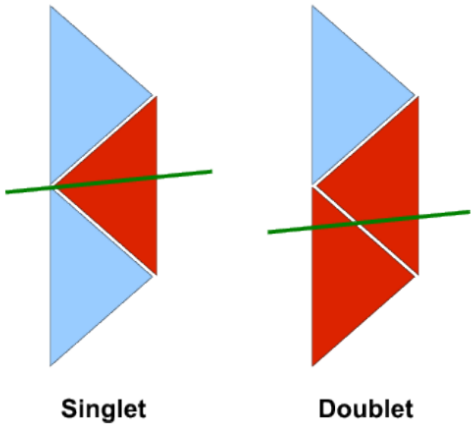

Figure 3.11: Example of a particle interacting with one scintillator bar (a singlet) and two bars (a doublet). Image courtesy of the T2K collaboration.

The electronics on the PØD consist of 174 TFBs and 6 RMMs. The TFBs are mounted on metal plates supported by "rails" located at the top and south side of the PØD. The rails on the top go horizontally while the rails on the side go vertically. The rails not only supply the four voltages needed for the electronics, but also support two aluminum extruded pipes which contain cooling water. Until the winter of 2011, the rails at the top of the PØD also supported the six RMMs which read out the TFBs. In the winter of 2011, the RMMs were moved off the PØD and installed underneath the basket along a supporting wall, called the curtain. The RMMs were moved to allow better access as well as better cooling. The ECal Super-PØDules have one pair of rails (top and bottom) while the WT Super-PØDules have two pairs of rails. The rails conduct electrical power through six bus bars. Four bus bars

at 5.5, 3.8, 3.1, and 1.7 V conduct power for the TFBs and RMMs while a fifth bar is at 70 V for the MPPCs and a sixth bar is set at ground. The current draw for the TFB bus bars are on the order of 4 to 40 A. In order to prevent humidity and circulate cooler air, the exterior of the PØD is covered with aluminum panels while dry air is injected inside the panels near the junction of the top and side rails. The air then travels along the rails before exiting the PØD.

Before installation, each PØDule was checked by use of an automated radiation source to scan along a PØDule looking for dead channels and confirming bar response. The bar response as a function of position was fit with using two exponential attention functions which represent a prompt response of the WLS fiber as well as a slower, secondary response. This function also included a reflection term as the WLS was read at only one end, with the other end mirrored.

In order to help with timing and calibration, the PØD has a Light Injection System (LI) designed to flash a known, but variable light source in order to examine MPPC performance in-situ. The LI uses 80 pairs of 400 nm UV LEDs as a light source with the ability to vary the LED intensity as well as the time the LED is active. The LI was used before on individual Super-PØDules in order to check that all channels were functional before installation. In addition, all Super-PØDules were individually run before installation using downward going cosmic rays to check channels and to find the overall resolution of the PØD. Both the LI and cosmic ray checks were performed when the Super-PØDules were finally installed in the near detector complex and these checks continue while the detector is taking data. In fact, the PØD can use thru-going Minimal Ionizing Particles (MIPs) as an energy calibration as the dE/dx is fairly constant over energy. This allows a measurement of the light yield per distance the particle traveled, which should be a constant over time and can be used to check detector response.

3.5 Overview of the TPC

Downstream of the PØD in ND280-OA is the Tracker section. The Tracker is composed of three Time Projection Chambers (TPCs) with two Fine Grain Detectors (FGDs) in between. The TPC allows for 3D measurement of a charged particles track which, using the magnetic

field, allows for charge identification as well as momentum measurement. In addition, by measuring charge deposition in the TPC as a particle travels, one can use the dE/dx and the known momentum for particle identification.

The TPCs, shown in Figure 3.12(a) and 3.12(b), are mostly constructed as an inner box filled with an Argon based gas (Ar:CF_4:iC_4H_{10} in a 95:3:2 mixture) inserted into an outer box filled with CO_2 for insulation. The center of the inner box has a cathode plane which produces a uniform electric field parallel to the magnetic field.

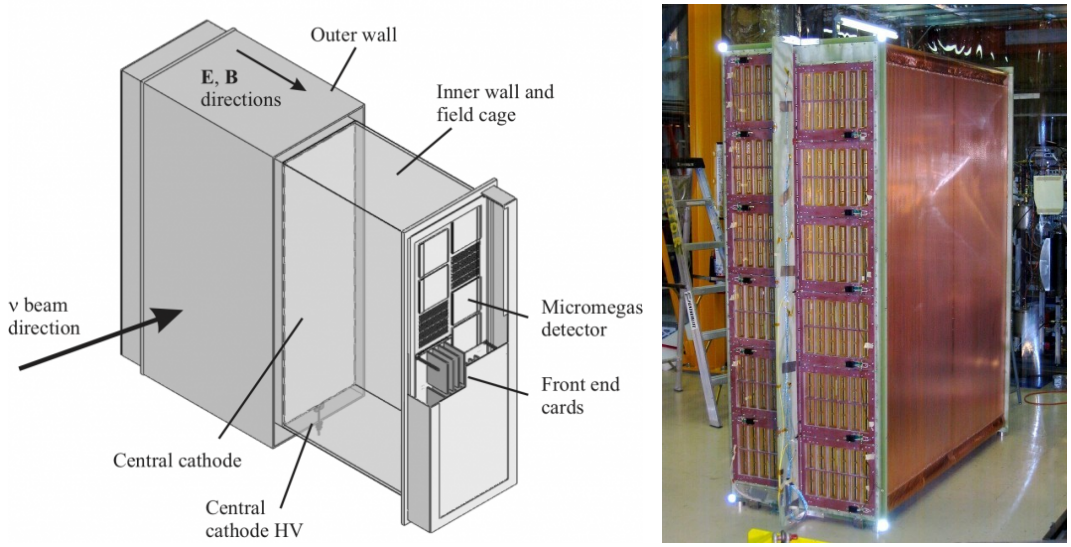

(a) Schematic of a TPC.

(b) Photograph of the inner box of a TPC.

Figure 3.12: TPC Schematic and Photograph. Image courtesy of the T2K collaboration.

As a charged particle passes through the TPC gas, the particle ionized the gas producing electrons which drift along the electric field away from the center cathode to the edge of the TPC. At the edge are a series of micromegas detectors[49] which multiply and sample the drifting electrons. A micromegas detector uses a metal mesh suspended over an anode pad using insulated posts in order to create an electron cascade between the mesh and the pad to multiply the signal, but not distort the electric field in the bulk. The anode pads in the TPCs are 7.0 mm in the vertical and 9.8 mm in the horizontal. There are 12 micromegas

modules which are 342 mm in the vertical and 359 mm in the horizontal covering each readout plane of a TPC resulting a total of 72 modules over all three TPCs. The pattern of active anode pads provides 2-D information while the timing of pad activation provides the full 3-D information. However, in order to determine the initial start of a charged track, timing information from other detectors such as the PØD or FGD is needed. The data is then sent to the DAQ as described in Section 3.2. In general, the TPC has spatial resolution around 0.8 mm and a momentum resolution of 10.0% of the momentum perpendicular to the magnetic field.

3.6 Overview of the FGD

There are two fine grained detectors (FGDs) located between two TPCs. The purpose of the FGDs are to act as target material for the Tracker as well as to track particles coming from the interaction vertex, such as protons. In order to do so, the FGD is composed of scintillator bars which are 9.61 mm in the horizontal, 9.61 mm in the vertical, and 1864.3 mm long. These bars are smaller than in other sub-detectors, allowing for better tracking of short particle tracks. The bars are arranged in layers which are perpendicular to the previous layer. The first FGD has 5,760 bars arranged in 30 layers while the second FGD has only 2,688 bars in 14 layers.

The second FGD has less bars because there are six 25 mm thick water layers in the second FGD. The water layers are made from 25 mm thick sheets of hollow corrugated polycarbonate in which water is circulated at sub-atmospheric pressure to prevent leaks. By performing measurements on both FGDs, it is possible to do a subtraction measurement in order to measure cross sections on water. The FGD uses similar MPPCs as other scintillator detectors in the near detector pit, but instead sends the signal to the "AFTER" ASIC and DCCs in a similar method as the TPC.

3.7 Overview of the ECal

The Electromagnetic Calorimeter (ECal) surrounds the PØD, TPCs, and FGDs in order to detect particles leaving the inner detectors and help with energy reconstruction. The ECal is divided into 13 separate modules which are all composed of scintillator bars. There are

six modules which surround the PØD along the four horizontal and vertical sides known as the PØD-ECal modules, six modules which surround the TPCs and FGDs along the four horizontal and vertical sides known as the Barrel-ECal modules, and a module which covers the downstream end of the last TPC known as the Downstream-ECal (DS-ECal). The bars used in the ECals have a rectangular cross section of 40 mm by 10 mm.

The DS-ECal has 34 layers of 50 scintillators bars 2040 mm in length in which each layer is orthogonal to the other. Each layer has a 1.75 mm sheet of lead after it. The Barrel-ECal has only 31 layers due to limited space but has similar bars and lead sheets. However, the bars which run along the beam direction are 3840 mm long while bars in the top and bottom modules which run perpendicular to the beam direction are 1520 mm long. The bars in the side modules which are perpendicular to the beam direction are 2360 mm long. The PØD-ECal has a very limited space available and is designed more to detect if photons or charged particles have left the PØD. Therefore, the bars in the PØD-ECal all run along the beam direction and are 2340 mm long. There are six scintillator layers separated by a 4 mm thick lead sheet for photon conversion.

3.8 Overview of the SMRD

The Side Muon Range Detector (SMRD) is a set of scintillator planes located in the UA1 magnet yoke designed to measure escaping muons from the inner detectors, act as a trigger for cosmic ray muons and look for neutrino interactions in the magnet and surrounding wall. The SMRD is composed of 440 scintillator modules inserted into air gaps which are 17 mm thick between the 48 mm thick steel plates in the yoke. The horizontal modules are composed of four scintillator planks with length of 875 mm, width of 167 mm, and height of 7 mm. The vertical modules have five scintillator planks with length of 875 mm, width of 167 mm, and height of 7 mm. Instead of using bars, the scintillators are produced as a plank with an S-shaped grove in the middle into which the wavelength shifting fiber is inserted. The grove has a bending radius of 29 mm and is 25 mm deep. This shape allows for more collection of light from the plank. There are a total of 4,016 MPPCs which are connected to the data acquisition system.

Chapter 4

PØD TARGET WATER SYSTEM

4.1 Introduction

This chapter presents an overview of the PØD water target system and water target mass calculations. This chapter is divided into two main sections. The first part covers the design and operation of the water target system while the second part covers the calculations needed in order to determine the mass of water in the PØD. In addition, we will include historical data representing the overall performance of the system over a period of three data taking periods in which the PØD was filled with water.

In general, the water system was originally installed with a set of custom Pressure Sensors (used during the Run 1 period of data taking). The system was upgraded with improved Depth Sensors during the Run 2 period of data taking and was upgraded with improved leak detection systems during the Run 4 period of data taking. These improvements are described in the upcoming sections.

4.2 Overall Water System

The water system was designed to supply water for the Water Target Super-PØDules, monitor the water level, drain the Water Target Super-PØDules, and measure the amount of water inserted and removed. The PØD has 25 water layers with 2 bags per layer as described in Section 3.4. Water is initially stored in a 3400 liter Main Tank and then pumped out using 50 pumps arranged in a pump rack into each bag. The water is removed using the same pumps.

The water monitoring was performed using two configurations. Initially, the water level was measured using Binary Wet-Dry Level Sensors along with a Pressure Sensor Combination. This configuration was upgraded after the first 6 months of running to a more sensitive and robust system that used Binary Wet-Dry Level Sensors and commercial Depth Sensors.

The entire system operates on an independent DAQ system.

Initially, metered pumps were going to be used to determine the amount of water inserted into the PØD, but instead the volume was found by determining the amount of water removed from the main tank as well as water height calculations. The details of these calculations are given in Section 4.5.

The next sections will go into the individual elements of the system in more detail.

4.2.1 Water Target Design

The PØD Water Target Super-PØDules were designed with interleaving layers of scintillator bars, brass, and water. Each layer was designed to have a water region that is approximately 30 mm thick along the beam direction and is 2 meters long in the transverse direction. To keep the water container mass low, high-density polyethylene (HDPE) bags were used. These bags contain the water, but structural support is supplied by the adjacent scintillator bars. The entire PØD is supported on the front end by the detector basket while the rear portion of the PØD is supported by cross beams clamped to the basket support beams. As the rear cross beams are not welded to the basket, it is expected that the PØD will lengthen by about 5 to 10 mm when the PØD is full of water.

Because the bags are not rigid, if a bag is empty while others are full, the scintillator layers would bulge due to unbalanced water pressure. Finite element analysis predicted that the PØD would be structurally sound in such an event, but would impact event reconstruction. In addition, requiring two bags per layer (each bag being about 2 meters in the vertical direction, 1 meter in the horizontal, and 30 mm in the beam direction) would help reduce any structural effects in case of an empty bag. With two bags, a central strut of HDPE was added to limit horizontal deflections in case of a water level mismatch between adjacent bags.

The bags were sealed into two HDPE pieces at the top and bottom of the bag, refereed to as the header and footer pieces respectively. The header had ports for fill, drain, and sensor tubes. The entire PØDule frame were edged with silicone sponge gasket material (Stockwell Elastomerics R-10470), so that each bladder was effectively encased within a waterproof seal

when compressed between adjacent PØDules. The footer was equipped with drain ports to direct any water captured within the gaskets to two drip pans mounted below the PØD and basket, one on either side of the basket centerline. The headers, footers, and frames were produced at the University of Washington Instrument Shop, shipped to Colorado State University for bladder insertion and heat-welding, then returned to University of Washington for testing and leak-checking. Each target layer was filled with water and left overnight before acceptance and shipment to Stony Brook University for integration with scintillator layers and assembly into Super-PØDules. The upstream water target Super-PØDule had 13 water layers (26 bags) and the central water target Super-PØDule had 12 layers (24 bags), for a total of 25 water target layers and 50 bags. After Super-PØDule assembly, the Super-PØDule was filled and drained at Stony Brook University and repeated when the Super-PØDule arrived at J-PARC before insertion into the detector basket.

4.2.2 Fabrication of Water Targets

The water target bags were made from a 1 meter wide continuous roll of seamless polyethylene plastic tubing. The plastic sheet was 0.15 mm thick, so the combined thickness of the water bag was 0.3 mm thick. The tubing was cut to the length of the PØDule height and the bottom was heat welded to the footer in order seal the bag and attach the bag to the lower frame. The header was attached but the top of the bag was not sealed. When inserted into the PØDule, the header was held in position by resting on the edges of the HDPE PØDule frame while the footer was held in place by screws which went through the bottom frame of the PØDule. This allowed the screws to hold the bag taunt, but allowed the screws to be loosened to allow the bag to be removed from the top once the Super-PØDule was completed without needing to disassemble the Super-PØDule.

After the PØD was inserted into the detector basket at J-PARC, it was discovered that a set of threaded rods were mistakenly left in the header that prevented bag removal from the top. These rods were inserted during transport to keep the Super-PØDules together, but were not needed once the Super-PØDules were inserted into the detector basket. In case of a bag replacement, a procedure was created in which the header of the leaky bag is

cut to allow access to the threaded rods, which are cut, and then unscrewed until the entire rod is removed one piece at a time. This procedure was used in the summer of 2012 when Bag 28 was replaced.

4.2.3 Water Target Plumbing

A water pump and monitoring system was designed to allow individual bladders to be filled, drained, and also provide water depth data. An overview is shown in figure 4.1. A pump rack with 50 self-priming bellows pumps (Gorman-Rupp Industries (GRI) 16001-005 F-009 T-007), one for each bladder, was designed with valves arranged to allow each pump to be used to either to fill or drain a single bladder. Photos of the pump rack are shown in figure 4.2. The pump rack was located outside the magnet on the B1 level of the Neutrino Monitoring building. The pumps were connected to fill and drain tubes on the bladders using Polyflo 66P 3/8 inch outer diameter polyethylene tubing. This tubing runs from the top of the pump rack to a connection manifold on the north side of the PØD which allowed the PØD to be transported with fill and drain tubes in place during construction.

The main target water storage tank for the PØD was a 900 US gallon (3400 liter) high density polyethylene tank, Ace Rotomold model VT0900-46, with an outside diameter of 1.18 meters and a height of 3.07 meters. On the top of the tank, a 410 mm diameter opening was used for insertion of four PVC pipes used to connect the bottom of the tank to four 20 liter buffer tanks on the P0D pump rack. The opening was loosely covered with polyethylene sheets to prevent dirt and dust from getting into the water.

The tank was filled with local tap water, filtered through a commercial pool filter to remove particulate matter. We added 0.875 liters of household bleach (6% solution of sodium hypochlorite) per tankful (3400 liters), as a biocide. The chlorine concentration was based on nominal values recommended for long-term storage of drinking water. This level of chlorination has no effect on the physics analyses. The tank was drained, refilled, and re-chlorinated every time a complete fill/drain cycle of the PØD was performed.

A valve was installed near the bottom of the main tank for drainage into a buffer/splash tub, which was connected by large-diameter tubing to the sump channel on the basement

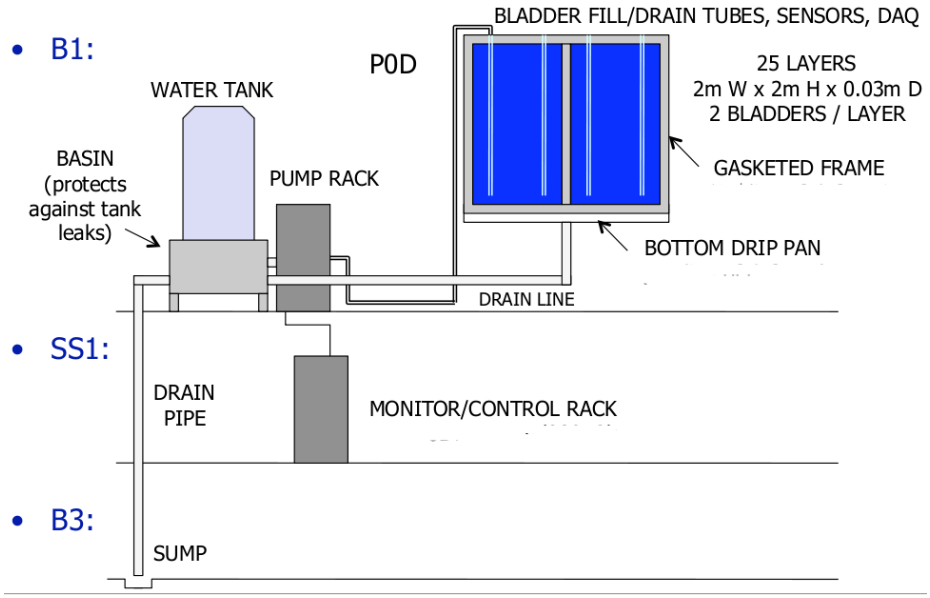

Figure 4.1: Diagram of the Water/Electronic Connections for the PØD (image courtesy of Jeff Wilkes

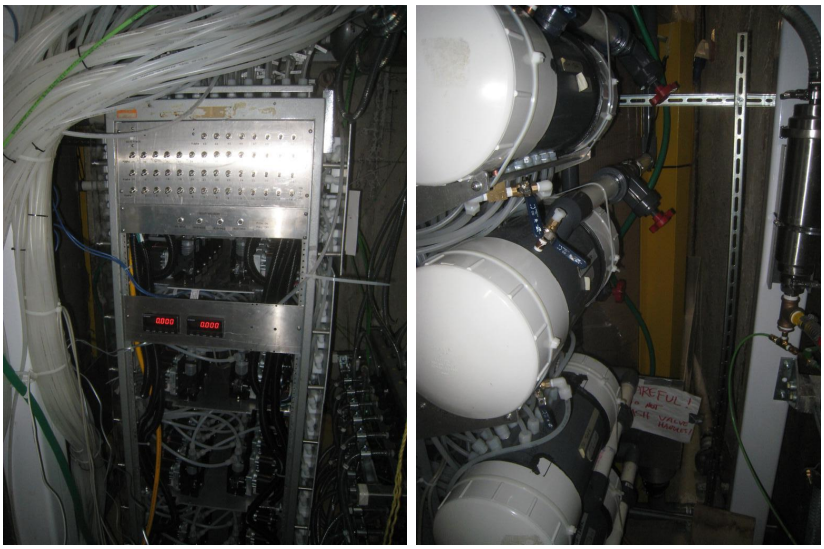

(a) Front (b) Back

Figure 4.2: Pump Rack

level. For volume calibration measurements, the drain valve output was diverted into measuring tubs using plastic hoses.

Each bladder was equipped with separate drain and fill tubes made of 3/8 inch schedule 40 PVC pipe. Each bladder had two additional PVC pipes containing water monitor sensors as described in Section 4.2.4.

Finally, to protect against a leak in a water bag, the underside of the PØD is covered with a Drip Pan. The Drip Pan was constructed from aluminum in two sections which cover the north or south half of the PØD. Each Drip Pan half contained a drain which is connected to a drain system that connects with the large-diameter tubing going to the basement sump channel. In the summer of 2012, this Drip Pan was replaced with an improved version which was divided into four pieces with a better drain system and built-in leak detectors which will be described in Section 4.2.6.

4.2.4 Water Sensors

In order to properly monitor the water level in each water target layer, sensors were inserted into each water target bladder. Accurate water level readings are needed not only for safety and engineering concerns, but needed to determine the water mass inside the fiducial volume of the PØD.

Two configurations of sensors were used to measure the water level in a water target bladder. The sensors initially installed had a significant failure rate, and also showed larger systematic uncertainties than acceptable, so a complete new set of sensors was installed after the first 6 months of running, during the summer accelerator downtime. Drawings of the two configurations and overall dimensions are shown in figures 4.3 and 4.4.

Original Configuration

In the original configuration, each water target bladder had two 2060 mm long, 20.4 mm wide PVC sensor pipes. The primary sensor pipe had a SSI Technology MediaSensor Pressure Transducer at the end, four Honeywell LLE Series Liquid Level Sensors spaced along the pipe, and two General Electric MA100 NTC Thermistors for temperature measurements.

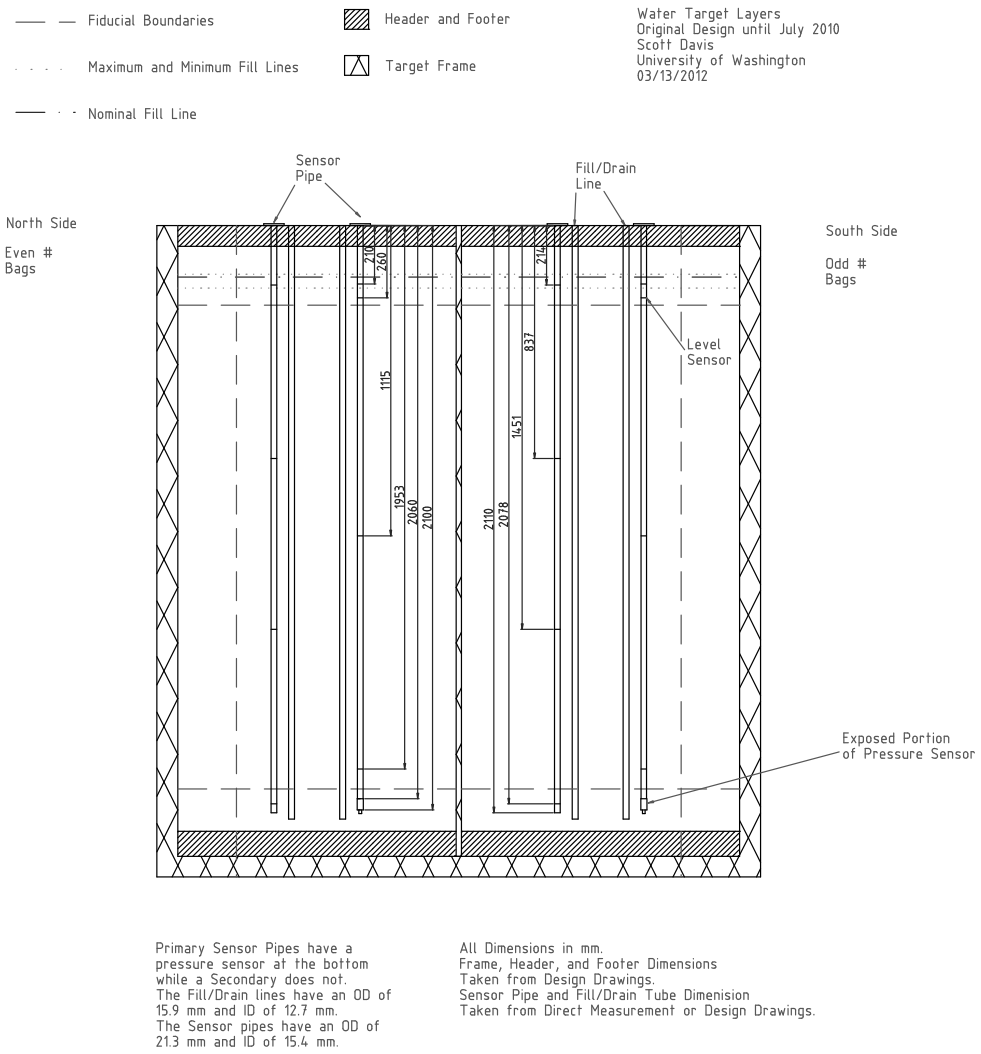

Figure 4.3: Original Configuration of PØD

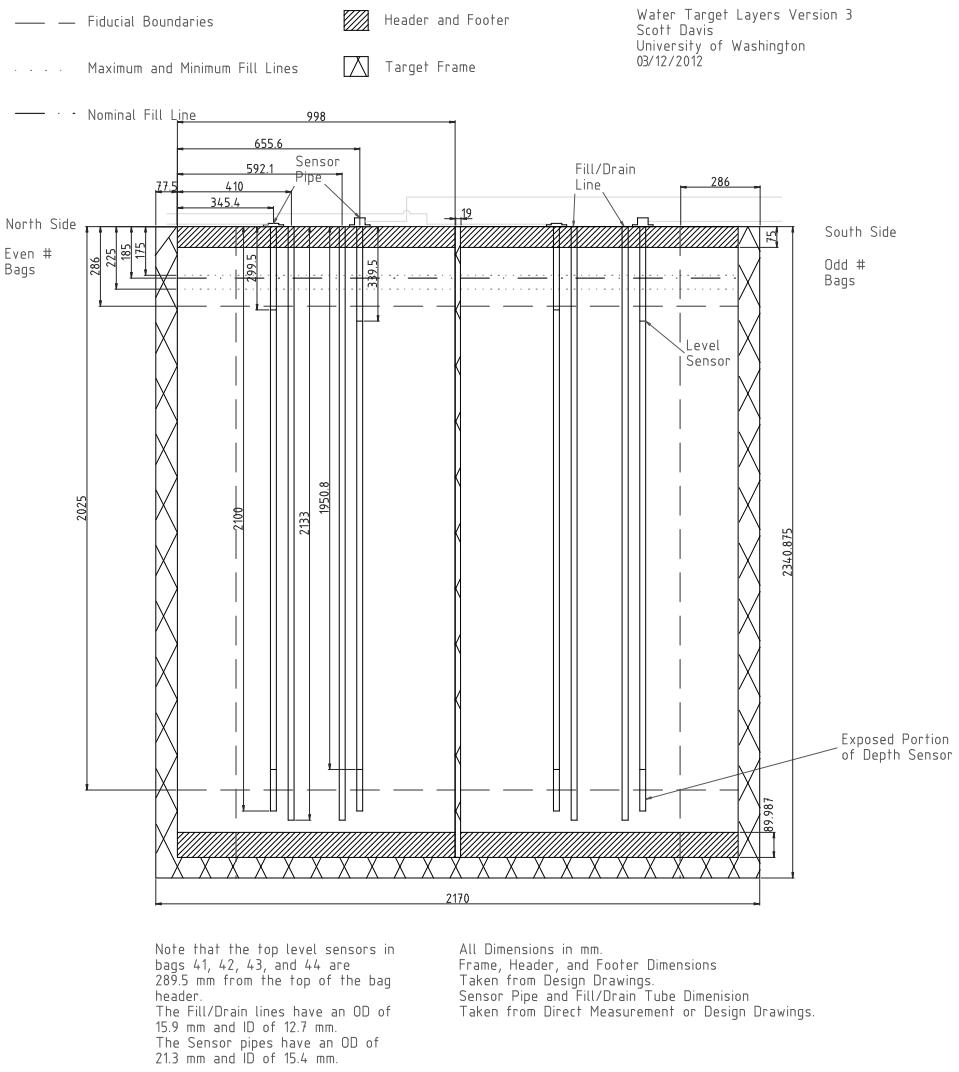

Figure 4.4: Updated Configuration of PØD

The secondary sensor pipe was similar to the primary except that it had no Pressure Transducer and the Binary Wet-Dry Level Sensors were at different depth levels (see Table 4.1).

Primary Sensor Pipe	Secondary Sensor Pipe
14.4 cm	0.47 cm
98.33 cm	63.23 cm
183.87 cm	126.1 cm
188.77 cm	188.77 cm

Table 4.1: Location of Binary Wet-Dry Level Sensors on sensors pipes in the original configuration. Location is based on the vertical distance from the bottom of the pressure sensor but just above the threaded extension

Water Depth was determined by determining the pressure difference between the Pressure Transducer in the water target bladder and a a SenSym ICT series ASDX Pressure Transducer located on the top of the Water Target Frame. The Binary Wet-Dry Level Sensors were used as a back-up level system as well as points to calibrate the difference between the Pressure Transducers.

Upgraded Configuration

After the first 6 months of running, it was clear that the initial configuration of sensors was not adequate to our needs. We discovered that the uncertainty in the pressure sensors caused the recorded depth to have noise on the order of 10 mm, even using ADC averaging. In addition, the pressure transducers inside the water target did not show long term survivability as only 37 of the original 50 sensors were operational after 6 months. Further details are in Section 4.3.

An entirely new set of sensors was installed over the summer 2010 beam-off break. New sensor pipes were installed in all bladders. In each bladder, both pipes had a GlobalWater WL400 Water Depth Sensor at the bottom end of the pipes. Each pipe also had one Honeywell Binary Wet-Dry Level Sensor, with improved waterproofing, placed near the

top of the sensor pipe for calibration and back-up purposes. The Global Water WL400 is warranted to have a 0.2% full scale accuracy between 1 C and 21 C. The linearity is 0.1% [50]. The liquid level sensors have a 3.5 mm radius front surface, and provide a 1 mm repeatability on fill or empty. There is a 2 mm hysteresis between fill and drain cycles.

One sensor pipe had the Binary Wet-Dry Level Sensor located 299.5 mm from the top of the water target bag header (labeled as the "High" sensor pipe), while the other sensor pipe in the bag has the Binary Wet-Dry Level Sensor located at 339.5 mm from the header (labeled as the "Low" sensor pipe). There is an exception for bags 41, 42, 43, and 44 in which the High Binary Wet-Dry Level Sensor is 289.5 mm from the header.

All new sensor pipes were water tested overnight or longer at University of Washington or University of Colorado at Boulder. In addition, the depth sensors were recalibrated by filling test pipes to a series of measured heights, and logging repeated depth readings. These data were then used to fit calibration curves relating depth to current-loop mA. Results were consistent with factory calibration data. The calibration process was checked with a 1-point measurement using an identical test stand after shipment to J-PARC. All the new sensor pipes were installed by mid-September, 2010.

4.2.5 Water System DAQ

The monitoring system consists of sensors which were inserted into the bladder and operated in the water itself, external monitoring sensor for the environment, and a DAQ system to collect the data and supply power. The entire system was designed to be independent of the ND280 Global Slow Control in order to be independent of shutdowns and to provide additional flexibility needed during PØD fill or drain operations. An outline of the two configurations we used is shown in Figure 4.5.

Original Configuration

The sensors were connected to a Sensor Board, a custom DAQ card built at the University of Washington, mounted on the top of the PØD, above the water target bladders. This board contained a SenSym ICT series ASDX Pressure Transducer for atmospheric pressure,

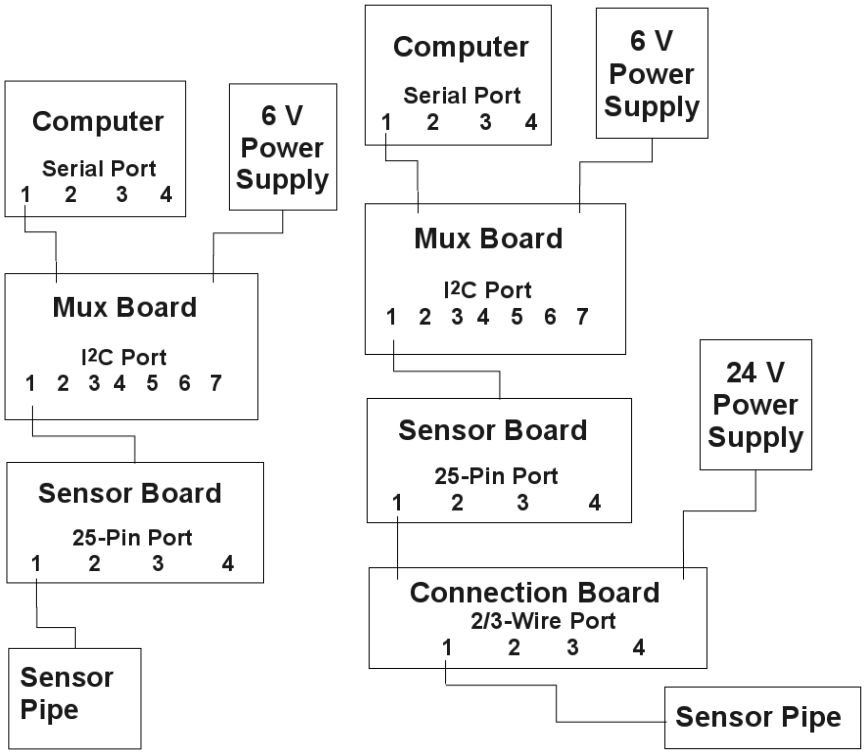

(a) Original Configuration (b) Upgraded Configuration

Figure 4.5: DAQ Connections

a Texas Instruments TMP275 Digital Temperature Sensor, two AD7998 8-channel, 12-bit ADCs to read the sensor outputs, and digital logic to communicate with the rest of the DAQ. The ADC has a full scale range of 0.0 V to 2.5 V. This leads to a resolution of 0.6 mV per bit. The ADC has an integral nonlinearity, defined as the maximum deviation from a straight line passing through the endpoints of the ADC transfer function, of ±1 least significant bit maximum but typically at ±0.2 least significant bits. The ADC has a differential nonlinearlity, defined as the difference between the measured and ideal, of +1/-0.9 least significant bit maximum but typically ±0.2 least significant bit. In addition, the ADC is rated to have a 2 μs conversion time and is rated for temperatures from −40 to 85 °C [24]. We noticed in situ as well as in a test stand, that changing the ambient temperature around the ADC by 10 °C has no change in recorded water depth.

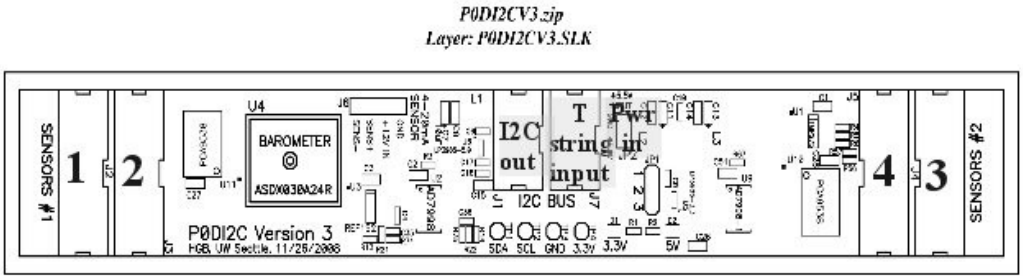

(a) Sensor Board Schematic

(b) Sensor Board Photo

Figure 4.6: Sensor Board

The DAQ communicates using I^2C data communication between local hardware compo-

nents and is converted to RS-232 serial data due to the distance required between the PØD and the available computer location. Sensor signals were digitized on the Sensor Boards, which were in turn connected to a custom built, 8 port Multiplexer (Mux) Board using the I^2C bus. A total of seven Mux boards were required. The Mux Board converted the I^2C signal to RS232 and also supplied power to the sensors and electronics. Photographs of the Mux Boards are shown in Figure 4.7.

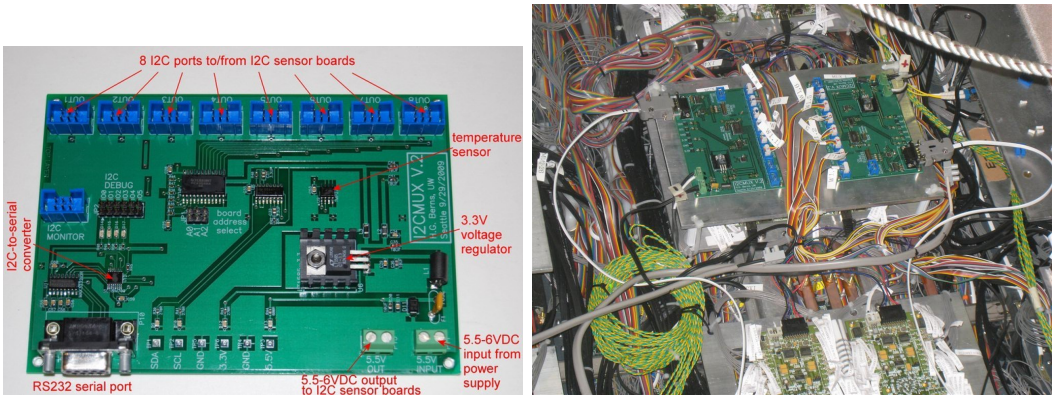

(a) Photograph (b) Mounted on PØD

Figure 4.7: Mux Board

The mapping system identified each sensor pipe with a port on the Sensor Board. Then each Sensor Board was identified by a port on a given Mux Board, which were connected to specific COM ports on a PC located on the SS Level. The mapping scheme is shown in Figure 4.8. In general, each Sensor Board monitored a single layer in the PØD and each Mux Board monitored half of a Super-PØDule. The Primary sensor pipes (which have the pressure transducer at the end) is located in the South position of each bag, while the Secondary sensor pipe is located in the North position of each bag.

The sensors are controlled and monitored by a graphical interface written in C++ by S. Davis. The monitoring program controls when the sensors are read, interprets the data, and then stores the data locally as well as with the Global Slow Control. When the program queries the DAQ, each Mux Board will query a Sensor Board to report the output of each digital chip or ADC chip. In order to suppress noise, by default the ADC chip is read 20

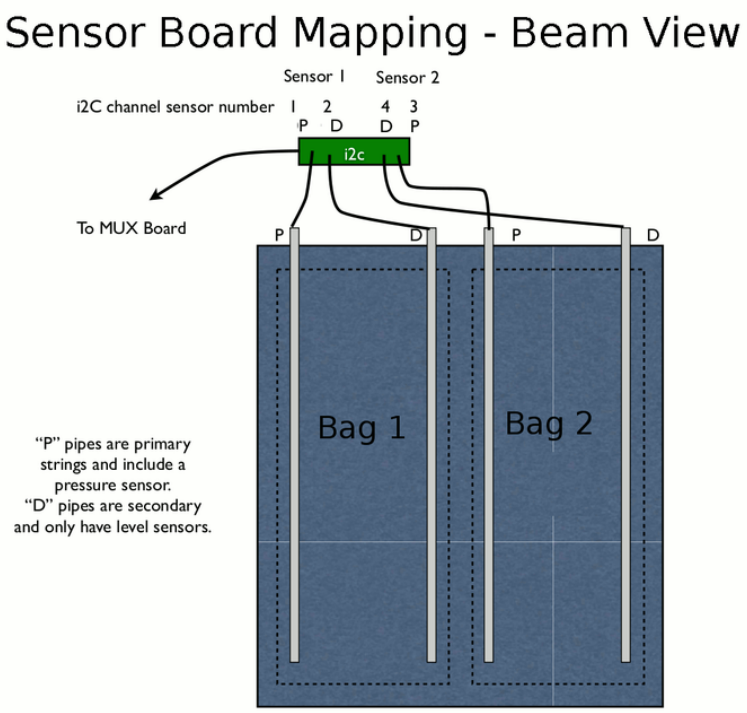

(a) Sensor board mapping.

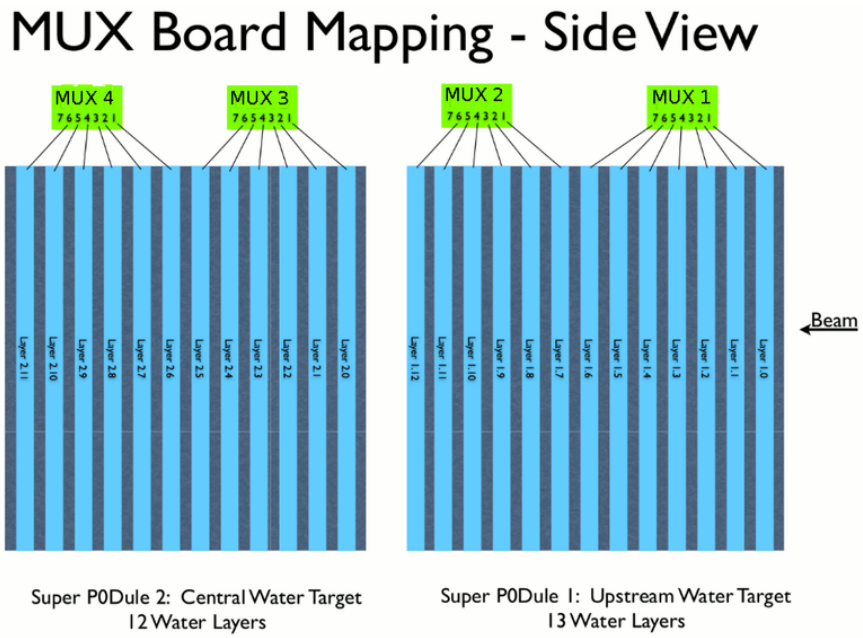

(b) Mux board mapping.

Figure 4.8: Sensor mapping scheme for the original configuration (image courtesy of Alysia Marino).

times and the average ADC value for each channel is recorded as well as the maximum and minimum ADC value for each channel. Because each Mux Board is connected to a separate COM port, each Mux Board is read simultaneously allowing the entire PØD to be read in 10 seconds. However, if the ADC averaging is removed, the time it takes to query the entire PØD drops to 5 seconds. The water monitoring program (i2cwaterdisp) is based on qt 4.5.1[78] and qwt 5.2.0[80]. The GUI windows were created using QDevelop[59] and QTDesigner 4.7[77]. Description of the monitoring software is located on the water expert page located on `http://www.t2k.org` and an example is shown in Figure 4.9.

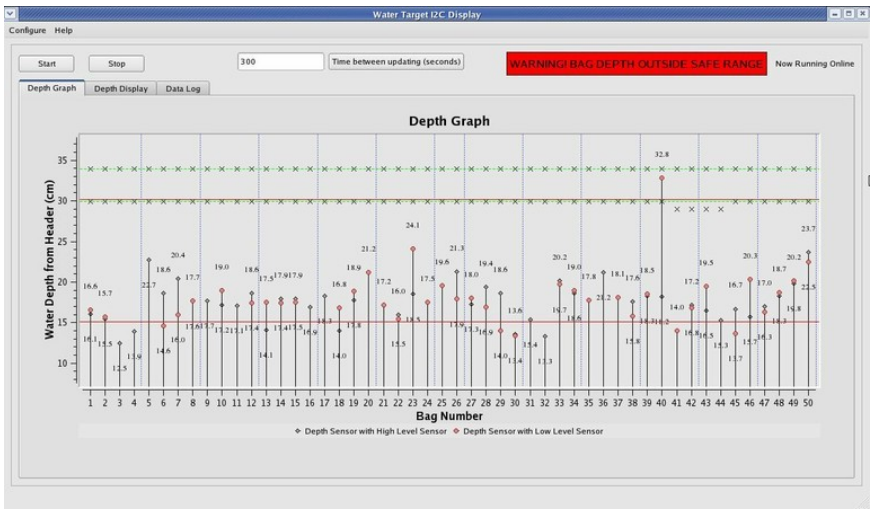

Figure 4.9: Monitoring software showing a few uncalibrated depth sensors.

Water DAQ Upgraded Configuration

The sensors were read out via the existing Sensor Boards and Mux Boards. However, the new depth sensors required an auxiliary custom built Connection Board to distribute DC power and convert current-loop signals to voltage signals for the Sensor Boards.

The Connector Board, shown if Figure 4.10, allows a two-wire connection to a 24V supply as well as a two-wire output connection to the GlobalWater WL400 Water Depth Sensor and a three-wire connection to the Binary Wet-Dry Level Sensors. The Connector

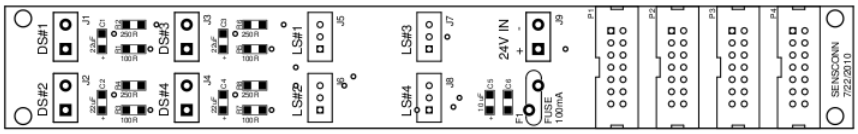

Figure 4.10: Schematic for the connector board.

Board has a 249.5 ohm resistor for each Depth Sensors in order to convert the current signal from the Depth Sensor into a voltage signal which is transferred to the Sensor Board.

In the original configuration, the Sensor Boards were directly attached to the water target headers underneath all the MPPC readout electronics (TFBs, RMMs, and the power/cooling ladders). However, it was discovered at the end of Run 1 that condensation on the cooling ladders when the electronics were not operational could fall onto the Sensor Boards and create a short. It was decided that we would have two Depth Sensors per bag, and the sensors should be connected in such a way that if one sensor board is not functioning, there would still be a way to read a Depth Sensor in every bag.

The mapping scheme is shown in Figure 4.11. In general, there are two Sensor Board/Connector Board pairs for every two layers (four bags). A Sensor Board/Connector Board pair is mounted on the North side of the PØD and on the South side of the PØD. The Depth Sensors on the North side of each bag are connected to the Sensor Board/Connector Board pair on the North side of the PØD, while the Depth Sensors on the South side of each bag are connected to the pair on the South side of the PØD. Using this scheme, each bag is read out by two different Sensor Boards. Each set of 6 layers (6 Sensor Board/Connector Board pairs) is read out by a Mux Board, except for the last Mux Board which must read out 7 layers and has a slightly different pattern. It should be noted at all High sensor pipes are the sensor pipes in the North position in the bags, while the Low sensor pipes are the pipes in the South position in the bags.

An extra Global Water Depth Sensor (serial# 1023103141) was mounted in the Main Tank in order to determine the depth of water in the Main Tank. This sensor was attached to a wood block mounted on top of the Main Tank as shown in Figure 4.12. This sensor

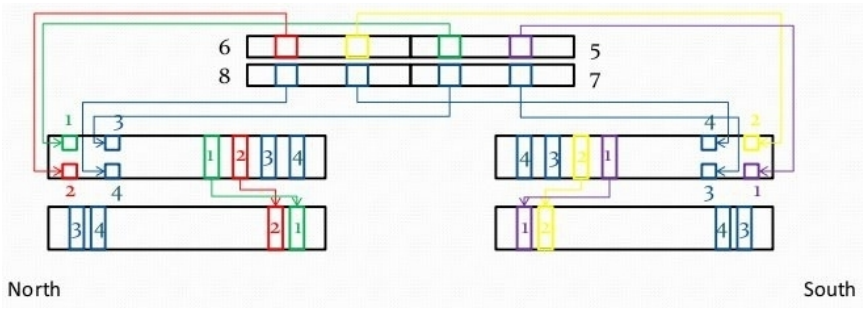

(a) Connector and sensor board mapping showing the connections between the sensors in water bags on the PØD labeled bags 5,6,7, and 8 and the conntections on the connector boards and sensors boards (image courtesy of James Imber).

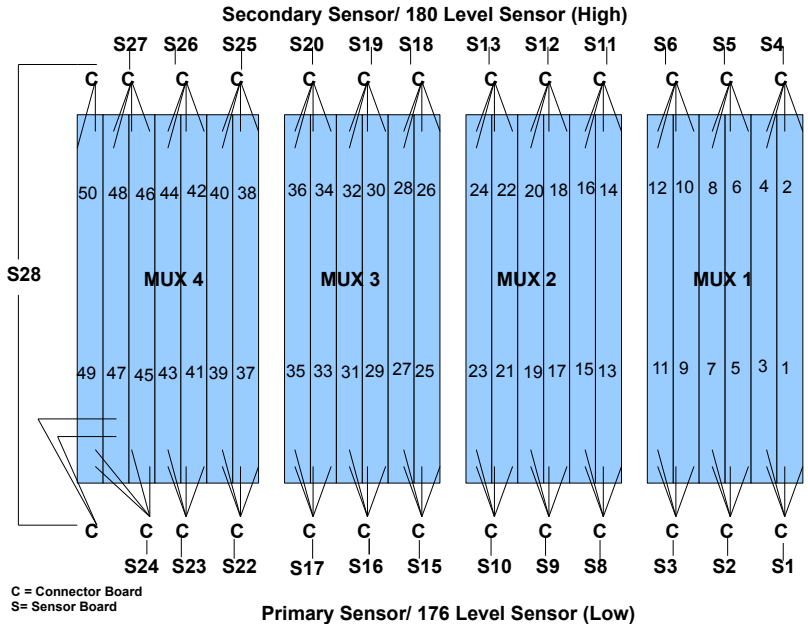

(b) Sensor board numbering and mapping showing which sensor board is connector to which bags. All sensors on a sensor pipe with a low sensor are connected to the bottow row of sensor boards while all sensors on a sensor pipe with high sensors are connected to the tow row of sensor boards.

Figure 4.11: Sensor mapping scheme for the upgraded configuration.

is not read out through the normal Water DAQ system, as the Main Tank is located away from the PØD outside the magnet. Instead a similar, smaller version of the Water DAQ was installed in which there is a single Mux Board, a single Sensor Board, and the required 6V and 24V power supplies. This system did not have a connector board because we used a prototype system that had a hard-wired connection on the 24V supply to provide filtering and supply the required voltage signal from the Depth Sensor.

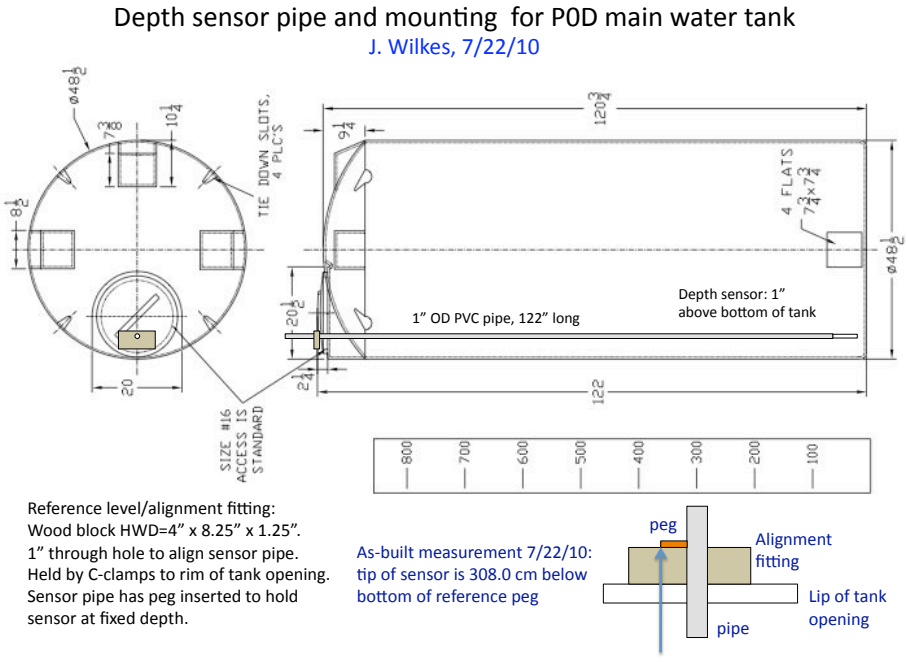

Figure 4.12: Diagram of the main tank depth sensor.

4.2.6 Drip Pan Upgrade and Leak Detector Installation

During the summer of 2012, a new drip pan was installed underneath the PØD as the old one was showing signs of wear and tear which created points in which water would collect and not drain properly. The new drip pan was designed and manufactured, with new mounting

fixtures, at Colorado State University. The drip pan is divided into four pieces named N-W, N-E, S-W, and S-E. The South sections are under the odd numbered bags and the North sections are under the even numbered bags. The East sections are under the bags 1 to 26 and the West sections are under the bags 27 to 50.

At the drain portion of each section, there is a leak detector sensor which is attached to a leak detector module. The modules detect if the sensor is wet and will send a voltage signal based on if the sensor is wet or dry. The modules are located outside the magnet next to the Main Tank DAQ. The module outputs 3.1V if no leak and 1V if there is a leak. This signal is connected to the Main Tank DAQ which transfers the signal information to the Global Slow Control. When tripped, the module will latch to 1V and an audio alarm is sounded continuously until the module is reset. The modules are labeled 1 to 4 and are connected to the N-E, S-W, S-E, and N-W sections, respectively and are shown in Figure 4.13.

Finally, the drain pipe from the drip pan had a new transparent section inserted under the magnet. This section can be removed easily and food coloring was smeared on the clear section of the pipe in order to identify water flow. Because this area under the magnet cannot be accessed when the magnet is on, a web camera with a light source was installed to transfer the image to a laptop on the SS level in order to do checks looking for water leaks.

4.2.7 Water Fill/Empty Procedure

In general, each water bladder has a separate pump that is used to fill and drain each bladder though the use of 2 separate 3-way valves. In the fill procedure, the 20 liter buffer tanks are filled separately to ensure uniform performance of the pumps, then the valves are set to allow the pump to pull water from the main tank and buffer tanks and then move the water into the PØD. The valves are reversed in order to allow the same pumps to drain the PØD as is shown in Figure 4.14. For structural reasons, the maximum deviation in water height between bladders in separate layers is 150 mm while the maximum deviation in water height between bladders in the same layer is 50 mm.

(a) Drip Pan Sections (b) Leak Detector Modules

Figure 4.13: New drip pan and leak detectors (photographs courtesy of Walter Toki).

In the original configuration, the water level was changed by 150 mm 2 layers at a time (4 bladders total). Due to the large variance in the pressure sensor combination, a slower fill and drain was needed to average over several data points. This was especially important once the water activated the fixed Binary Wet-Dry Level Sensors. These fixed points were used to check the calibration or recalibrate the pressure sensor combination. The PØD was filled until a pair of level sensors at 1900 mm above the pressure sensor were activated. The PØD was drained until the water level dropped below the drain line, which is 33 mm below the pressure sensor. As the PØD is located several meters above the pump rack, the water lines had to be purged of water to prevent a siphoning of the water bladders if a water line is damaged. This was accomplished by closing valves from the 3000 liter main tank, opening a valve to expose the buffer tank to air, and then draining the buffer tank. The remaining water in the lines were then pumped into the PØD once both level sensors at 1900 mm were wet. On average, this puts the water level at about 1920 mm above the pressure sensors which corresponds to 180 mm from the top of the water target frame.

In the upgraded configuration, the more robust depth sensors allowed all bladders to be filled or drained at the same time. In this case, the bladders were filled until the water

level was approximately 185 mm from the top of the water target frame at which point, the buffer tanks were emptied and the lines were emptied as well. The fill and drain procedure for the PØD as well as the procedure to fill and drain the Main Tank is located on the water expert webpage in the PØD operations page on `http://www.t2k.org`.

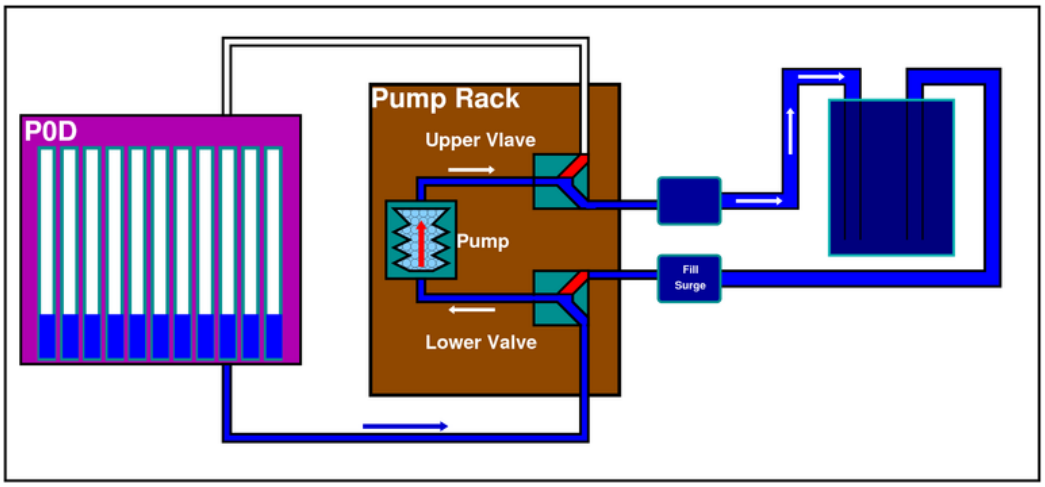

Figure 4.14: Schematic of connections to drain the PØD (image courtesy of Kevin Connolly)

4.3 Water System Performance

4.3.1 Original Configuration Performance

In the original configuration, the target water depth was measured in each bladder by reading the absolute pressure sensor at the bottom of the sensor pipe. The reading of the independent atmospheric pressure sensor located on the DAQ card on the outside of the PØD was subtracted from the submerged sensor value to determine water pressure and hence depth. The sensors were calibrated using Binary Wet-Dry Level Sensors as reference points. Without such calibration, the raw depth estimate from the Pressure Sensors had a combined uncertainty of ±136 mm based on factory specifications, dominated by the uncertainty of the atmospheric pressure sensor. Once calibrated, uncertainty in the sensor combination was found to be ±14 mm, but the calibration was found to systematically drift several centimeters over the course of several months.

After the initial target fill on March 6, 2010, two of the 50 Pressure Sensors and three of the 400 Binary Wet-Dry Level Sensors did not function correctly and by the time the targets were drained on July 27, 2010, 13 of the 50 Pressure Sensors and 22 of the 400 Binary Wet-Dry Level Sensors no longer functioned correctly. Those sensors which did function showed a change in water level on the order of 100 mm (see Figure 4.15).

We expect that the outer bags (1,2,49 and 50) will expand 5-10 mm, while the interior bags should remain stationary. In order to see if the calibration drifts over time, we could look at the average bag height just after the fill in March and just before the drain in July. A 10 mm drop in a the bag height should roughly correspond to a 1.5 mm increase in thickness so a 5-10 mm increase in thickness should correspond to a drop of 33-67 mm. The average difference is a 33 mm drop in water level. This drop would require the majority of water target bags to have expanded by about 5 mm in thickness, which would account for over 120 mm of increased thickness in the water target. As we do not observe this, we believe this trend is representative of a calibration drift with time. For these reason we replaced the existing sensors with Global Water model WL400 Depth Sensors, as described in section 4.2.4.

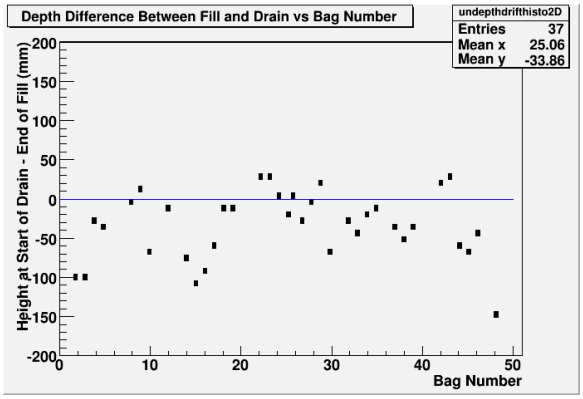

Figure 4.15: Water Level Shift from the Start to End of Run1 using Pressure Sensors

4.3.2 Upgraded Configuration Performance

With the upgraded configuration, the Depth Sensors were found to have fluctuations of ±1 mm but had a ±15 mm calibration offset before insertion into the PØD. This offset was reduced by using the fixed Binary Wet-Dry Level Sensors to provide calibration reference points in situ. We expect the water level to settle due to compression of the plastic scintillator. As show in Figure 4.16, the largest change in water level is closest to the downstream end of the PØD.

The improved stability and accuracy of the Depth Sensors allowed us to determine that during Run2, a leak in Bag 28 (north most bag in the most upstream layer of the Central Water Target) started around December 19th, 2010. This leak was confirmed by the uniform readings of the water level by both Depth Sensors in the bag, the change of state of the Binary Level sensors from Wet to Dry, and signs of water movement in the bags which are upstream and downstream of Bag 28. Details about the leak are discussed in Section 4.4.2.

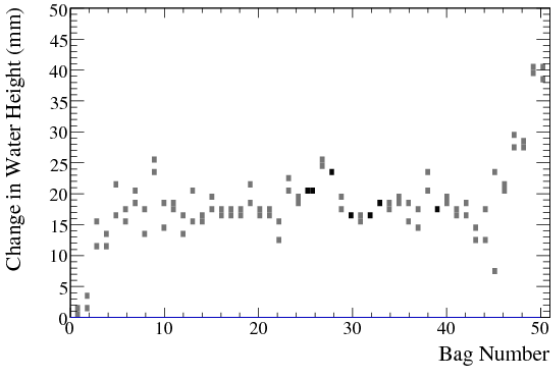

Figure 4.16: Water Level Shift After 19 Days (2 Sensors per Bag) For the Depth Sensors

4.3.3 Calibration of the Depth Sensors

The WL400 water depth sensors received from Global Water were split between the University of Colorado and the University of Washington for preliminary testing and calibration in summer of 2010 in identical testing stations. The sensors were mounted to the ends of PVC

pipe and placed in tall water tanks. Multiple sensors within a water tank were calibrated simultaneously. For a calibration, the water level within the tank was increased in stages over a 2 m range, allowing the water sensors to measure a range of depths corresponding to the expected range of depths within the PØD. The depth for each sensor at each stage was measured by eye using a ruler attached to the tank. The same DAQ system used for the water readout of the sensors in the PØD was used both at Washington and Colorado, and the current values from the sensors were recorded. A linear fit was performed to the current/depth data points and calibration constants (offset and slope) from the linear fit were recorded to convert current into depth for each sensor.

The depth sensors were packed up and shipped to Tokai upon completion of testing and calibration. A testing station was installed in the B2 level of the ND280 pit, using similar water tanks and DAQ. As a final test prior to installation within the PØD, each depth sensor was placed in the tank at a specific depth, with both the current and depth recorded. This is also when the Binary Level Sensors were attached to the pvc pipe, and these were tested at this time as well. The results of the test on B2 are show in Figure 4.17 in cm. The actual water depth was subtracted from the depth sensor reading using the calibrations from University of Washington or Colorado University. We found an underestimation of 7.8 mm $\pm$ 14.4 mm.

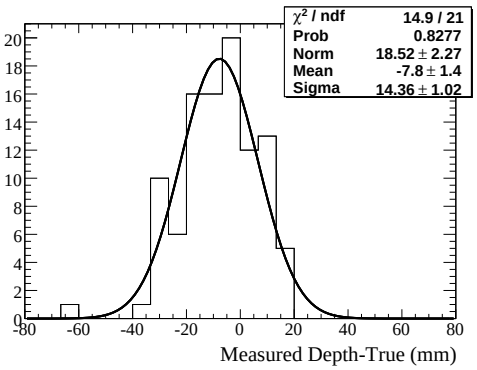

Figure 4.17: Calibrated Depth minus Actual Depth on the B2 level

4.3.4 In situ Verification and Calibration of Depth Sensors

Because the level sensors are a fixed distance from the top of the water target bladder header, we could use the level sensors as a known calibration point.

During the run 2 fill and drain, the water level passed both the high level sensor and the low level sensors. In figures 4.18(a) and 4.18(b), we show the depth sensor measurement per bag when the high or low sensors activated. These measurments were obtained by looking when the level sensors went from dry to wet and recording the distance reported by a sensor at that time. We averaged this distance with the next distance record taken immediatly before and after in order to smooth out a fluctuation.

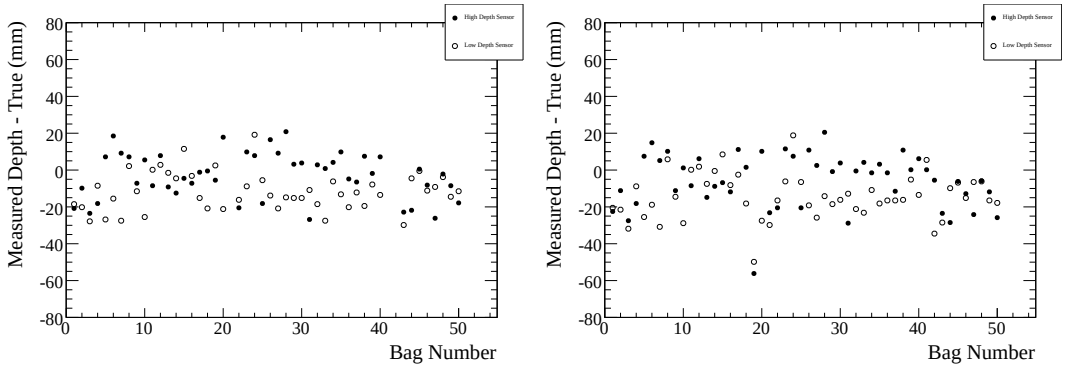

(a) High Level Sensor

(b) Low Level Sensor

Figure 4.18: Measured location minus known location of the level sensor when the level sensor went from dry to wet in the run 2 fill.

Unfortunatly, the water electronics do not sample continuously. Instead, the electronics sample once every 16 seconds during the fill and every 10 seconds during the drain. This allows for a window in time when a level sensor can switch on or off. For example, a sensor could switch on just after a previous sample, but will not be recorded until 10 or 16 seconds have passed. As a result, the rate of change of depth can add an additional potential offset which is variable across all sensors.

During the fill, the water level flow rate tends to decrease as the water level increases because of the back pressure from the partially filled bags. This can be seen in plot 4.19(a).

The flow rate was found by finding the depth change for three consequtive points and averaging the two differences. We only considered a set of points in which there was a total change of greater than 2 mm over data points. The flow rate is about 0.2 mm per second on averge when the water level is close to the top (200-600 mm from the header). This accounts for the fill rate which slows down significantly in between 200 and 400 mm. As we sampled every 16 seconds during the fill, the uncertainity in the level switch based on the sample rate is $(0.2 * 16)/\sqrt{12}$ =0.9 mm.

During the drain, there is a siphon effect that increases the flow rate significantly. In addition, the siphon is strong enough that the pumps can be turned off but the water can still drain. This is shown in plot 4.19(b) around 800, 1200, 1400, 1600, and 1800 mm from the top. At these points, most of the pumps were turned off to allow other pumps to run to achieve a uniform drain height. The flow rate is about 0.8 mm per second when the water level is close to the top (200-600 mm from the header). This accounts for the initial start of the pumps before the siphon effect. As we sampled every 10 seconds during the drain, the uncertainity in the level switch based on the sample rate is $(0.8 * 10)/\sqrt{12}$ =2.3 mm.

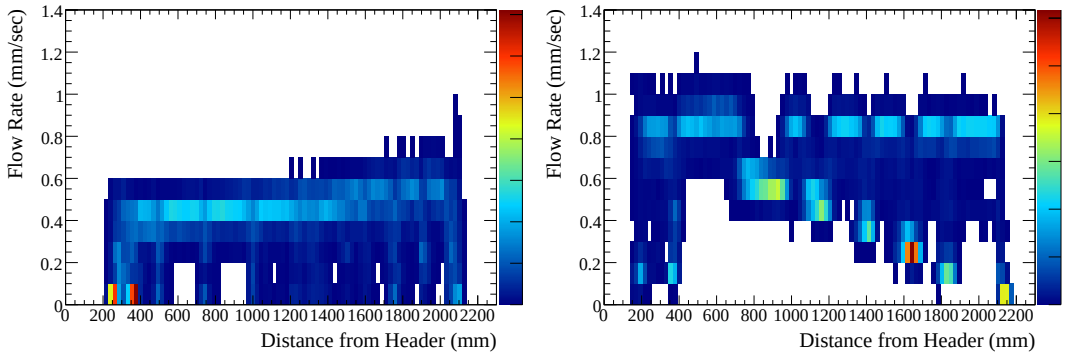

(a) Run 2 Fill

(b) Run 2 Drain

Figure 4.19: Flow Rate for All Pumps using Both Depth Sensors in the Bags. Lighter color represents more events in each histogram bin.

We find, as shown in figures 4.20(a) and 4.20(b), that on average, the depth sensors were under estimating the location by 7.5 ± 12.9 mm for the high level sensor and 10.3 ± 14.4

mm for the low level sensor. In addtion, we can look at the measured location minus the true level sensor location in both the fill and drain. The histograms are shown in figures 4.21(a) and 4.21(b). By subtracting the entries of those histograms, we find that there is a systematic shift of 22.8 ± 5.4 mm between the fill and the drain. This shift comes from several factors including a contribution from the hysterisis of the level sensors as well as the quicker drain rate.

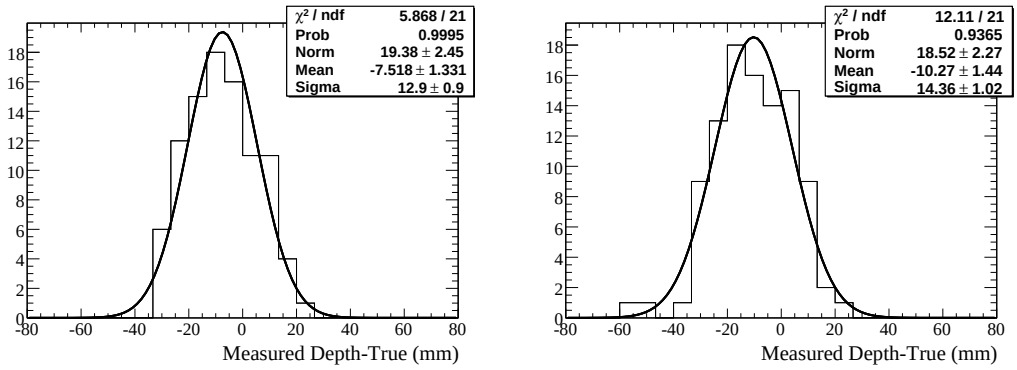

(a) High Level Sensor

(b) Low Level Sensor

Figure 4.20: Measured location minus known location of the level sensor when the level sensor went from dry to wet in the run 2 fill.

Because we have multiple level sensors, we can do a comparison between the true distance between the level sensors compared to the difference found by the depth sensors. In other words, we can compare the known distance between tow level sensors to the distance between when the level sensors change state reported by the depth sensors. The results are shown in 4.22(a) and 4.22(b). Using similar methods as previously, we find that in the fill, the depth sensors underestimate the difference by 1.4 ± 3.9 mm while in the drain, the depth sensors overestimate the difference by 3.0 ± 5.7 mm.

Finally, we can use the level sensors during a drain to compare the change in depth measured by the depth sensor and the true distance between the level sensors and an empty PØD. As before, we recorded the time when the low level sensor changed. In addition, we used 10 samples per depth sensor on the morning before the fill for the empty result for the

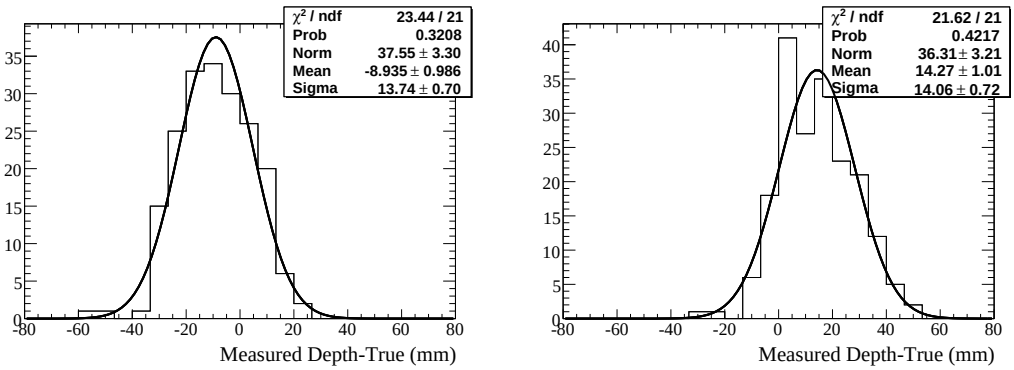

(a) Run 2 Fill (b) Run 2 Drain

Figure 4.21: Measured location minus known location of the level sensor.

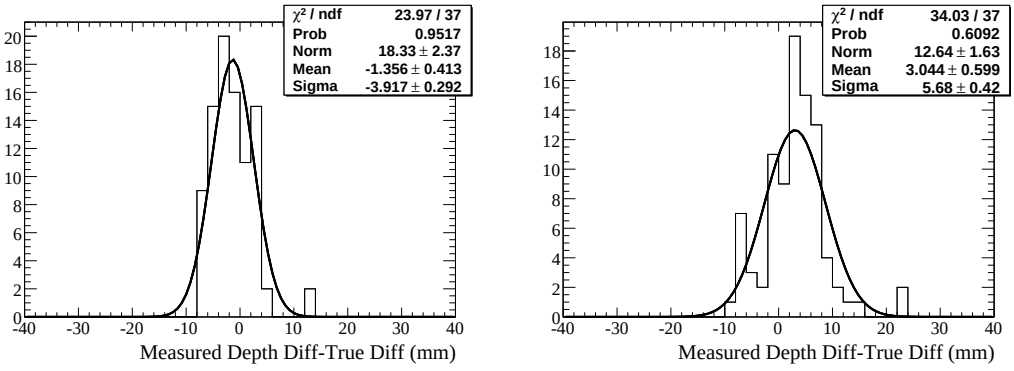

(a) Run 2 Fill (b) Run 2 Empty

Figure 4.22: Distance between level sensors measured by the depth sensors minus known distance between level sensors.

fill. For the drain, we used 10 samples taken on the morning 10 days after the drain. We waited 10 days to allow the depth sensors to stabalize and any leftover water on the depth sensors to evaporate away. The results are shown in figures 4.23(a) and 4.23(b).

Using similar methods as previously, we find that in the fill, the depth sensors overestimate the difference by 10.0 ± 12.5 mm while in the drain, the depth sensors overestimate the difference by 7.6 ± 13.3 mm. It should also be noted the depth sensors are consisent between the fill and drain. As shown in figures 4.24, the offset of the change measured in the fill minus the offset of the change measured in the drain is 1.9 mm ± 5.8 mm.

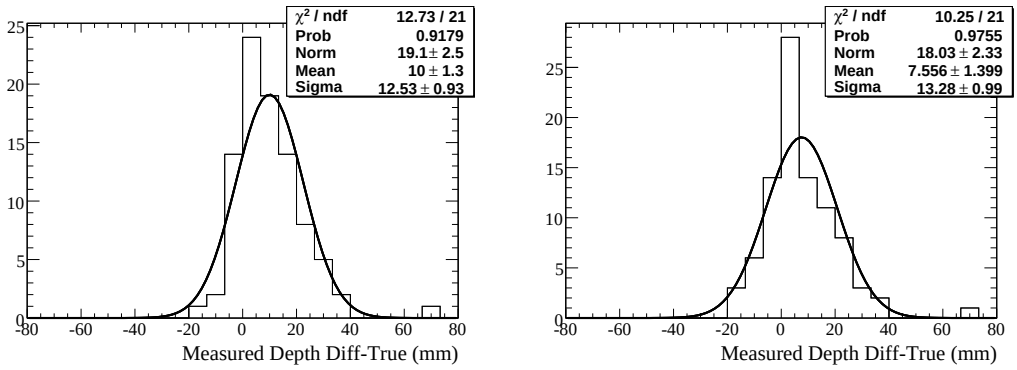

(a) Run 2 Fill

(b) Run 2 Empty

Figure 4.23: Distance between Empty PØD and lowest level sensors measured by the depth sensors minus known distance from the depth sensor to the lowest level sensor.

4.3.5 Depth Sensor Systematic Uncertainty

Uncertainty in Absolute depth

After calibration, we performed an absolute depth check on the B2 level as explained in section 4.3.3 and found that the depth sensors were underestimating the actual distance from the header by 7.8 mm ± 14.4 mm. We expected an uncertainty of at most ±5 mm just from the error in the calibration process.

Based on section 4.3.4, We noticed that that the depth sensors had an offset of 8.9 ± 13.7 mm during the fill in which the depth sensors were underestimating the distance from

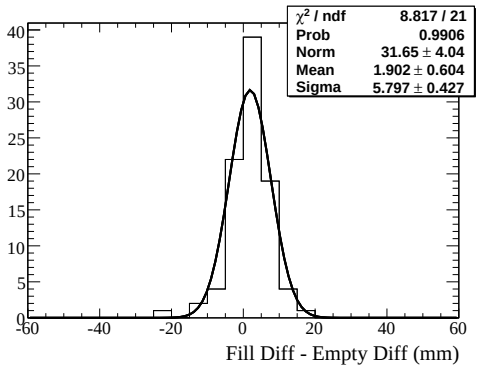

Figure 4.24: The overestimation of the Fill minus the overestimation of the Drain

the header. During the drain, the depth sensors overestimated the distance with an offset of 14.3 ± 14.1 mm. However, because of delays in reading the water electronics as explained in Section 4.3.4, we expect the actual offset is less.

Comparing with the calibrations and the above measurements, We will set an absolute uncertainty of ±15 mm to a depth sensor meaurement.

Uncertainty in Change in Depth

Based on section 4.3.4, we found a change in depth between the two level sensors was underestimated by 1.4 ± 3.9 mm during the fill and overestimated by 3.0 ± 5.7 mm during the drain for a true measured distance of 40 mm for most of the sensors. This corresponds to an underestimation of 3.5% ± 9.8% in the fill and 7.5% ± 14.3% in the drain.

However, this measurement is highly influenced by sampling rate of the electronics and the fill/drain rate. Because the flow rate is about 0.2 mm per second in the fill and about 0.8 mm per second in the drain (see Section 4.3.4), we expect that the sampling rate would be responsible for a significant portion of the uncertainity. For example, the sampling error of 0.9 mm corresponds to the error for a single level sensor to flip, so the error for two would be 1.3 mm. This corresponds to a 3.3% inherent error in the fill. The drain has a sampling error of 2.3 mm for a single level sensor flip, so the error for two would be 3.3 mm. This corresponds to a 8.3% inherent error in the drain.

Because the sampling rate contributes a large portion of the error and shift for these small measurements, we will examine the effect of measuring a change over larger distances.

We also found that the change measured from empty to the lower level sensor was an overestimation of 10.0 ± 12.5 mm for the fill and 7.6 ± 13.3 mm for the drain. This corresponds to an overestimation of 0.6% ± 0.7% of the true distance difference of 1740 mm for the fill and an overestimation of 0.4% ± 0.8% for the drain. Because of the large distance involved, the sampling rate is a smaller part of the total uncertainity (0.1% for the fill and 0.2% for the drain).

Based on these measurements, and as we plan to measure large changes in depth for the fiducial volume measurements, we will set an uncertainty on the change of depth to ±0.6% of the change of depth.

In addition, since we observe that the fill and drain give consistent results as shown in figure 4.24, even after several months, we believe that the depth sensor calibrations are not significantly drifting with time.

4.3.6 Post Earthquake Performance

The PØD was drained of water on February 14, 2011. On March 11, 2011, there was a 9.0 Richter scale earthquake off the east coast of Japan (the 2011 Tohoku Earthquake) which caused a long shutdown of the beamline and near detector. It was decided to dedicate the next run (Run 3) without water, so the first tests of the water monitoring system with water was during the summer of 2012. The initial test in July showed no physical signs of damage as there was no leaks in the plumbing system nor any leaks in the bags with the except of Bag 28 which was already known.

However, during the first test fills, it was noticed that the calibration of some of the Depth Sensors was off while other sensors were no longer stable but showed signs of large fluctuations on the order of hundreds of mm over time. Some example plots are shown in figure 4.25.

In order to safely fill the PØD and accurately determine the water level, a criteria document was established that required at last one working Depth Sensor per bag and

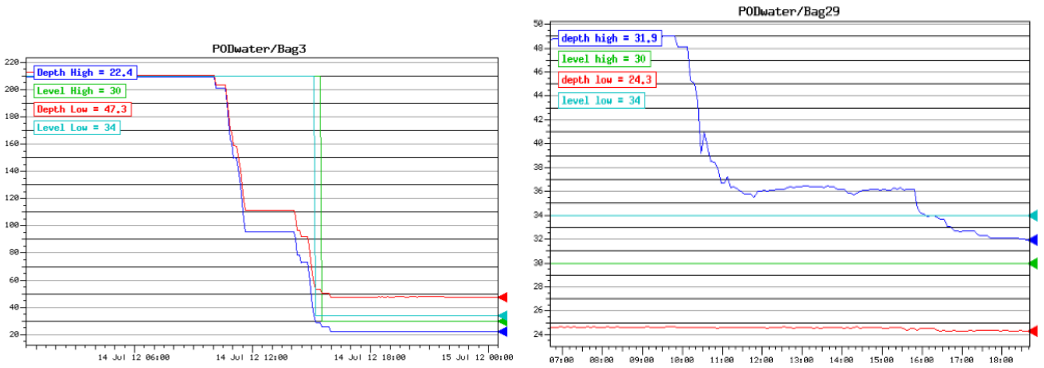

(a) Example of Calibration Offset (b) Example of Unstable Sensor

Figure 4.25: Example of Defective Depth Sensors. The y axis is distance from the top of the header in cm. Upward movement in the plot represents a decrease in water height while downward movement in the plot represents an increase in water height.

working Depth Sensors in adjacent bags. Once the PØD was filled, the sensors would be monitored to their status based on the stability of the sensor. If both sensors in a bag were judged to be unstable, then the PØD would be drained.

To fill the PØD, 18 Depth Sensors were replaced and three were refurbished while the others were recalibrated. The PØD remained full until February 6, 2013 when the PØD was drained due to a leak in Bag 43. During run 4, no new sensors became unstable while a few unstable sensors became stable and a few stable sensors had moments of instability. The full details are discussed in Section 4.4.3.

4.4 Historical Fills and Drains

4.4.1 Run 1 Height Measurements

The height of water in a water target bag during run 1 can be found three different ways: using pressure sensors, using the Binary Level Sensors, and using a physical dip stick. The Run 1 Water period started with the fill on March 4, 2010 and ended when the drain on July 26, 2010. This period does not correspond exactly to when beam was being delivered to the experiment as the PØD is usually filled and drained during beam off times.

All 50 bags had a pressure sensor which can be used to determine the height of water in the bag, but at the time of the fill, only 48 were functional and at the time of the drain, only 37 were functional. However, just before the drain, sensor board 9 was shorted by condensation, so depth and level sensors for bags 17 and 18 were not available during the drain, but we had accurate information about the water level before the drain.

The pressure sensors work by doing a subtraction of pressure in the submerged sensor to an atmospheric sensor and are calibrated to a certain zero point. The uncalibrated height reading from the sensor combination has an uncertainty of ± 136 mm as reported from the manufacturer. This large uncertainty is dominated by uncertainties in the atmospheric pressure sensor located on the sensor board and includes averaging 10 samples in order to reduce electronic noise. In principle, we could reprocess the data using more precise atmospheric pressure data from the TPC group's database. However, we can calibrate the sensor combination to a known depth and then look at the variation over time.

On March 4, 2010, all 50 bags were filled from empty until the top Binary Level Sensors read wet (only 1 reading wet was required). After one evening for setting, any bag which did not have at least one top Binary Level Sensor reading wet was filled until at least one of the top Binary Level Sensors read wet. After 10 minutes to recalibrate, the fill lines and surge tank were purged until no water was seen in the lines after several minutes. Once we were at that height, we recalibrated the pressure sensor combination and looked at the distribution over time. We took a measurement for each bag every 5 minutes over 5 days and found that the average standard deviation was 14 mm. A similar test but with no recalibration was done just before the drain and found an average standard deviation of 8.5 mm. This measurement shows that the pressure sensor has a stability on the order of 10 mm, but there can be long term drift as the sensor's calibration changes over time. During the drain, we used timing information gathered from the first Fill as well as the Binary Level Sensors to drain safely.

Another method is to use the Binary Level Sensors which where were placed at specific locations inside the water target bags. The method is to look for the highest sensor which is still wet and use the location of that sensor as a lower bound for the water height. For example, there is a Binary Level Sensor at 210 mm from the top of the header and one at

260 mm from the top of the header. If the 260 mm sensor reads wet and the 210 mm is dry, then the water level is somewhere between 210 and 260 mm. If a 210 mm sensor reads wet, then the water level is at 210 mm or greater. This provides a lower limit, but not an exact reading. During fill and drain operations, we log the time when level sensor changes state and can then compare this height to the pressure sensor for calibrations.

As a final check, a wooden dowel was inserted into certain bags in order to get a physical measurement of the water level. As the water level was physically measured and does not depend on sensors, this would be the most accurate measurement of the height, but was limited to only 6 bags which were measured by Dave Warner, Vittorio Paolone, and Scott Davis on July 2, 2010.

These 3 methods are shown in Table 4.2. The Table shows the bag number, then the depth reported by the pressure sensors at the end of the Fill in March and the Drain in July. The next column shows the location of the highest level sensor which was still wet and finally a dip stick measurement if it is available. Because we believe there is a calibration drift over time and because the pressure sensor combination was not recalibrated before the drain, there may be a systematic shift in the reported depths at the drain, which will make the calculated volume at the drain more uncertain than at the fill.

Averaging over all water target bags in the PØD, the pressure sensor combination reported a height of 211 mm with a standard deviation of 19 mm for the end of the Fill and 220 mm with a standard deviation of 48 mm for the start of the Drain. The average lower limit for all bags using the level sensors was 206 mm with a standard deviation of 16 mm and the average dip stick measurement was 213 mm with a standard deviation of 32 mm.

Table 4.2: Water level measured relative to the top of the Water Bag header in run 1 at the end of the Fill and start of the Drain. A smaller distance equates to a higher water level.

Bag	At Fill, Pressure Sensor Distance (mm)	At Drain, Pressure Sensor Distance (mm)	At Drain, Location of Highest, Wet Level Sensor (mm)	Water Distance Measured by Dip Stick (mm)
1	176	n/a	210	
2	180	288	210	
3	187	193	210	
4	192	206	210	
5	179	196	210	
6	n/a	n/a	210	
7	171	195	210	
8	172	166	210	
9	185	208	210	
10	206	284	210	
11	173	n/a	210	
12	155	204	210	
13	162	n/a	210	
14	216	305	210	
15	189	222	210	
16	170	237	210	
17	203	253	210	
18	177	189	210	
19	173	190	210	

Continued on next page

Table 4.2 – continued from previous page

Bag	At Fill, Pressure Sensor Distance (mm)	At Drain, Pressure Sensor Distance (mm)	At Drain, Location of Highest, Wet Level Sensor (mm)	Water Distance Measured by Dip Stick (mm)
20	184	n/a	210	
21	178	n/a	210	
22	180	149	210	
23	181	206	210	
24	196	207	210	
25	197	209	260	
26	204	292	260	
27	188	183	210	
28	191	182	210	
29	214	291	210	
30	218	267	210	
31	189	n/a	210	
32	194	219	210	
33	175	199	210	
34	180	194	210	
35	192	182	210	
36	179	n/a	210	
37	173	149	210	185
38	184	229	210	196
39	194	228	210	192
40	194	n/a	210	198
41	183	n/a	210	
42	185	155	210	

Continued on next page

Table 4.2 – continued from previous page

Bag	At Fill, Pressure Sensor Distance (mm)	At Drain, Pressure Sensor Distance (mm)	At Drain, Location of Highest, Wet Level Sensor (mm)	Water Distance Measured by Dip Stick (mm)
43	189	171	210	
44	202	256	210	
45	199	253	210	
46	184	223	210	
47	165	n/a	260	
48	224	360	260	
49	212	n/a	260	259
50	n/a	n/a	260	250

Flow Meter Measurement

In addition to height measurements, we did measurements of the volume of some bags using Omega FPR301[66] flow meters during the fill and drain. A flow meter is a sensor module which is inserted in the tubing to measure flow. The sensor is an impeller device which delivers one pulse per rotation. For the models we use this corresponds to 2.6 mL per pulse. Pulses are counted by a remotely located display which can be set to display instantaneous flow rate or integrated flow. The meter has an operating range from 0.07 to 5 gallons per minute (0.26 to 18.9 liters per minute) with an accuracy of 1% full scale accuracy.

In the Fill, we used 2 flow meters for bags 6 and 50. In the Drain, we used the same flow meter for bag 50, but a different flow meter for bag 6. In addition, we attached the flow meter that was on bag 6 in the fill to bag 18 for the drain. All meters used the factory calibrations which is reported as a multiplicative factor. However, tests done using a controlled setup at the University of Washington showed that the calibration was not constant with flow

rate, but changed as the flow rate diminished. In addition, it was discovered during the fill and drain that when the flow rate was sufficiently low, the impeller would not move and we would not measure flow below a certain rate. Based on these observations, we decided that the flow meters were not accurate enough for use in a volume measurement.

During the Drain, three bags were also drained into vats that could be measured directly so that the drained volume could be measured directly. We selected bags 18, 49 and 50 because bags 18 and 50 were also attached to flow meters, and the pressure sensors were not functional in bags 49 and 50. The vats were then emptied using a chemists' 5 L graduated pitcher with markings readable to about 50 mL. This was done by Jeff Wilkes and Chiaki Yanagisawa on July 26, 2010. Allowing for minor spills the total volumes should be accurate to about 500 mL. Bag 18 had 52.6±0.5 L of water removed while Bag 49 had 65.4±0.5 L and Bag 50 had 63.4±0.5 L of water removed.

4.4.2 Run 2 Measurements

Run 2 water is defined as the time period from October 27, 2010 to February 14, 2010 when the PØD was drained. During this period, the Depth Sensors showed stability to the level of 1 mm except for a set of spikes and depth change as shown in Figure 4.26. This period is defined by a sudden spike, followed by a decrease in recorded depth, followed by another spike. The Depth Sensors were stable after this point.

Aside from the "phase transition", there were few overall trends although the downstream most layers showed signs of expansion due to the water pressure. This expansion is expected as the upstream portion of the PØD is rigidly constrained by the basket support structure, whereas the downstream portion is not as rigidly constrained.

The Run 2 Water period ended due to a leak developed in Bag 28. The leak was first noticed on Dec 24, 2010 and appears to have started on Dec 19, 2010. Both Depth Sensors in Bag 28 showed a similar decreasing trend in water height, while there was signs of decreasing water height in Bags 26 and 30. We expect that as the water level decreases in a bag, then the water pressure in bags upsteam and downstream would press on the leaking bag and would expand, causing a decrease in the water level in the upsteam and downstream bags.

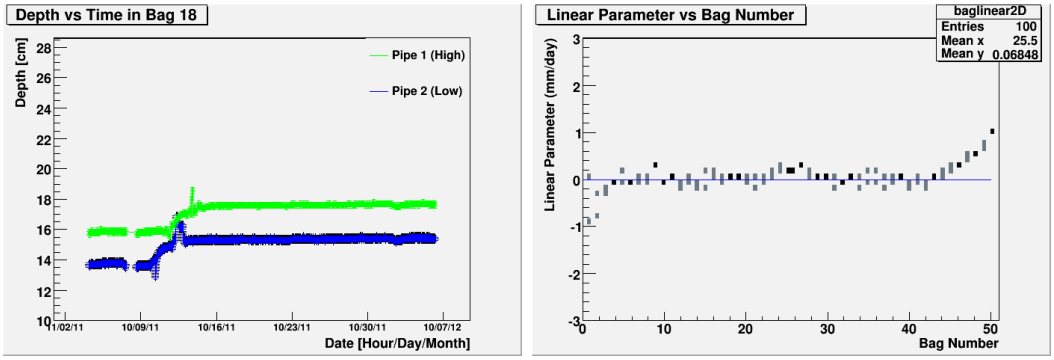

(a) Example of a "Phase Transition"

(b) Slope (mm per day) for a linear fit to the Depth Sensor height over a two week period after the initial "phase transition" after the fill.

Figure 4.26: Examples of Depth Sensor Features and Stability

There is a central support between bags in the same layer, so we would expect little change in the adjacent bag in the same layer as the leaking bag.

The leak in Bag 28 was visually confirmed around January 7, 2011 by removing the drip pan from the bottom of the PØD and observing water drops coming from the bottom of Bag 28. On January 7, Bag 28 was topped off to make sure the water level was significantly above the fiducial boundary located at 286 mm from the top of the water bag header. For reference, assuming an ideal geometry, a water level drop of 10 mm corresponds to a loss of 280 ml of water. Before the top off, Bag 28 had a leak rate around 15 mm drop in water level per day, but after the top off, we detected no water leak until January 15, 2011 when the leak rate rose to 20 mm per day but then stopped leaking around January 18 when the water level was stable again. On January 30, the leak resumed at 15 mm per day and Bag 28 was topped off on February 5th. After the February 5th top off, the leak rate increased to 30 cm per day requiring another top off on February 10th. After the February 10th top off, the leak rate increased to 45 mm per day and increased to 67 mm per day on February 13th. At this point, the PØD was drained on February 14th as there was a request to collect data with the PØD without water. The full history of Bag 28 and Bag 30 during this period are shown in figure 4.27 in which the sharp decrease in distance from the top of the header

corresponds to top off periods. During the drain, the Main Tank depth sensor went from 885 ADC to 2588 ADC while the external sight glass had a change of height of 2534±1 mm.

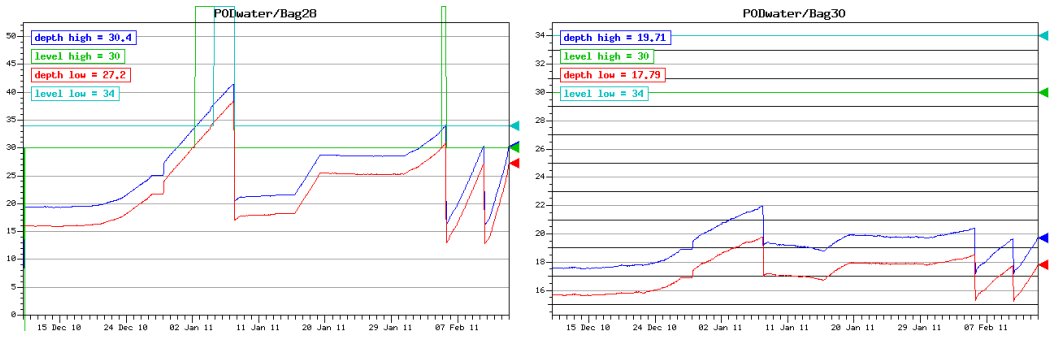

(a) Bag 28 Water Level

(b) Bag 30 Water Level

Figure 4.27: History plots showing the water level in Bags 28 and 30 from Dec 10, 2010 to February 13, 2011. The y axis is distance from the top of the header in cm. Upward movement in the plot represents a decrease in water height while downward movement in the plot represents an increase in water height.

In the table 4.3, we show the depth sensor measurement before the Fill, after the Fill (including the blowout of the lines), before the Top Off, after the Top Off, before the Drain, and after the Drain. These measurements were taking by averaging the depth sensor over 10 minutes. We defined the Before Fill period as starting at 11:00 on October 26, 2010 and the After Fill period started at 15:30 on October 27, 2010. The Before the Top Off period started at 10:00 on November 4, 2010 and the After the Top Off period started at 14:30 on November 4, 2010. The Before Drain period started at 13:30 on February 14, 2011 and the After Drain period started at 16:00 on February 14, 2011.

Table 4.3: Depth Sensor Measurements at Key Points in Run2

Depth Sensor	**Before Fill**	**After Fill**	**Before Top Off**	**After Top Off**	**Before Drain**	**After Drain**
Bag 1 High	2089.5	245.3	260.2	150.1	156.0	2105.9
Bag 1 Low	2100.5	244.9	258.8	149.4	154.0	2113.7
Bag 2 High	2098.0	245.2	257.8	148.7	160.0	2111.7
Bag 2 Low	2110.0	257.2	268.0	159.6	170.5	2121.0
Bag 3 High	2088.5	236.0	241.7	147.1	166.0	2104.4
Bag 3 Low	2098.0	241.5	245.1	151.0	168.0	2109.0
Bag 4 High	2099.0	253.2	257.5	155.5	177.0	2113.2
Bag 4 Low	2107.0	245.7	249.9	147.7	167.0	2124.1
Bag 5 High	2088.0	239.2	243.2	122.3	148.0	2101.5
Bag 5 Low	2113.5	274.1	277.8	159.6	200.5	2142.3
Bag 6 High	2091.0	248.2	251.3	125.6	152.5	2101.7
Bag 6 Low	2112.5	284.0	285.4	161.7	189.0	2126.6
Bag 7 High	2091.0	234.3	237.0	112.1	140.0	2107.6
Bag 7 Low	2110.5	273.0	275.8	153.6	181.0	2120.5
Bag 8 High	2101.0	247.1	252.5	147.3	174.0	2115.5
Bag 8 Low	2111.0	253.9	259.6	154.9	178.0	2120.7
Bag 9 High	2098.5	256.1	261.9	152.5	182.5	2112.0
Bag 9 Low	2102.0	260.6	265.9	157.0	188.5	2117.7
Bag 10 High	2082.5	236.0	238.8	127.0	150.0	2096.0
Bag 10 Low	2106.0	267.6	268.1	157.9	181.0	2117.2
Bag 11 High	2100.0	264.2	269.8	155.2	180.0	2112.2
Bag 11 Low	2103.0	257.1	261.0	146.8	171.0	2113.3
Bag 12 High	2096.0	265.0	267.9	153.0	177.0	2110.5

Continued on next page

Table 4.3 – continued from previous page

Depth Sensor	Before Fill	After Fill	Before Top Off	After Top Off	Before Drain	After Drain
Bag 12 Low	2109.0	270.5	273.7	159.1	183.0	2127.3
Bag 13 High	2097.0	260.5	264.8	153.9	178.0	2109.3
Bag 13 Low	2112.0	254.2	257.0	148.0	171.0	2122.2
Bag 14 High	2103.5	256.5	259.4	162.6	186.0	2124.3
Bag 14 Low	2107.0	249.4	251.6	155.6	177.0	2119.7
Bag 15 High	2101.0	273.9	275.6	156.4	186.0	2117.3
Bag 15 Low	2104.0	258.9	262.4	143.0	174.5	2119.3
Bag 16 High	2098.0	253.9	256.9	154.2	179.0	2112.8
Bag 16 Low	2105.0	251.3	254.8	152.8	178.0	2120.0
Bag 17 High	2097.0	243.9	247.4	143.0	169.0	2112.8
Bag 17 Low	2108.5	259.4	262.8	158.1	184.0	2120.2
Bag 18 High	2091.0	239.0	243.8	135.0	161.0	2104.0
Bag 18 Low	2103.0	261.1	264.3	156.7	182.0	2115.2
Bag 19 High	2100.5	247.0	252.0	155.5	190.0	2117.5
Bag 19 Low	2111.0	241.7	247.0	150.5	182.5	2128.0
Bag 20 High	2091.0	244.8	246.0	113.0	143.0	2104.0
Bag 20 Low	2120.0	284.7	287.4	154.8	184.0	2144.7
Bag 21 High	2086.0	217.1	227.2	149.1	181.5	2100.4
Bag 21 Low	2100.0	226.6	236.4	158.2	189.0	2119.7
Bag 22 High	2090.0	251.4	255.0	156.3	179.0	2100.3
Bag 22 Low	2100.5	248.4	252.8	152.9	178.0	2114.2
Bag 23 High	2098.5	251.1	260.3	132.0	184.0	2115.7
Bag 23 Low	2119.0	271.9	280.0	152.2	202.0	2130.4
Bag 24 High	2114.0	283.0	289.5	145.0	195.5	2125.7
Bag 24 Low	2108.0	272.7	277.3	133.0	184.0	2120.2

Continued on next page

Table 4.3 – continued from previous page

Depth Sensor	Before Fill	After Fill	Before Top Off	After Top Off	Before Drain	After Drain
Bag 25 High	2099.0	270.2	283.8	168.2	210.5	2112.5
Bag 25 Low	2106.0	256.2	270.0	155.1	198.5	2119.9
Bag 26 High	2088.0	259.8	274.2	139.2	204.0	2101.2
Bag 26 Low	2112.0	290.6	303.3	170.4	235.0	2124.7
Bag 27 High	2090.0	250.0	254.9	137.9	176.5	2105.5
Bag 27 Low	2116.0	280.1	283.4	168.1	204.0	2129.1
Bag 28 High	2100.0	253.1	261.1	132.1	310.5	2114.7
Bag 28 Low	2118.0	289.5	294.0	166.7	342.0	2131.5
Bag 29 High	2092.5	251.0	253.8	141.2	170.0	2104.7
Bag 29 Low	2119.0	269.5	273.4	161.1	188.0	2131.5
Bag 30 High	2094.0	235.0	241.0	135.9	183.0	2105.8
Bag 30 Low	2115.0	255.3	262.1	156.9	202.5	2128.8
Bag 31 High	2093.0	255.0	259.3	162.6	188.0	2108.9
Bag 31 Low	2100.0	239.3	241.8	144.6	170.0	2113.0
Bag 32 High	2092.0	238.3	242.0	141.0	167.5	2106.4
Bag 32 Low	2108.0	261.1	263.7	164.0	189.0	2120.8
Bag 33 High	2091.5	237.0	241.2	130.3	157.5	2104.6
Bag 33 Low	2121.5	267.2	269.4	160.1	188.5	2149.4
Bag 34 High	2093.0	259.4	261.9	150.5	179.0	2105.2
Bag 34 Low	2106.0	271.0	273.8	163.4	190.0	2116.6
Bag 35 High	2094.5	257.2	257.9	143.5	173.5	2109.7
Bag 35 Low	2109.0	280.4	280.7	167.2	195.0	2124.6
Bag 36 High	2101.0	241.0	243.3	147.1	171.0	2113.8
Bag 36 Low	2110.0	257.4	258.9	164.0	188.0	2123.5
Bag 37 High	2095.0	249.2	250.9	153.1	179.0	2114.7

Continued on next page

Table 4.3 – continued from previous page

Depth Sensor	Before Fill	After Fill	Before Top Off	After Top Off	Before Drain	After Drain
Bag 37 Low	2102.5	256.2	256.4	158.4	182.0	2114.0
Bag 38 High	2091.0	245.6	248.6	127.2	160.5	2107.3
Bag 38 Low	2113.0	274.6	276.9	157.7	190.0	2127.2
Bag 39 High	2098.5	253.0	256.4	161.1	190.0	2114.5
Bag 39 Low	2111.0	260.7	263.1	167.0	190.5	2118.3
Bag 40 High	2093.5	255.1	255.4	143.1	170.0	2109.2
Bag 40 Low	2108.0	277.0	278.5	165.7	191.0	2119.2
Bag 41 High	2103.0	251.3	254.2	156.6	183.5	2116.0
Bag 41 Low	2101.0	248.2	250.8	155.2	182.0	2118.7
Bag 42 High	2089.0	234.1	236.8	131.2	158.5	2104.0
Bag 42 Low	2096.0	264.6	266.7	162.5	192.0	2111.9
Bag 43 High	2102.0	230.1	237.2	151.9	180.0	2115.4
Bag 43 Low	2090.5	237.6	245.4	161.4	188.0	2102.7
Bag 44 High	2102.5	253.9	259.0	157.5	188.0	2118.5
Bag 44 Low	2083.0	237.1	239.2	139.2	170.0	2096.7
Bag 45 High	2100.5	266.9	269.7	154.8	191.5	2115.5
Bag 45 Low	2110.0	268.5	271.9	152.9	191.0	2121.5
Bag 46 High	2093.0	252.4	256.3	155.5	191.0	2105.5
Bag 46 Low	2102.0	256.9	259.2	159.4	193.0	2113.1
Bag 47 High	2093.5	254.7	265.0	160.6	210.0	2109.3
Bag 47 Low	2105.0	236.0	244.9	141.1	190.0	2117.2
Bag 48 High	2101.5	263.2	271.3	171.8	217.0	2115.4
Bag 48 Low	2111.0	264.1	271.3	171.9	215.0	2127.9
Bag 49 High	2098.0	263.0	281.0	168.0	234.5	2114.1
Bag 49 Low	2114.0	270.1	288.9	175.2	240.0	2126.3

Continued on next page

Table 4.3 – continued from previous page

Depth Sensor	Before Fill	After Fill	Before Top Off	After Top Off	Before Drain	After Drain
Bag 50 High	2095.0	264.0	282.1	191.8	240.0	2106.1
Bag 50 Low	2099.0	258.5	276.2	185.7	236.0	2114.3

4.4.3 Run 4 Measurements

Depth Sensor Stability Criteria

As reported in section 4.3.6, during the summer of 2012, we discovered that some of the Depth Sensors were no longer stable and other Depth Sensors needed recalibration. There were several test fills in the Summer of 2012 in order to determine the condition of the PØD water system after the 2011 Tohoku Earthquake as well as to test the replacement of the leaky Bag 28. During these test, each Depth Sensor was examined and repaired. The list of repairs for each Depth Sensor is shown in figure 4.28(a).

Some sensors, labeled "OK", were left with no change. Other sensors, labeled "CAL", were stable but needed recalibration in order to be more accurate. We used the Binary Level Sensors during the test fills in order to recalibrate these sensors. We decided to replace 18 Depth Sensors with new ones, labeled "NEW" and had three sensors removed and refurbished, labeled "REF", and then reinserted. We were unable to obtain enough new Depth Sensors, so some sensors that were unstable or "BAD" remained.

Using a stability criteria[1], we determined that we could safely fill the PØD and maintain stable operation as long as each bag had at least one Depth Sensor which was stable and there was a bag adjacent upstream or downstream with two working Depth Sensors. The idea is that if there was a leak in a bag, we would see similar water movement in the adjacent bag. With the addition of the leak detectors in the Drip Pan and the video feed of the drain

[1] DocDB 1499

from the Drip Pan (see section 4.2.6), this configuration would allow us to maintain the stability of the PØD water level.

During run 4, once the PØD was filled, each Depth Sensor would be examined to determine the stability status. A sensor is "Stable" if all measurements are within 10 mm over 8 hours and has not deviated over 10 mm during the week. A sensors is "Watch" if all measurements are within 10 mm over 8 hours and has not deviated over 30 mm during the week. A sensor is "Bad" if measurements vary over 20 mm over 8 hours, or more than 10 mm within 30 minutes. These sensors are very unstable and may not be useful for draining purposes. A sensor which is neither "Bad", "Watch", or "Stable" is "Unstable". Such a sensor can be used for drain as the sensor does not show sudden jumps which would make a drain difficult to monitor. If both sensors in a bag are "Unstable" or "Bad" then a drain may be required at that point.

When the PØD was finally drained, 22 depth sensors had at one point in time been listed as "Bad" or "Unstable". These sensors are listed as "BAD" in figure 4.28(b). There were 10 "Bad" sensors at the end of the fill as well as the three refurbished sensors which showed poor behavior early on. No "NEW" sensors went bad, and four "OK" sensors went bad. Also, the Depth Sensor located in Bag 37 with the High Binary Level sensor showed signs that it had shorted out and was disconnected shortly after the fill in order to avoid large current draws.

In figure 4.28(b), we also display the expected access for each Depth Sensor. The access to the top of the water headers can be obscured by overlapping TFB mounting plates, electrical ground rail, or the actual electronic mounting and cooling rails. If the access to a pair of bags (a layer) has no obstruction, that layer is labeled "Op". If a TFB mounting plate may need to be moved, the layer is labeled "T". If there is also a ground rail that may need to be moved, then the layer is labeled "T/G". Finally, if the electronics mounting and cooling rails needs to be moved to access that layer, then the layer is labeled "R".

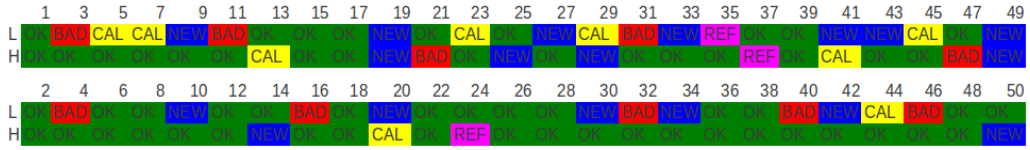

(a) Status of Depth Sensors at the End of the Fill.

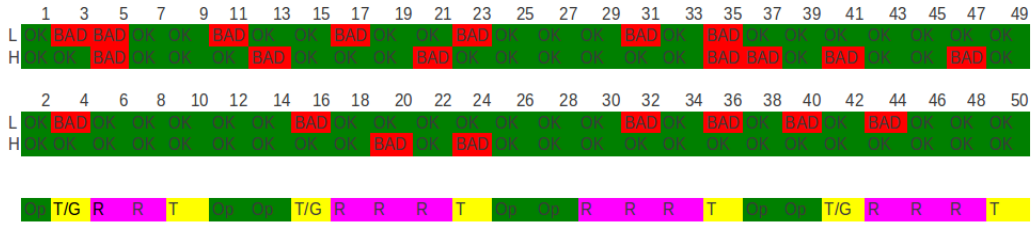

(b) Integrated status of Depth Sensors during Run 4 as well as ease of access for each sensor.

Figure 4.28: Depth Sensor status during run 4

Height Measurements

In the table 4.4, we show the depth sensor measurement before the Fill, after the Fill (including the blowout of the lines), a month after the Fill, before the Drain, and after the Drain. We defined the Before Fill period as starting at 11:00 on September 20, 2012 and the After Fill period started at 17:00 on September 21, 2012. We also include the measurement one month later at 17:00 on October 21, 2012 to represent a month of settling. The Before Drain period started at 09:00 on February 6, 2013 and the After Drain period started at 16:00 on February 6, 2013.

Table 4.4: Depth Sensor Measurements at Key Points in Run4. Entries with an asterisk are Bad Depth Sensors

Depth Sensor	**Before Fill (mm)**	**After Fill (mm)**	**1 Month After Fill (mm)**	**Before Drain (mm)**	**After Drain (mm)**
Bag 1 High	2128	158	163	154	2117
Bag 1 Low	2145	164	168	156	2114
Bag 2 High	2135	155	156	159	2123
Bag 2 Low	2082	162	159	163	2118
Bag 3 High	2107	117	125	131	2114
Bag 3 Low	**2130***	**147***	**152***	**236***	**2102***
Bag 4 High	2140	137	141	146	2117
Bag 4 Low	**2154***	**344***	**676***	**637***	**2121***
Bag 5 High	2176	209	212	256	2172
Bag 5 Low	**2102***	**219***	**714***	**660***	**2129***
Bag 6 High	2142	183	187	195	2120
Bag 6 Low	2084	124	147	152	2102
Bag 7 High	2159	201	205	210	2138
Bag 7 Low	2135	158	161	167	2125
Bag 8 High	2109	155	177	184	2122
Bag 8 Low	2119	173	178	186	2127
Bag 9 High	2129	152	178	185	2111
Bag 9 Low	2156	187	215	219	2127
Bag 10 High	2139	169	173	178	2116
Bag 10 Low	2167	170	191	198	2136
Bag 11 High	2138	147	173	179	2115
Bag 11 Low	**2118***	**372***	**358***	**284***	**2102***

Continued on next page

Table 4.4 – continued from previous page

Depth Sensor	**Before Fill (mm)**	**After Fill (mm)**	**1 Month After Fill (mm)**	**Before Drain (mm)**	**After Drain (mm)**
Bag 12 High	2138	184	187	195	2127
Bag 12 Low	2100	160	175	184	2124
Bag 13 High	2131	140	142	**128***	**2100***
Bag 13 Low	2122	177	175	183	2113
Bag 14 High	2128	182	181	187	2133
Bag 14 Low	2171	169	175	180	2124
Bag 15 High	2158	171	180	189	2128
Bag 15 Low	2156	170	175	184	2109
Bag 16 High	2131	177	170	178	2124
Bag 16 Low	**2104***	**122***	**541***	**304***	**2106***
Bag 17 High	2123	178	184	193	2123
Bag 17 Low	2106	163	**521***	**617***	**2121***
Bag 18 High	2151	136	141	149	2099
Bag 18 Low	2128	164	170	174	2123
Bag 19 High	2131	157	179	186	2144
Bag 19 Low	2114	168	190	198	2128
Bag 20 High	**2134***	**110***	**336***	**368***	**2141***
Bag 20 Low	2096	192	213	224	2158
Bag 21 High	**2221***	**689***	**1239***	**801***	**1486***
Bag 21 Low	2151	163	173	185	2117
Bag 22 High	2162	151	162	172	2117
Bag 22 Low	2103	131	155	169	2111
Bag 23 High	2130	170	186	206	2134
Bag 23 Low	2219	224	242	**471***	**2201***

Continued on next page

Table 4.4 – continued from previous page

Depth Sensor	**Before Fill (mm)**	**After Fill (mm)**	**1 Month After Fill (mm)**	**Before Drain (mm)**	**After Drain (mm)**
Bag 24 High	2128	445	59	97	2116
Bag 24 Low	2124	148	175	196	2142
Bag 25 High	**2142***	**283***	**311***	**330***	**2156***
Bag 25 Low	2129	182	196	223	2112
Bag 26 High	2125	204	214	233	2142
Bag 26 Low	2099	155	180	200	2097
Bag 27 High	2161	160	173	198	2130
Bag 27 Low	2112	150	181	203	2136
Bag 28 High	2120	165	195	211	2135
Bag 28 Low	2116	140	170	185	2119
Bag 29 High	2127	163	186	203	2142
Bag 29 Low	2140	138	141	157	2099
Bag 30 High	2171	123	136	156	2125
Bag 30 Low	2118	106	135	153	2132
Bag 31 High	2113	146	155	167	2115
Bag 31 Low	**2114***	**223***	**417***	**329***	**2098***
Bag 32 High	2147	124	133	147	2125
Bag 32 Low	**2141***	**334***	**-389***	**-418***	**1995***
Bag 33 High	2156	187	202	209	2161
Bag 33 Low	2123	170	197	199	2137
Bag 34 High	2157	183	187	193	2119
Bag 34 Low	2150	174	191	198	2122
Bag 35 High	2148	159	**290***	**426***	**2123***
Bag 35 Low	2094	**467***	**178***	113	2130

Continued on next page

Table 4.4 – continued from previous page

Depth Sensor	**Before Fill (mm)**	**After Fill (mm)**	**1 Month After Fill (mm)**	**Before Drain (mm)**	**After Drain (mm)**
Bag 36 High	2166	182	212	196	2140
Bag 36 Low	2145	192	**230***	201	2134
Bag 37 High	**2079***	**-70***	**n/a***	**n/a***	**n/a***
Bag 37 Low	2162	178	182	189	2111
Bag 38 High	2162	171	178	188	2128
Bag 38 Low	2148	155	159	168	2110
Bag 39 High	2125	175	183	188	2115
Bag 39 Low	2154	185	186	194	2119
Bag 40 High	2143	178	183	191	2124
Bag 40 Low	**2134***	**187***	**328***	**494***	**2134***
Bag 41 High	**2127***	**434***	**444***	**573***	**2115***
Bag 41 Low	2103	121	141	151	2121
Bag 42 High	2149	168	173	181	2121
Bag 42 Low	2114	151	170	174	2154
Bag 43 High	2138	159	167	217	2103
Bag 43 Low	2108	170	197	245	2121
Bag 44 High	2100	150	153	162	2087
Bag 44 Low	**2099***	**196***	**632***	**676***	**2142***
Bag 45 High	2167	155	168	196	2126
Bag 45 Low	2119	127	138	167	2099
Bag 46 High	2137	138	158	197	2108
Bag 46 Low	2088	171	205	240	2104
Bag 47 High	**2114***	**144***	**174***	193	2118
Bag 47 Low	2141	147	164	201	2108

Continued on next page

Table 4.4 – continued from previous page

Depth Sensor	**Before Fill (mm)**	**After Fill (mm)**	**1 Month After Fill (mm)**	**Before Drain (mm)**	**After Drain (mm)**
Bag 48 High	2126	165	184	222	2147
Bag 48 Low	2120	151	187	225	2117
Bag 49 High	2105	149	199	234	2127
Bag 49 Low	2093	159	202	238	2105
Bag 50 High	2106	199	238	270	2152
Bag 50 Low	2128	204	226	262	2106

During the Fill, the Depth Sensor in the Main Tank recorded an ADC value of 2629.0 counts with the PØD empty, a value of 2525.6 counts at the lower fiducical boundary, a value of 1028.9 counts at the upper fiducial boundary, and a value of 941.0 counts after the Fill and blow-out. An external sight-glass was recorded at 2810 mm at the lower fiducial boundary, then 547 mm at the upper fiducial boundary, and 415 mm after the Fill. During the Drain, the Depth Sensor in the Main Tank recorded an ADC value of 927.4 counts with the PØD full, a value of 1027.7 counts at the upper fiducical boundary, a value of 2517.0 counts at the lower fiducial boundary, and a value of 2628.0 counts with the PØD empty.

4.5 Volume Measurements

The ultimate goal of the PØD water system is to fill and drain the PØD in such a way as to find the total mass of water inside the fiducial boundary in order to find accurate cross section measurements on water. Ideally, the mass of water should be found to 1% or better in order to help limit the error on cross section in water, especially Neutral Current π^0 interactions. There are two major methods which are used to determine the amount of water in the fiducial volume: by using constrains on the PØD volume based on as-built numbers, or by determining how much water left the Main Tank when the PØD was filled

or drained.

4.5.1 Summary of P0D Geometry

The PØD design and construction is explained in Section 3.4. Because the PØD is constrained in a fixed space in the Detector Basket, one could use a known thickness of the individual PØDules in order to constrain the space available for water.

The PØD fiducial volume is defined as a region in the water target Super-PØDules which is approximately 250 mm from the edge of the active volume. This volume runs from midway through the most upstream USWT PØDule to midway through the most downstream CWT PØDule. The dimensions are 1600 mm in X, 1740 mm in Y, and 1705 mm in Z. The volume is centered at -36 mm in X, -1 mm in Y, and -2116 mm in Z using the global coordinate system.

Total length of Water Target	1741±4 mm
Thickness of USWT Cover	6.35±0.25 mm
Nominal thickness of PØDule	38.75±2 mm
Average thickness of PØDule	38.75±0.1 mm
Vertical strut horizontal dimension	18±0.5 mm
Width of the water target fiducial region	1740 mm
Height of the water target fiducial region	1600 mm
Nominal thickness of water target layer	28±2 mm
Measured thickness of USECal	304.80±0.44 mm
Nominal thickness of USECal	302.01 mm
Measured thickness of CECal	303.71±0.42 mm
Nominal thickness of CECal	302.01 mm

Table 4.5: Physical measurements of the P0D as taken during construction.

Based on as built measurements shown in Table 4.5, it is possible to determine the total length of the water target region and the expected thickness of each PØDule along with

construction measurements. The thickness of each PØDule dedicated to water is determined by the thickness of the HDPE PØDule frame. Using these measurements, Clark McGrew calculated the expected mass of water that would be in the fiducial volume.

Error with correlation limited by ECal width	3.0%
Error with fully correlated errors	7.7%
Error with uncorrelated errors	1.2%

Table 4.6: Error on Fiducial Volume Measurements.

The uncertainty of the mass depends on how the errors are correlated as shown in Table 4.6. A conservative error estimate would assume that all errors are fully correlated, but if all thickness errors are correlated, the total length of the water target region would extend into the adjacent ECal Super-PØDules. Using the position of the ECal Super-PØDules as a constraint, the total mass of water in the fiducial volume is 1884 $\pm$ 60 kg including corrections for sensors and fill/drain pipes. Note that using the known geometry has an error of 3.0%, while an error of 1.0% is preferred for analyses.

4.5.2 Calibration of the Main Tank Mass

The water added to the PØD comes from the Main Tank. By monitoring the change in the water level in the Main Tank, it is possible to determine how much water entered the PØD in total and by montioring the Main Tank level during certain period of filling, we can determine the total water added at various points.

To monitor the water level, we have plastic tubing attached to the outside of the Main Tank to act as a sight glass and we have a depth sensor inserted into the Main Tank. While we have the dimensions of the Main Tank, it was decided to perform a calibration in order to find a direct comparison to how much water mass corresponds to a specific change in water height.

The calibration procedure started by filling the Main Tank, recording the water level by both the sight glass and depth sensor, then draining the main tank into a 80 L bucket.

The bucket was then weighed with a calibrated digital scale to determine the mass of the water extracted. This procedure was repeated until the Main Tank was drained at which point the Main Tank was filled and the entire procedure was repeated a second time. This procedure was first performed by Kevin Connolly and Dave Forbush in the summer of 2011 and repeated by Dan Cherdack, Alex Clifton, Aaron Fienberg, Dave Forbush and Walter Toki in the summer of 2012. In the first calibration set, the scale was not calibrated with precision masses, while the scale was calibrated in the second calibration set. There was no noticable differences between the calibration sets.

There are two calibration constants, C_{adc} corresponding to the depth sensor and C_{sight} corresponding to the sight glass. The calibration constants can be found by fitting the measurements with a linear fit. And example is shown in Figure 4.29.

The sight glass measurement uncertainity is taken to be ± 5 mm from visual estimation. The scale (Acculab SVI-100E) has a precision of ± 0.02 kg but with a $\pm 5\%$ accuracy with no calibration. Tests with calibrated weights show that the scale used in the first calibration set was accurate to within ± 0.02 kg and the scale was recalibrated with the precision weights during the second calibration set. The depth sensors have steady state fluctuations of ± 1 mm which is typically 0.7 ADC, but can vary based on calibrations.

Based on calculations peformed by Kevin Connolly, C_{adc} is $1.612 \pm 0.012 \frac{kg}{ADC}$ and C_{sight} is $1.070 \pm 0.008 \frac{kg}{mm}$.

4.5.3 Determination of the Run 1 Total Mass

During the Run 1 fill, there was no depth sensor in the Main Tank, but there was a sensor during the drain. The volume of water from the P0D drain was either removed to separate tanks and measured accurately via the same scale used for the Main Tank calibration, or else diverted back to the Main Tank. The volume of this tank was calibrated using the inserted depth sensor, as discussed in Section 4.5.2. The change in depth was 1532 ± 9 ADC counts using the uncertainty give in Section 4.3.5. That change of ADC counts from the depth sensor translates to a change in water volume of the main tank of 2470 ± 24 kg. The water that was removed to the smaller tanks and measured via mass amounts to 181.4 ± 0.4

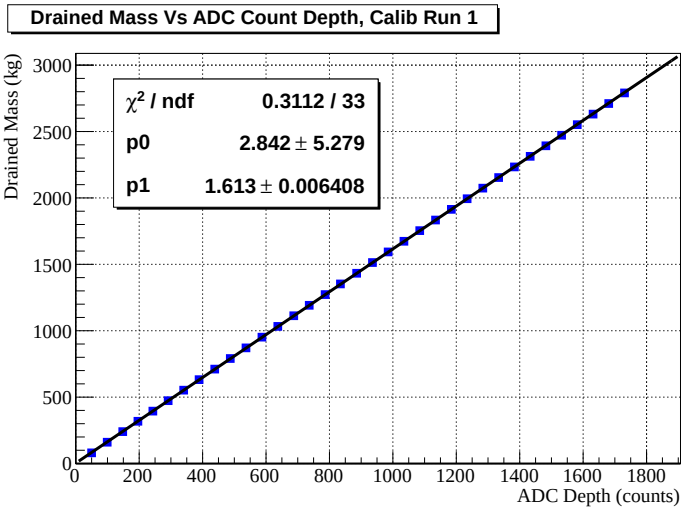

Figure 4.29: Total extracted mass versus sensor ADC count, calibration run 1 during Summer 2011 (image courtesy of Kevin Connolly).

L. Using the density of water of 0.998203 kg per L at 22 °C, this corresponds to 181.1±0.4 kg. Thus the total amount of water extracted from the P0D was 2651±24 kg.

Due to the large water height uncertainty from the pressure sensors, the geometric measurement of the water level in section 4.5.1 is the prefered value.

4.5.4 Determination of the Run 2 Total Mass

During the fill of the PØD, the depth sensor in the Main Tank was accidentally disconnected, limiting the measurement to the sight glass. The change of sight glass height was 2336±2 mm from "first contact", which is defined as the point at which the depth sensors in the PØD detect water until the water level in the PØD was above the fiducial boundary and the Main Tank was no longer being drained. Using the calibration in Section 4.5.2, this corresponds to 2499±18 kg. However, during the filling procedure, there was a small leak and incorrect settings in the pump rack. This is estimated to have diverted 14±4 kg that left the Main Tank but did not end up in the PØD and must be removed.

In addition, as a safety procedure, once the Main Tank is no longer being drained, there

is still water located in the lines going from the pump rack to the PØD. If this water is not removed, a cut in a line could drain a bag due to gravitational siphon. Therefore, the pumps are open to atomsphere and the water remaining in the lines is pumped into the PØD itself which raises the water level. To determine the mass of the blow out, we assume the water bag is a rigid structure and measure the change in the water height during the blow out. Based on measurements and calculations by Kevin Connolly and Dave Forbush, the mass of the blown out water is 40.9±4.2 kg.

Once the PØD was filled and allowed to settle for a day, it was deterimined that the water level was too close to the upper fiducial boundary and a "top off" was needed. A small amount of water was added to the PØD to raise the water level. During this procedure, bubbles formed in the sight glass which interfered with the measurement, but the depth sensor in the Main Tank was operational. The change in ADC was 98±1 ADC. Using the calibration of the main tank, the mass of water added was 157±2 kg.

On December 3, 2010, additional water was added to bags 49 and 50 because the water level had dropped due to settling close to the fiducial boundary. Because only 2 bags needed water, water was manually added using a bucket which allowed the bucket to be weighed to determine the mass added. The total water mass added was 3.84±0.02 kg. Taking the initial mass and removing the lost water but adding the blowout and topoff masses, the total water mass during the fill was 2687±19 kg.

During the drain of the PØD during run 2, Bag 28 had developed a leak and was no longer at the same height as at the end of the fill due to various top-offs. Therefore, we expect that the total mass measured at the drain will be different from the fill. There are no major corrections needed during a drain, since all water taken from the PØD goes directly into the Main Tank. The Main Tank depth sensor had a change of 1703±10 ADC during the drain, while the sight glass changed by 2534±1 mm. This corresponds to a total mass of 2745±26 kg using the depth sensor or 2711±20 kg using the sight glass.

4.5.5 Determination of the Run 4 Total Mass

During the fill of the PØD, the main tank depth sensor changed by 1688±10 ADC from empty PØD to fill and after the blow out. Using the calibration in Section 4.5.2, this corresponds to 2721±26 kg. Using the blow out value of 40.9±4.2 kg in Section 4.5.5, the total mass using the depth sensor is 2762±26 kg. The sight glass was not recorded for the total volume, so we have no measurement for the total volume.

During the drain of the PØD during run 4, the Main Tank depth sensor had a change of 1701±10 ADC during the drain, while the sight glass was not used. This corresponds to a total mass of 2742±26 kg using the depth sensor.

Chapter 5

MULTIPLE PION PRODUCTION

5.1 Introduction

In recent years there has been interest in neutrino cross section measurements. As oscillation experiments attempt to make precision measurements, systematic errors related to the Monte Carlo generators as well as background events contribute a significant portion of the error in the analysis[54]. There are several experiments measuring various cross sections of ν_μ such as Charged Current Inclusive (CC Inclusive or CCInc), Charged Current Quasi-Elastic (CCQE), Charged Current Single Pion production (CC1pi), and the Neutral Current (NC) equivalents as well as other cross section measurements such as coherent pion production[32][46]. These cross sections are experimentally defined based on the neutrino interaction with the nucleus. Table 5.1 shows what particles exit the interation nucleus from a neutrino interaction. Further information is dicussed in Section 5.2. Some experiments which have done cross section measurements are: Argon Neutrino Test (ArgoNeuT) experiment[25], CERN Hybrid Oscillation Research apparatUS (CHORUS) experiment[42], KEK to Kamioka (K2K) experiment[67][52], Mini Booster Neutrino Experiment (MiniBooNE)[16], Main INjector ExpeRiment: nu-A (MINERνA)[1][64], Main Injector Neutrino Oscillation Search (MINOS) experiment[22], Neutrino Oscillation MAgnetic Detector (NOMAD) experiment[20], NuTeV experiment[79], SciBar Booster Neutrino Experiment (SciBooNE)[15], and T2K experiment. However, there are not many modern experiments measuring Charged Current Multiple Pion production (CCNpi).

In general, CCNpi experiments from neutrinos has been limited to Deep Inelastic Scattering (DIS) measurements at higher neutrino energies. DIS has been studied in experiments such as CHORUS, MINOS, NOMAD, and NuTeV[46] to probe quarks, the weak force, and neutrino cross sections. The best measurements of CCNpi at lower energies to date are from bubble chamber experiments observing pion production from deuterium[60][41] in

Cross Section	Definition
CCInc	1 lepton, any other particles
CCQE	1 lepton, no others except for nucleons
CC1pi	1 lepton, 1 pion, no others except for nucleons
CCNpi	1 lepton, >1 pion, no others except for nucleons
NC	No leptons, any other particles

Table 5.1: Cross Section Definition

which specific pion modes are observed (see Figure 5.1). These experiments concentrated on $\pi^{\pm}$s and have few measurements involving π^0s. An inclusive multiple pion measurement, in other words a measurement in which there is more than one pion generated of any type, was not measured in those experiments but could be useful to constrain the entire multiple pion space.

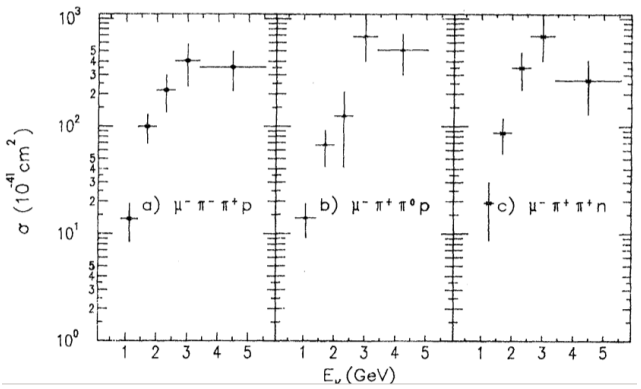

(a) ANL Cross Section[60].

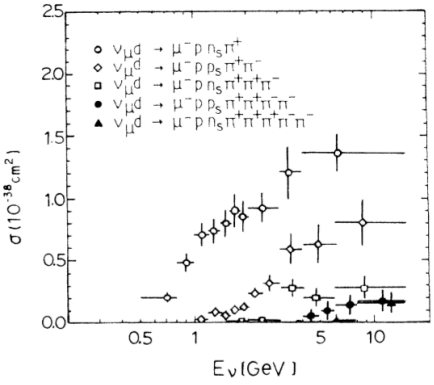

(b) BNL Cross Section[41].

Figure 5.1: Previous multiple pion cross section measurements. Plots are from the cited papers.

In addition, neutrino generators such as NEUT[56] and GENIE[26] model the CCNpi cross section with three different methods. At high hadronic invariant mass Deep Inelastic

Scattering (DIS) is used to model the pion production, while at low hadronic invariant mass a resonance model is used. A smooth transition between the two models is used in the "transition region" based on empirical data. By examining CCNpi from lower energy neutrinos, we should be able to probe this region and provide additional data. In addition, previous experiments used deuterium while the PØD is composed of a mixture of organic scintillator, brass, and water, which results in measurements on various nuclei. Specifically, by measuring the cross section when the PØD has water and when there is no water, one could get information about the cross section on water. There are no measurements of multiple pion production on water at the beam energies of T2K.

Therefore, this cross section should be explored to help further enhance neutrino generators and reduce backgrounds for other analyses. This reaction could be probed using the higher energy tail of the T2K off-axis neutrino beam, as the peak energy of the off-axis neutrino beam is too low.

5.2 Monte Carlo Generation

It is instructive to examine the process by which neutrino Monte Carlo is created in T2K. In general, the neutrino flux is first simulated, then fed into a neutrino event generator which simulates the interaction on a nucleon and outputs the particles which leave the nucleus, then GEANT[14] is used to simulate the outgoing particles as they move through the detector. A detector electronics simulation then takes the simulated particle interactions in the detector and converts interactions into electronic signals which are fed into a calibration routine in a manner similar to actual data. The generator flow is shown in figure 5.2.

The neutrino flux for T2K is generated using data from a dedicated experiment at CERN, NA61/SHINE[11][10], which measures pions and kaons coming from a similar target as the T2K target. Additional simulation input from GEANT and FLUKA[45] (2008 version 3c) is also used. The output is the neutrino flux at various distances and angles from the target which can be fed into the neutrino interaction generators. In addition, the T2K beam flux group occasionally releases flux tuning files. These tuning files are released as new data from NA61 becomes avaliable and represents a reweighting of the flux Monte Carlo. In this reweighting method, a neutrino interaction is reweighted based on the true neutrino energy

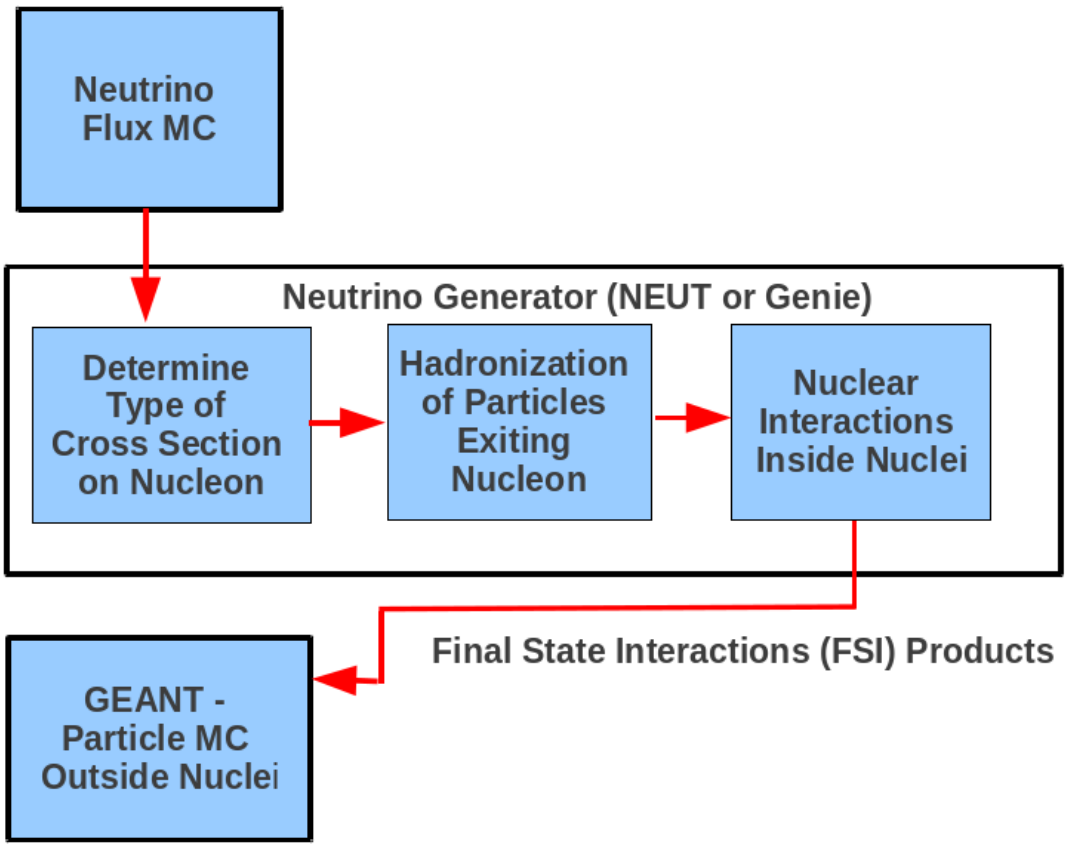

Figure 5.2: Monte Carlo Generation Flow Chart

evaluted using the updated data. In this analysis, we use the beam flux reweight version 11bv3.2.

In the T2K collaboration, two neutrino Monte Carlo generators are used: NEUT[56] and GENIE[26]. Both generators work in a similar method in which the incoming neutrino interacts with a nucleon inside a nucleus and produces several secondary particles. These particles then propagate and interact within the nucleus and then leave the nucleus. Because of the nuclear interactions, different particles may exit the nucleus than were produced from the neutrino interaction.

The neutrino-nucleon scattering is modeled using several different cross sections based on the neutrino energy. Both NEUT and GENIE use similar models, but the models are encoded differently and they may be tuned in slightly different fashions. Charged current quasi-elastic scattering is based off the Llewellyn-Smith model[62] while intermediate resonance production is based off the Rein-Sehgal model[70]. Deep inelastic scattering (DIS) is modeled using the parton functions from GRV98[51] with corrections from Bodek and Yang [34]. The hadronization from DIS is determined by PYTHIA[75] at high hardonic invariant mass (typically W>2 GeV) and empirical data tuning for lower hadronic invariant mass. In order to avoid double counting, there is a transition region in which a smooth transition is made from resonance production to DIS with experimentally tuned parameters in order to fit pion production data. Coherent pion scattering also uses the Rein-Sehgal model[71].

If the nucleon is bound in a nucleus instead of free, both models use a Relativistic Fermi Gas model based on the assumption that outgoing nucleons must exceed the fermi momentum of nucleus. A Spectral Function model is in production for both generators which would allow the nucleons to have a non-uniform momentum distribution. Once secondary particles from the nucleon interaction have formed, both generators use different cascade models to propagate the secondary particles through the nucleus and allow interactions with other nucleons. Section 5.14 describes additional parameters which are adjusted for systematic errors.

Once secondary particles leave the nucleus, GEANT4 is used to propagate these particles through the detector and to determine interactions with the detector material. The energy

depositions in the active elements of the detector are fed to the ElecSim package, which simulates the scintillation effects based on previous experiments and pre/post installation calibrations. The simulation package determines the amount of light generated from the particle interaction, and then simulates the response of the MPPC in order to produce output Monte Carlo which will have a similar data structure as actual data.

5.3 FSI and Generator Definition

In determining the constituents of a sample, it is important to define how the sample is divided up. One may define an interaction based on what particles exit the interaction on a single nucleon. Neutrino generators often define samples based on an "interaction code" which is based on the interaction of the neutrino and nucleon. However, if the nucleon is in a nucleus, there are often other interactions between the exiting particles and the other nucleons. These interactions can change the number or type of particles exiting the nucleus. All experiments can only observe particles as they exit from the nucleus in which a neutrino has interacted. We define this interaction as a Final State Interaction (FSI) and the previous as a Generator Interaction[1]. We define our FSI in Table 5.2. In this measurement, all samples are defined by the FSI unless stated otherwise.

5.4 Event Reconstruction

In order to determine physics quantities, such as particle momentum, energy deposition, distance traveled, or angle to beam axis, the raw data is fed into a reconstruction package which takes calibrated signal hits and creates general trends such as tracks or showers which have associated physics quantities and particle ID. In ND280-OA, reconstruction is first performed on a sub-detector scale and then the reconstructed objects from each sub-detector are combined into a global fit. Ideally, analyses would use the global reconstructed objects, but as of the version of software used for this analysis, production 5, the global reconstruction

[1]Due to the confusion of whether CCQE is defined as a Generator Interaction or after FSI, one could define an addition term such that CCQE refers to a interaction on a nucleon, but a measurment with a lepton and no pion is defined as "CC0pi". With this definiton, experiments actually measure a CC0pi interaction, which is mostly CCQE interactions on the nucleon, but could also contain other interactions in which pions are absorbed and do not exit the nucleus.

FSI	Definition
CCQE	1 Muon, no others except for photons and nucleons
CC1pi	1 Muon, 1 pion, no others except for photons and nucleons
CCNpi	1 Muon, >1 pion, no others except for photons and nucleons
NC	No muons or electrons
Other	Other neutrino interactions inside the PØD fiducial
Out of P0D	True neutrino interaction outside PØD
Out of P0D Fiducial	True neutrino interaction outside PØD fiducial
Sand	True neutrino interaction is outside the detector complex

Table 5.2: FSI Sample Definition

was not perfected and was not fully functional. This means that most analyses use a hybrid approach in which the global reconstruction, Global, is used for select applications while the local reconstruction, in this case PØDRecon, is used for the bulk of the analysis.

PØDRecon is designed to reconstruct physics objects in the PØD with a specific tuning to allow for π^0 reconstruction and particle ID. The fundamental reconstruction object is a hit, which represents the light output of a scintillator bar. Any bar which has a signal of at least 1 PE is considered a hit. The general procedure is to first apply a cleaning algorithm to all hits in an event. This algorithm, called PØDClean, removes hits which have a small PE signal, unless there is a neighboring hit nearby. In addition, an upper threshold cut and a timing cut requiring hits to be within 50 ns of the mean of all hits was introduced late in 2013 in order to account for hot channels (constantly large PE signals) or electronic distortion of late hits that was noticed in Data but not simulated in Monte Carlo.

After passing the PØDClean step, the remaining hits are fed into a track reconstruction algorithm. Because a hit corresponds to a scintillator bar, which runs along the x or y axis, a hit has only 2-D information. Therefore, the reconstruction first considers hits only in the X-Z or Y-Z plane independently for making 2-D tracks. In order to make 2-D tracks, the reconstruction uses a road-following algorithm with a Hough Transform seed. This

algorithm collects similar hits which are then fit by a Kalman fitter. If the Kalman fit fails, or the track crosses less than 6 scintillator layers (3 PØDules), then the hits are fit to a straight line in the 2-D view. The 2-D tracks are then matched using a score based on hit location and charge overlap. The hits from the two matched 2-D tracks are then refed into the Kalman fit to fit as a 3-D track. Once there is a set of 3-D tracks, a 3-D vertex is found by iteratively looking for track crossing points. After all tracks and vertices are found, the tracks are run through a particle ID algorithm in order to assign a general ID (Muon-like, Electron-like, or Proton-like) to each track.

After track reconstruction is finished, PØDRecon continues by combining hits which were not used in tracks as well some tracks into shower objects, which represent electronic showers and are important for π^0 identification. The methodology is similar for tracks in that hits are combined into 2-D showers which are further combined into 3-D showers along with vertex reconstruction followed by Particle ID and Muon tagging based on the decay electron. As this analysis only uses the output from the track reconstruction, we will not delve further into these algorithms.

5.5 Data and Software Used

In this analysis, we will examine the data available during the first 3 running periods that pass certain data quality cuts. These data quality cuts make sure that the beam is operating as expected and the ND280-OA is operating correctly. Run 1 started on March 19, 2010 and ended on June 16, 2010 with approximately 2.95×10^{19} protons on target (POT) after data quality cuts. The PØD was full of water during the entire run. Run 2 Water-In started on Oct 18, 2010 and continued until Feb 11, 2011 when the PØD was drained of water. There was approximately 4.25×10^{19} POT during that run. Run 2 Water-Out also started on Feb 11, 2011, after the PØD had been drained, and ended on March 11, 2011 with 3.59×10^{19} POT. Run 3 started on April 8, 2012 and ended on June 9, 2012 with 13.48×10^{19} POT and no water in the PØD. Both Data and Monte Carlo were processed using the production 5 version of the ND280-OA software. Specifically, the Data was processed with 5G (v10r11p27) while the Monte Carlo was processed with 5E (v10r11p17).

Bunch Number	Bunch Start (ns)	Bunch End (ns)
1	2700	3100
2	3280	3680
3	3860	4260
4	4440	4840
5	5020	5420
6	5600	6000
7	6180	6580
8	6760	7160

Table 5.3: Bunch Selection

5.6 Charged Current Inclusive Sample

In order to measure a relative measurement to a CC Inclusive sample, we must use a series of cuts to establish a fairly pure CC Inclusive sample. Once we have a CC Inclusive sample, a more pure Multiple Pion sample can be determined with further cuts.

In order to establish a CC Inclusive sample, we will follow a similar procedure as the PØD ν_μ group does for their Inclusive ν_μ CC measurement[2]. The general methodology is to use the PØD as a target, but use the tracker to determine an outgoing muon. The data is organized into "events" which are defined as a proton spill from the accelerator complex. A spill has either six or eight bunches, depending on the data run used. We first sort all Globally reconstructed objects in an event into bunches by using the time when the object started with a bunch window. The windows are defined in Table 5.3. In addition, each object must have a momentum at the start of the object which is not "0" or "10,000" and a status which is not "0". These are default values that show that a track was not reconstructed well.

Once the global objects are sorted, we loop over all bunches. For a single bunch, we require at least one global object start in the fiducial volume of the water target volume

[2]T2K TN–80

Type of Boundary	Lowest Boundary	Highest Boundary
PØD X Boundary	-1088.6	1016.6
PØD Y Boundary	-1142.2	1140.2
PØD Z Boundary	-3294.9	-937.1
PØD Fiducial X Boundary	-836	764
PØD Fiducial Y Boundary	-871	869
PØD Water Target Z Boundary	-2969	-1264

Table 5.4: PØD boundaries in the global coordinate system (mm).

of the PØD. This way, we ignore events that have no reconstructed global objects in the PØD or have only through-going tracks. The boundaries of the PØD are shown in Table 5.4 using a similar fiducial volume as the PØD π^0 analysis[3].

In order to establish a CC Inclusive sample, we now look over all global objects in a bunch and find the highest momentum object which also has a negative charge, uses at least the PØD and TPC1, and starts in the water target region of the PØD. This object is considered the muon candidate. Based on Monte Carlo studies in the Water-In sample, 93.8% of the muon candidates are actually muons, while 3.1% are pions with the rest a mixture of electrons or nucleons in the water-in sample. In the Water-Out sample, 92.0% of the muon candidates are actually muons, while 4.2% are pions with the rest a mixture of electrons or nucleons. Based on Monte Carlo, only 1.6% (water-in) or 1.9% (water-out) of events with a muon candidate are true Neutral Current events which means that we have a very pure CC Inclusive sample. In addition, requiring the muon candidate to start in the Upstream Water Target (USWT) reduces the NC component to only 0.6% (water-in) or 1.0% (water-out).

[3]T2K TN–73

5.7 Refining The Sample Using PØD Cuts

One we have a CC Inclusive sample, it is useful to find a reconstructed vertex and look at track topology. As pions are typically of short length (see Figure 5.3), the decision was made to look for reconstructed objects in the PØD using PØDRecon as the pions will not be well reconstructed in the Global reconstruction. From the CC Inclusive sample, we first look for a reconstructed vertex that is 3-D. This allows us to use a vertex that should have a well defined position and passed track reconstruction well. Once we have a vertex, we require that vertex to be in the PØD fiducial boundary and in the USWT. By requiring the vertex to be in the USWT, we allow particles leaving the interaction nucleus a volume in which to interact or decay. Otherwise, a vertex near the end of the PØD will have most of the particles leave the PØD which will limit the ability of the PØD to distinguish between events. Vertices in the Central Water Target (CWT) have less volume to traverse and should have less distinguishing power. This was confirmed by looking at the K-S test between some Monte Carlo observables for different interaction modes such as CCQE, CC1pi, and CCNpi based on the location of the interaction vertex as one travels downsteam. In general, the probability of distinguishing interaction modes decreases for events further downsteam.

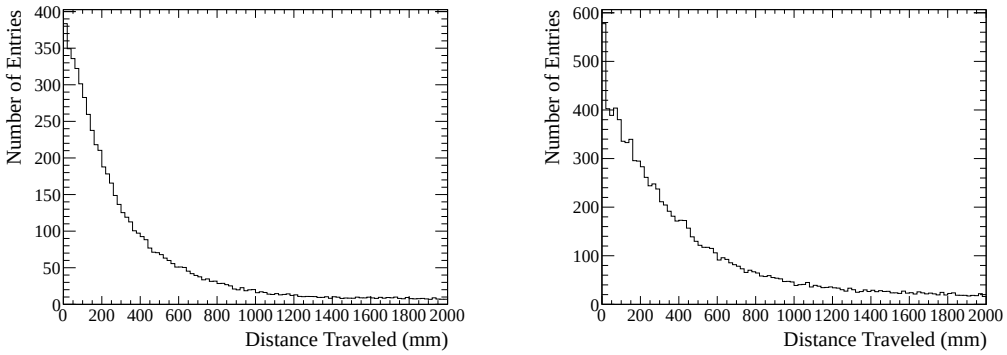

(a) NEUT Water-In

(b) NEUT Water-Out

Figure 5.3: True Distance traveled by $\pi^{\pm}$s leaving the interaction nucleus. π^{0}s travel less than 1 mm. GENIE is similar.

Once we have found a vertex in the right volume, a cut is made to make sure that all tracks are 3-D. This will give us well formed tracks. Finally, there is a cut to make sure the muon candidate starts within 100 mm of the reconstructed vertex. This cut is to make sure we do not associate the muon candidate with a secondary interaction instead of the primary neutrino interaction.

Finally, we want to try to remove events in which an interaction happened outside the PØD, but a secondary particle entered the PØD and interacted. In addition, we would like to eliminate high energy DIS events which produce large particle showers. These events are fairly well understood, whereas we are more concerned with the lower energy events. And finally, by restricting the bulk of the event to happen inside the PØD, we can use PØD observables to distinguish between various interaction modes.

One way to removed high-energy or external events is to do a containment cut in which we do not allow any particle, except for the candidate muon, to leave the PØD. Our containment cut requires that there are no reconstruction nodes in the outer two scintillator bars in the edges of the PØD, including the two most upstream PØDules. A node is a 3-D reconstruction object usually formed from a pair of hits that are matched together. We use nodes instead of hits for the containment to avoid a single 2-D noise hit from causing a rejection. For the downstream face of the PØD, the cut also requires that there be no nodes in the last two PØDules that have not been associated with the candidate muon object.

Based on Monte Carlo studies in Water-In(Water-Out), the containment cut allows 90.7%(89.1%) of true one-particle events to pass but only 40.9%(36.3%) of true two-particle events and 15.1%(11.0%) of greater-than-two-particle events, in which nucleons and photons are not considered. Based on the Monte Carlo, about 50% of the missed particles that escape are electrons with another 30% coming from charged pions. As low energy electrons and pions are often not reconstructed well, it is expected that these particle may pass the containment cut.

The results of all cuts are shown in Figure 5.4. After the cuts, the muon candidate momentum and angle from the z-axis (beam axis) is shown in Figures 5.5 and 5.6 along with the position of the vertex in X (Figure 5.7), Y (Figure 5.8), and Z (Figure 5.9). There is good agreement between Data and Monte Carlo for the muon observables as well as for

the vertex location.

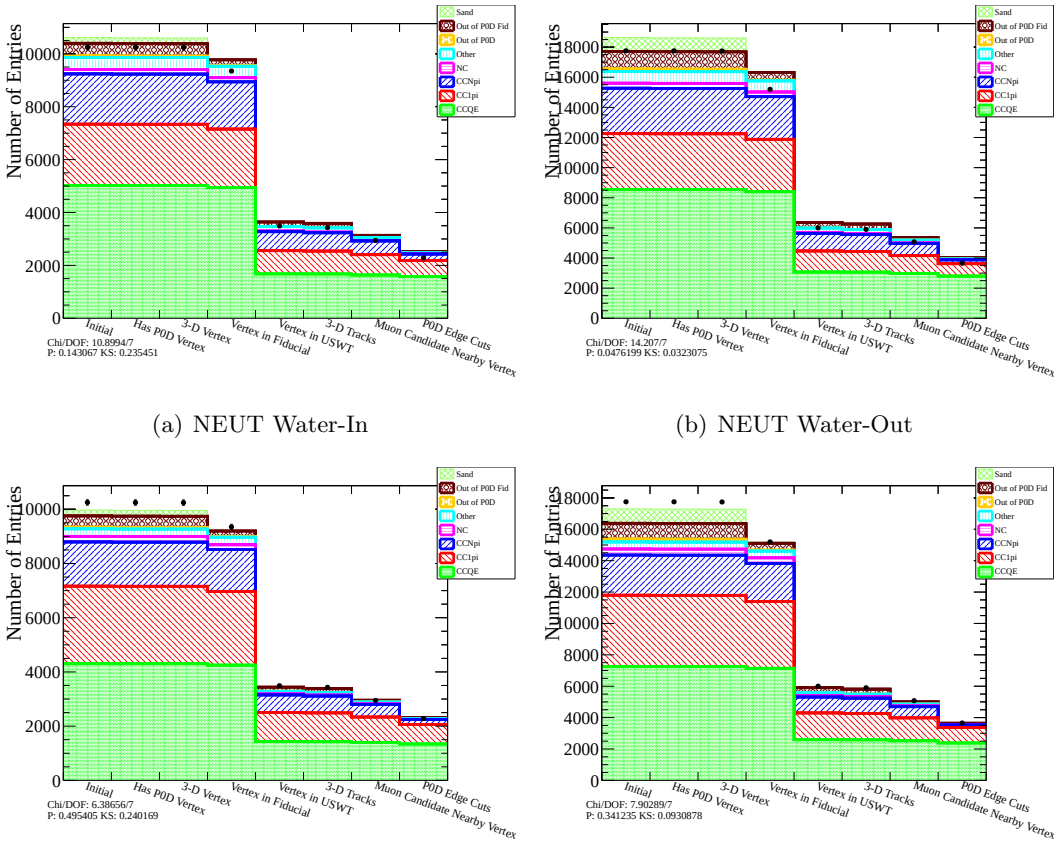

(a) NEUT Water-In

(b) NEUT Water-Out

(c) GENIE Water-In

(d) GENIE Water-Out

Figure 5.4: Number of events after each cut.

After these cuts, one could look at the track topology in order to make a cut on the number of tracks in order to have a pure CCNpi sample. In an ideal detector, CCQE would be reconstructed as one or two tracks (if the proton is reconstructed, which is unlikely in the PØD) while CC1pi can be reconstructed as two tracks (for charged pion). CCNpi will often have at least three tracks (see Figure 5.10), so a CCNpi pure sample would have a cut requiring more than two tracks. However, such a cut would still have a strong CC1pi background. We find that such a sample is 43% pure for CCNpi for water-in and 30% for water-out. The removal of water reduces the target mass, allowing particles to travel

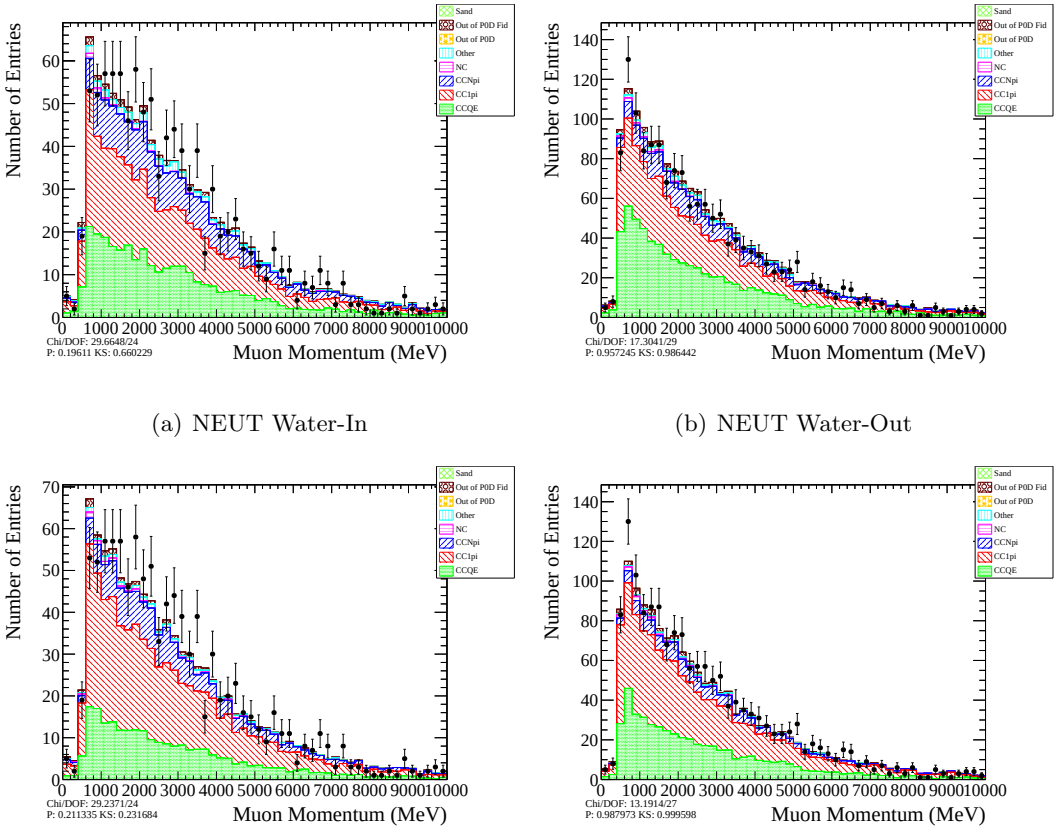

(a) NEUT Water-In

(b) NEUT Water-Out

(c) GENIE Water-In

(d) GENIE Water-Out

Figure 5.5: Muon candidate momentum at the start of the track.

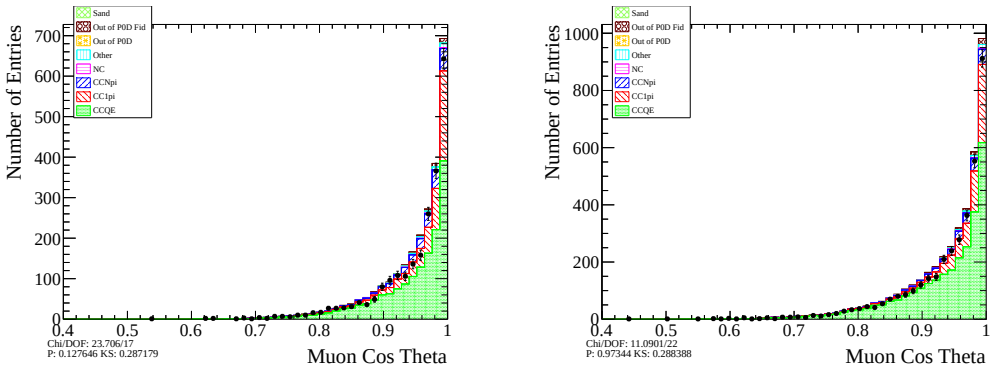

(a) NEUT Water-In

(b) NEUT Water-Out

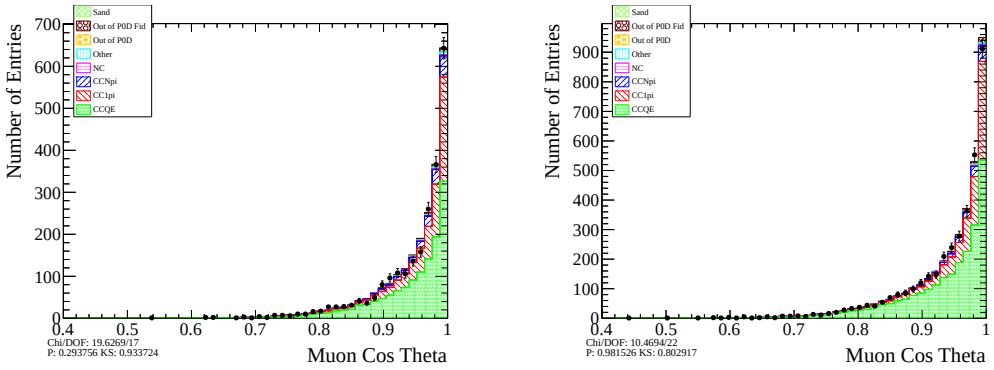

(c) GENIE Water-In

(d) GENIE Water-Out

Figure 5.6: Cosine of the angle between the start of the muon candidate track and the Z axis.

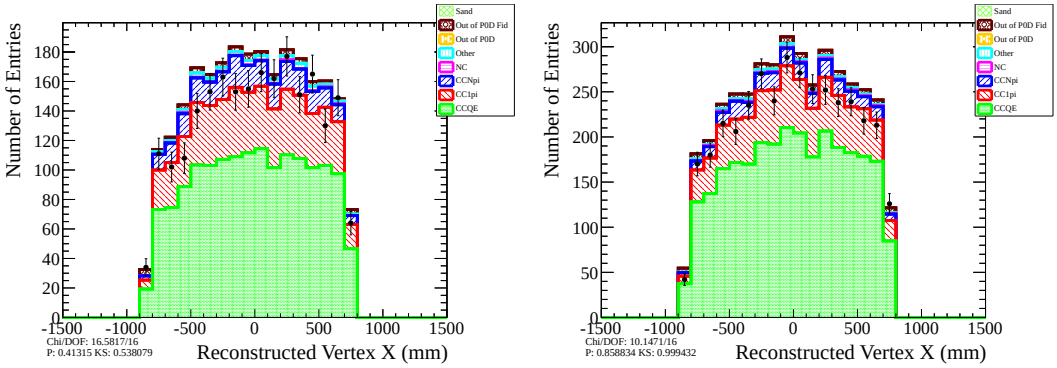

(a) NEUT Water-In

(b) NEUT Water-Out

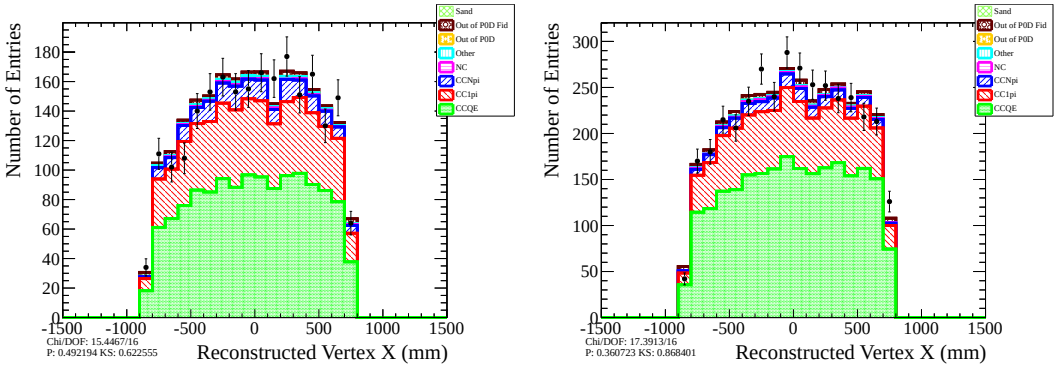

(c) GENIE Water-In

(d) GENIE Water-Out

Figure 5.7: X position of the reconstructed vertex after cuts.

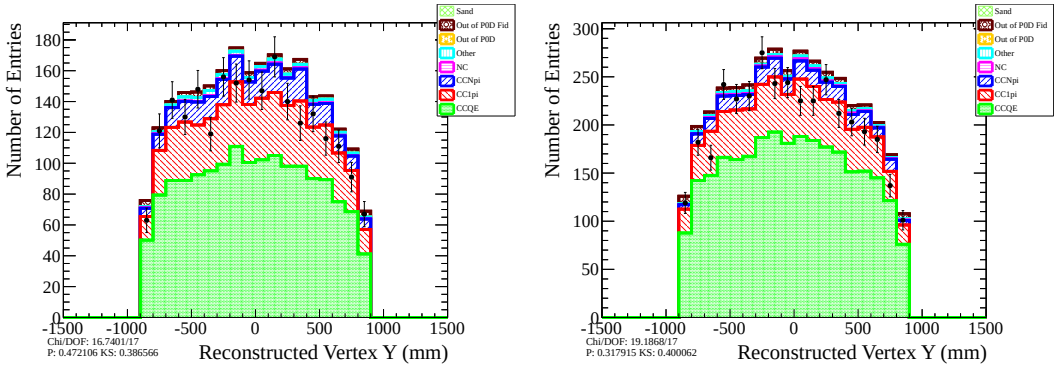

(a) NEUT Water-In

(b) NEUT Water-Out

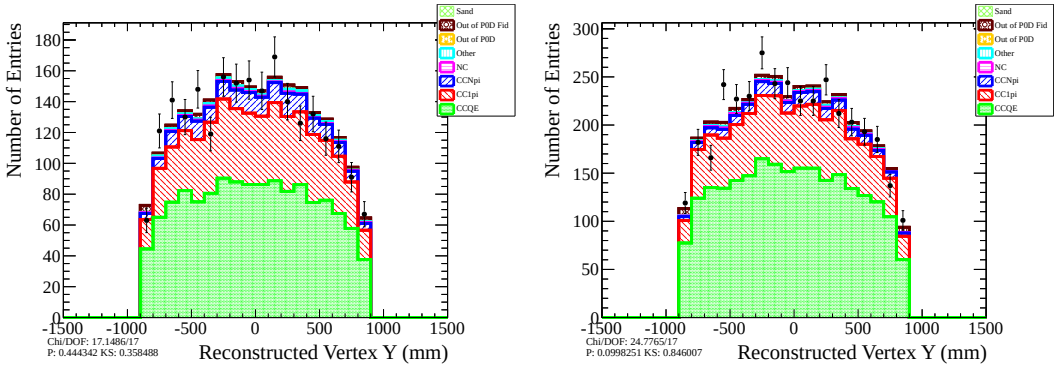

(c) GENIE Water-In

(d) GENIE Water-Out

Figure 5.8: Y position of the reconstructed vertex after cuts.

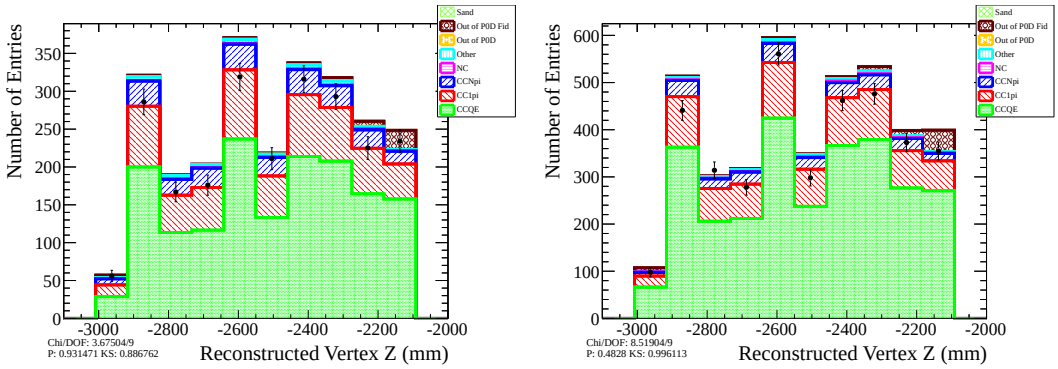

(a) NEUT Water-In

(b) NEUT Water-Out

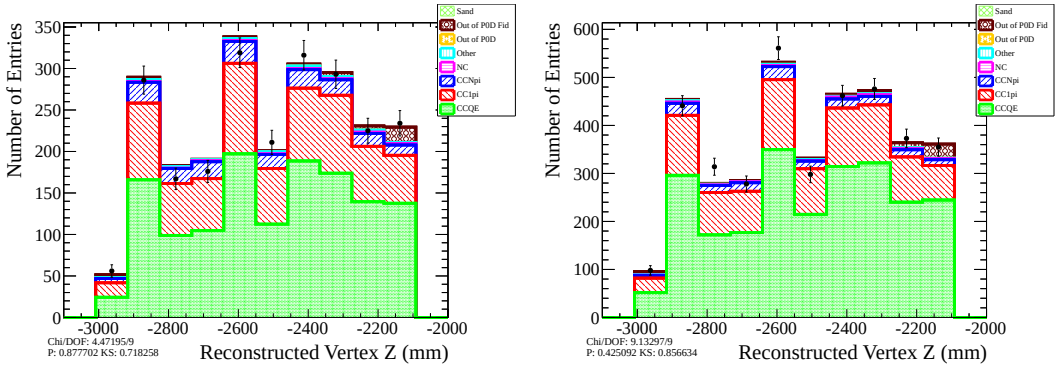

(c) GENIE Water-In

(d) GENIE Water-Out

Figure 5.9: Z position of the reconstructed vertex after cuts. Dips in both Monte Carlo and Data are effects caused by binning effects caused by discrete separation between PØDules.

further. In addition, as we would like to target lower-energy neutrino CCNpi events, we find there are few observable quantities with obvious cut boundaries. Instead, we will not use cuts to determine a pure sample, but will fit the data to Monte Carlo templates in order to determine the correction needed for Monte Carlo.

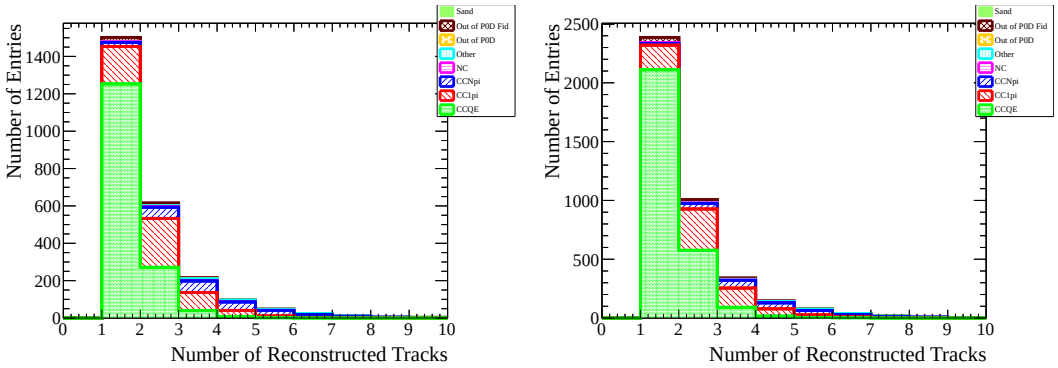

(a) NEUT Water-In

(b) NEUT Water-Out

(c) GENIE Water-In

(d) GENIE Water-Out

Figure 5.10: Number of reconstructed tracks.

5.8 Fitting Monte Carlo to Data Strategy

The CCNpi to CCInc ratio can be found by counting the number of CCNpi events in data, N_{Data}^{CCNpi}, as well as the number of CCInc events, N_{Data}^{CCInc}, then adjusting the number of events by the efficiency, ϵ^{CCNpi} and ϵ^{CCInc}, to find the true number of data events. If we

assume that the efficiency is same in Data and Monte Carlo, then the efficiency is found by finding the number of events in Monte Carlo from the analysis, N_{MC}^{CCNpi} and N_{MC}^{CCInc}, compared to the number of generated events in Monte Carlo, $N_{MCTruth}^{CCNpi}$ and $N_{MCTruth}^{CCInc}$ as shown in Equation 5.1.

$$\begin{aligned} R_{Data}^{CCNpi/CCInc} &= \frac{N_{Data}^{CCNpi}\frac{1}{\epsilon^{CCNpi}}}{N_{Data}^{CCInc}\frac{1}{\epsilon^{CCInc}}} \\ &= \frac{N_{Data}^{CCNpi}}{N_{Data}^{CCInc}} \times \frac{N_{MCTruth}^{CCNpi}}{N_{MC}^{CCNpi}} \times \frac{N_{MC}^{CCInc}}{N_{MCTruth}^{CCInc}} \end{aligned} \tag{5.1}$$

We can relate the number of events in data to a cross section because the number of events is proportional to the cross section as shown in Equation 5.2 in which σ_{target}^{CCNpi} represents the cross section on a specific target nuclei, Φ is the flux, T_{target} is the number of target nuclei, and t is the time in which data is taken. If our detector was constructed of a single target nucleus, then we could do a direct measurement of the cross section for that target as many terms cancel out in the ratio. However, as our detector is composed of multiple different target nuclei, the number of events is related to a target average cross section instead of a direct cross section on a specific target.

$$N_{Data}^{CCNpi} = \Phi t \sum_{target} \sigma_{target}\epsilon_{target}^{CCNpi}T_{target} \tag{5.2}$$

In Equation 5.3, we can adjust the generated ratio of CCNpi to CCInc from the Monte Carlo by finding the number of CCInc and CCNpi events from Monte Carlo that pass all our cuts as well as the number of CCInc and CCNpi events from Data that pass all our cuts. In effect, we are using the ratio of events that pass our cuts from both Data and Monte Carlo to create a Data to Monte Carlo ratio.

$$\begin{aligned} R_{Data}^{CCNpi/CCInc} &= \frac{N_{Data}^{CCNpi}}{N_{Data}^{CCInc}} \times \frac{N_{MC}^{CCInc}}{N_{MC}^{CCNpi}} \times \frac{N_{MCTruth}^{CCNpi}}{N_{MCTruth}^{CCInc}} \\ &= \frac{N_{Data}^{CCNpi}}{N_{Data}^{CCInc}} \times \frac{N_{MC}^{CCInc}}{N_{MC}^{CCNpi}} \times R_{MCTruth}^{CCNpi/CCInc} \\ &= R_{Data/MC} \times R_{MCTruth}^{CCNpi/CCInc} \end{aligned} \tag{5.3}$$

The number of events in Monte Carlo that pass our cuts can be determined by using the Monte Carlo truth information. In order to determine the number of Data events which are CCNpi and CCInc, we need some way to separate the Data events. We will perform this separation by first using the Monte Carlo to establish a prediction, then we will use the Data to adjust the prediction to represent the Data. To do this adjustment, we will fit Monte Carlo histograms to the equivalent data histograms using a maximum likelihood based on Poisson statistics. In essence, we will be scaling the Monte Carlo fractions of CCQE, CC1pi, CCNpi, and other reactions in order to find the best fit of Monte Carlo to Data.

Obviously, it is important to find observables which have some differential power between the various reactions, or else the fit will be undefined. Once we have defined our observables, we will do a simultaneous fit for each observable using Equation 5.4[32] as our negative likelihood which we will minimize using Minuit[58] within the ROOT framework[35]. In Equation 5.4, we sum over all bins, i, in our observables for both data and Monte Carlo ("expected").

$$-2\ln L = 2\sum_i (Nexp_i^{Scaled} - Ndata_i + Ndata_i \ln \frac{Ndata_i}{Nexp_i^{Scaled}}) \tag{5.4}$$

For the expected Monte Carlo events in each bin i, we use equation 5.6 when we are using all true neutrino energies. We scale the Monte Carlo template by a factor, $R^{template}$, which is a floating parameter in our fit. It should be noted that for fitting purposes, we have combined the Other, NC, Out of PØD, Out of PØD Fiducial, and Sand templates into a single Other template. In general, the Other template is small compared to the remaining templates, so we can treat the individual components as one template. However, if the Other template is large, then the individual components should be separated to allow additional freedom to account for variations within the individual Other templates.

$$Nexp_i^{Unscaled} = N_i^{CCQE} + N_i^{CC1pi} + N_i^{CCNpi} + N_i^{Other} \tag{5.5}$$

$$Nexp_i^{Scaled} = R^{CCQE} \times N_i^{CCQE} + R^{CC1pi} \times N_i^{CC1pi} + R^{CCNpi} \times N_i^{CCNpi} + R^{Other} \times N_i^{Other} \tag{5.6}$$

Once we have fit our observables to data and obtained the individual scale factors, we can use Equation 5.7 to determine the data to Monte Carlo ratio, R, for this relative ratio. Once we have the overall data to Monte Carlo ratio, we can use the last equation in Equation 5.3 to determine the corrected relative cross section.

$$\begin{aligned} R_{Data/MC} &= \frac{N_{Data}^{CCNpi}}{N_{Data}^{CCInc}} \times \frac{N_{MC}^{CCInc}}{N_{MC}^{CCNpi}} \\ &= \frac{\sum_i R^{CCNpi} * N_i^{CCNpi}}{\sum_i Nexp_i^{Scaled}} \times \frac{\sum_i Nexp_i^{Unscaled}}{\sum_i N_i^{CCNpi}} \end{aligned} \tag{5.7}$$

5.9 Observables for Fitting

We need observables which show some difference between the various Monte Carlo templates in order to allow the fit to adjust to data. After exploring several parameters, two observables seem to show the most promise. As we require containment of all tracks except the muon candidate in the PØD, we can look at the longest contained track to see any difference in templates. Naively, we would expect that a CCQE event would have a shorter contained track than other interactions because we would expect that track to be a proton. Both CC1pi and CCNpi would have longer pion tracks, but if there are more overall tracks, then we could expect that the CCNpi tracks might be longer due to higher energy or the CC1pi events are coming from events with a π^0 in which case we have shorter tracks from showering electrons.

In Figure 5.11 we show the length of the longest contained track in a sample with only two tracks. In Figure 5.12 we show the length of the longest contained track in a sample with more than two tracks. In general, there is a shape difference between CCQE and other modes in the two-track sample, and a small shape difference between CCNpi and other modes in the greater-than-two sample. In Appendix A we have included plots in which all modes are normalized to unit area.

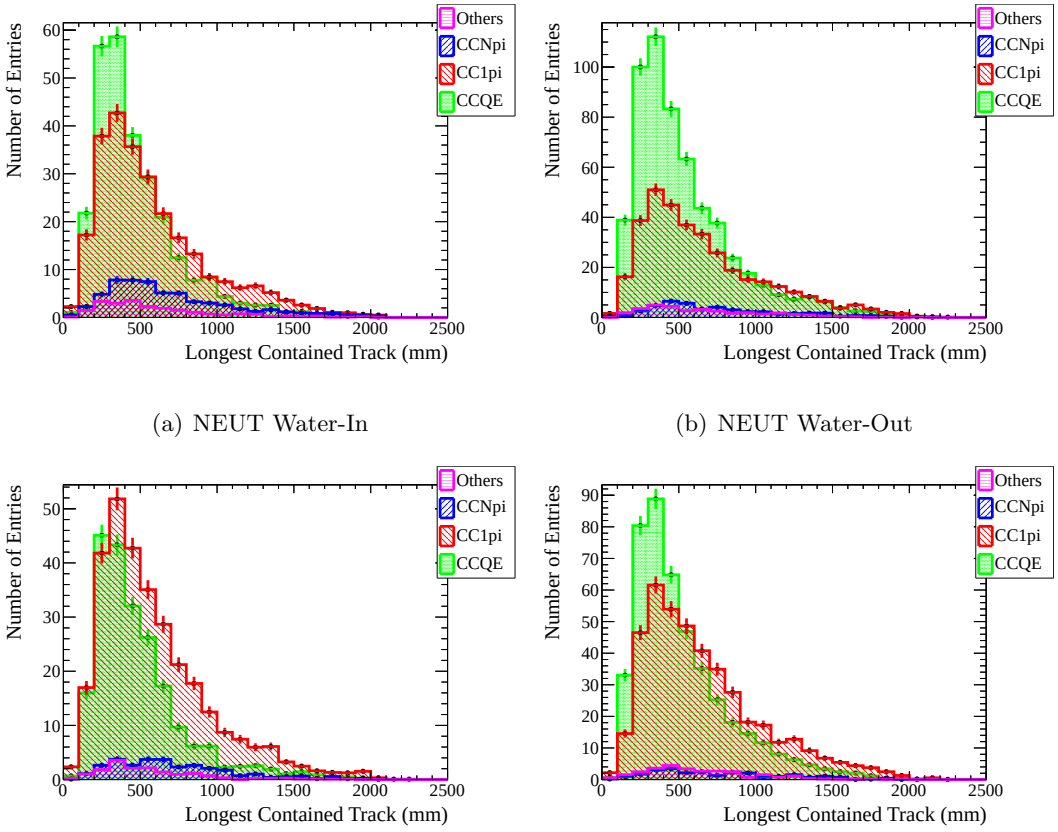

(a) NEUT Water-In

(b) NEUT Water-Out

(c) GENIE Water-In

(d) GENIE Water-Out

Figure 5.11: Longest contained track for events with 2 tracks

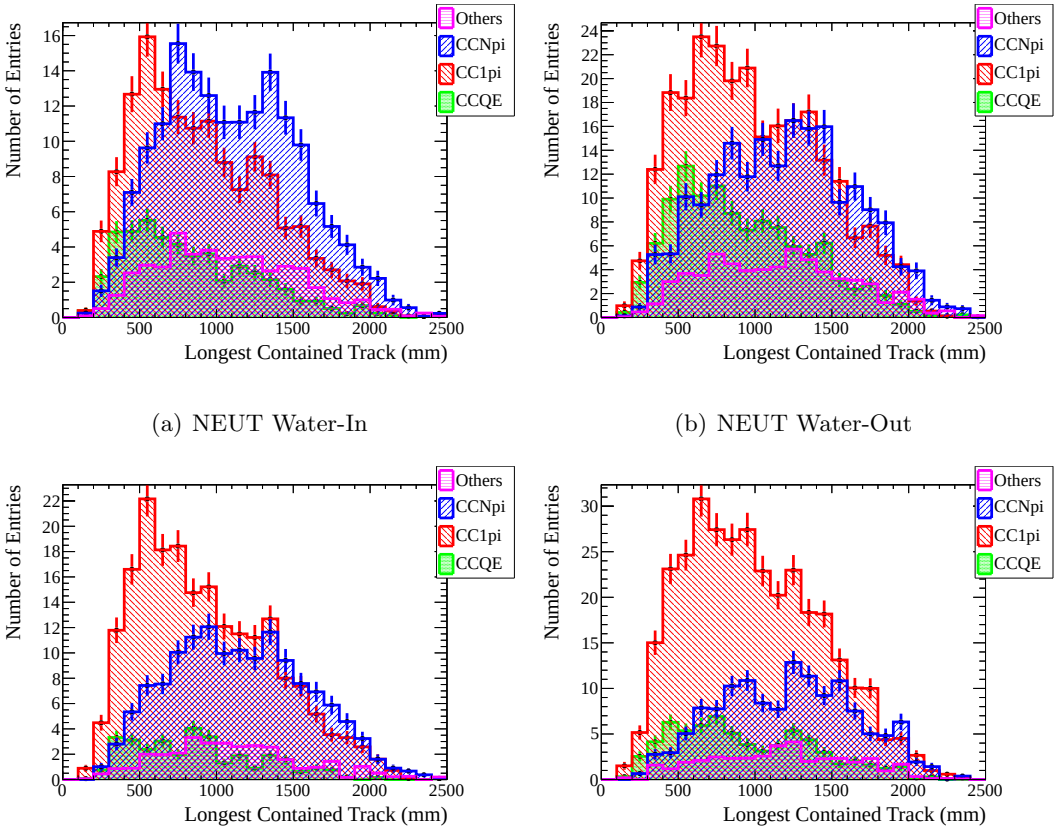

(a) NEUT Water-In

(b) NEUT Water-Out

(c) GENIE Water-In

(d) GENIE Water-Out

Figure 5.12: Longest contained track for events with >2 tracks

Another observable we have looked at is hits nearby the reconstruction vertex. We expect that at lower energies, CCNpi will produce shorter pions which will deposit energy in the detector, possibly scatter, and may not be reconstructed well. By looking at the total number of hits nearby the reconstruction vertex, we can get some information about possible unreconstructed tracks nearby the vertex. To do so, we looked for hits that come from the Clean algorithm in PØDRecon which is described in Section 5.4. By looking at the Clean step, we get all non-noise hits even if they are not used in the track reconstruction. We look for clean hits in a region defined as a triangular region within 9 bars and 3 layers of the reconstructed vertex.

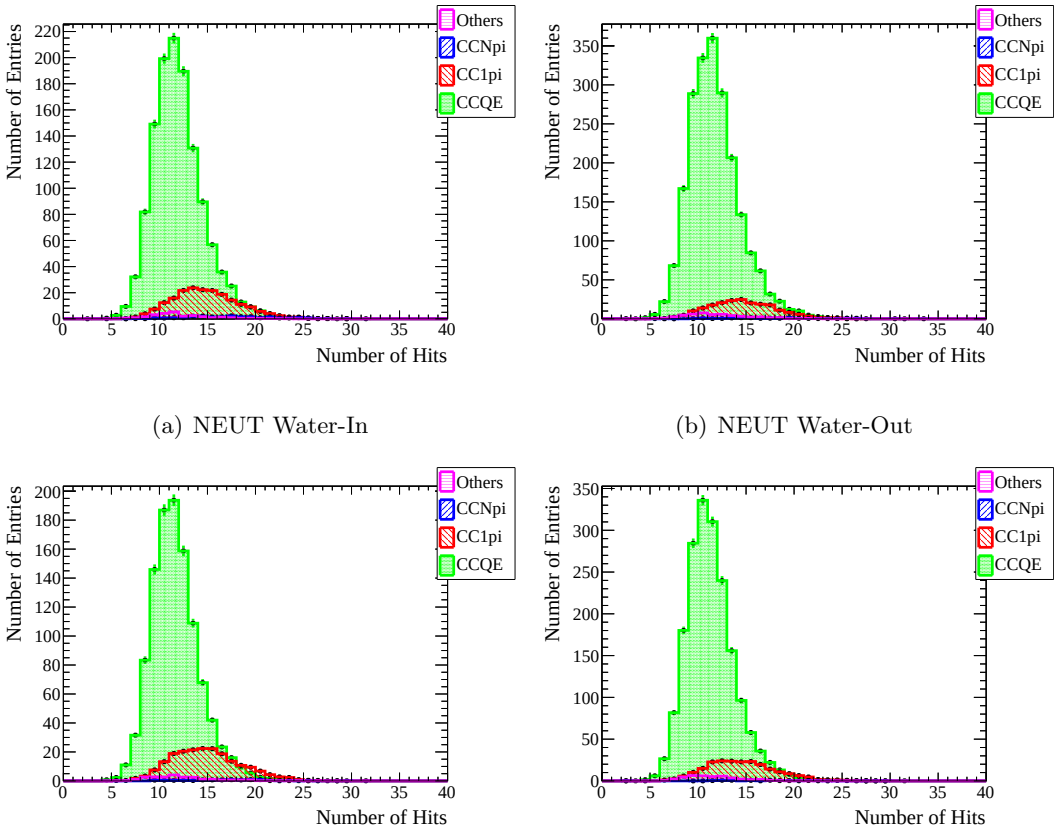

(a) NEUT Water-In

(b) NEUT Water-Out

(c) GENIE Water-In

(d) GENIE Water-Out

Figure 5.13: Number of hits nearby the reconstruction vertex for events with 1 track

In Figure 5.13 we show the number of hits nearby the vertex in a sample with only one track. This sample is heavily dominated by the CCQE mode, so we can use this sample to set the CCQE normalization.

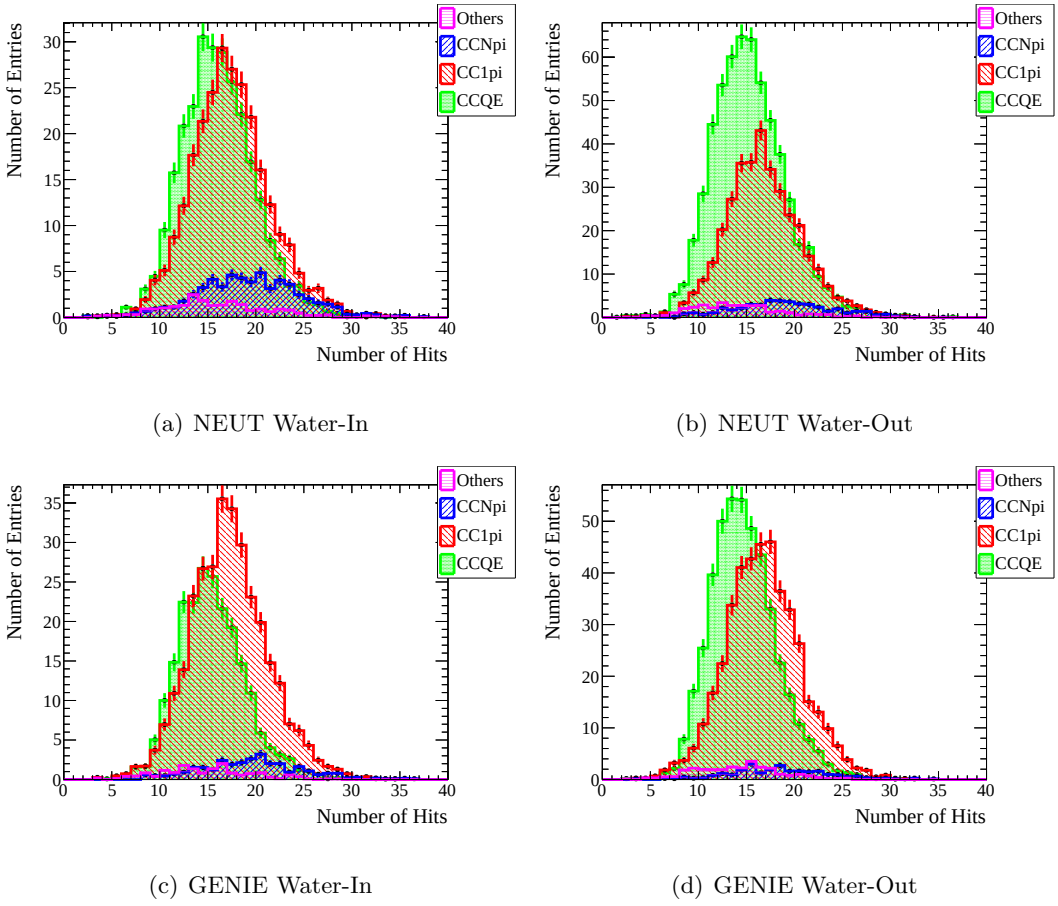

(a) NEUT Water-In

(b) NEUT Water-Out

(c) GENIE Water-In

(d) GENIE Water-Out

Figure 5.14: Number of hits nearby the reconstruction vertex for events with 2 tracks

In Figure 5.14 we show the number of hits nearby the vertex in a sample with only two tracks. In Figure 5.15 we show the number of hits nearby the vertex in a sample with more than two tracks. In general, there is a subtle difference between CCQE and CC1pi in the samples, but there is an obvious shape difference between CCNpi and other modes. In Appendix A we have included plots in which all modes are normalized to unit area.

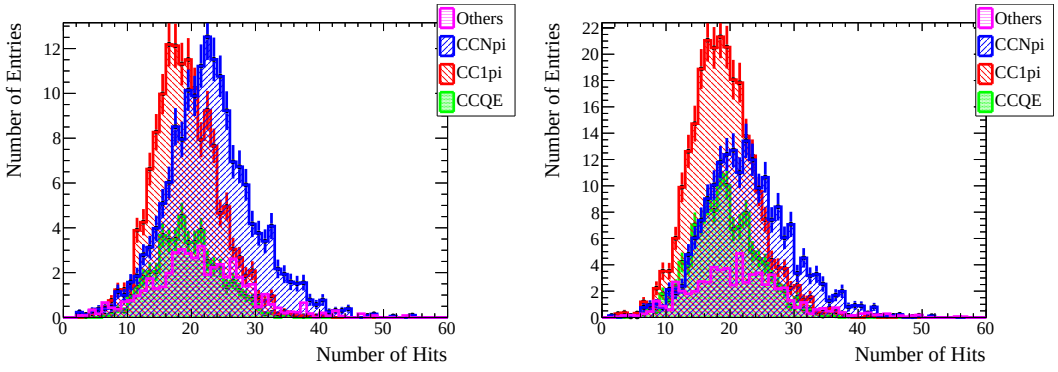

(a) NEUT Water-In

(b) NEUT Water-Out

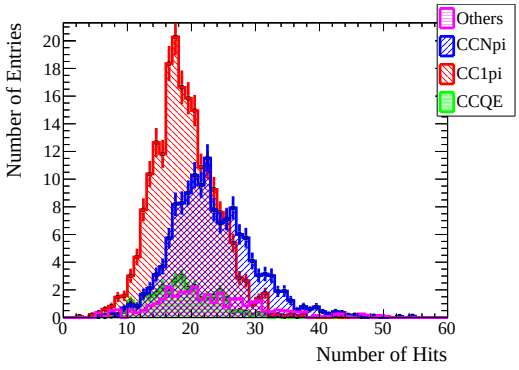

(c) GENIE Water-In

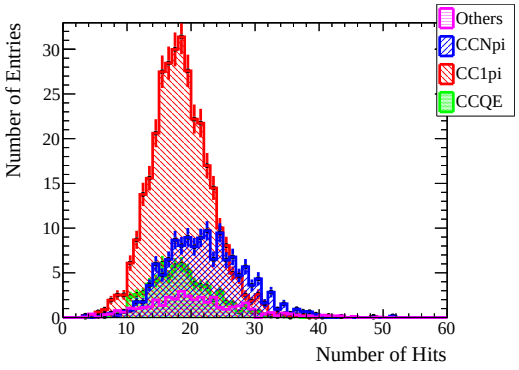

(d) GENIE Water-Out

Figure 5.15: Number of hits nearby the reconstruction vertex for events with >2 tracks

5.10 Fitter Verification and Binning

As a test of the robustness of the fitter and to determine if the fitter has any bias, we fit the Monte Carlo templates to the same templates that have been varied within statistical fluctuations. We then repeat this procedure 200,000 times and fill a histogram using the pull for each fit. The pull is defined in Equation 5.8. The pull histogram is fit using a gaussian to find the mean and sigma. If the fitter is correctly identifying statistical fluctuations with no bias, then the mean should be 0 and the sigma should be 1. The pull for all four samples, NEUT Water-In, NEUT Water-Out, GENIE Water-In, and GENIE Water-Out, are performed independantly of the others using their own Monte Carlo templates.

$$Pull = \frac{R_{fit} - R_{true}}{\sigma_{fit}} \tag{5.8}$$

In the process of verifying the fitter, the likelihood for each throw can be histogramed. This histogram can be fit with a χ^2 distribution in order to find the Number of Degrees of Freedom (NDoF) expected for the Monte Carlo templates. This distribution can be used to compare to the likelihood resulting from fitting the data.

	Pull Mean	Pull Sigma	Best Fit χ^2 NDoF
NEUT Water-In	0.019±0.002	0.998±0.002	184.6
NEUT Water-Out	0.016±0.002	0.992±0.002	107.6
GENIE Water-In	0.010±0.002	0.962±0.002	176.0
GENIE Water-Out	-0.003±0.002	0.957±0.002	152.7

Table 5.5: Pull Mean and Pull Sigma

This procedure was also used to determine the binning used for each sample. The above method was repeated for a wide range of binning for the observables. The binning selected was the one with a mean pull between -0.2 and 0.2 which had the largest separation between the Monte Carlo templates. We also required the binning to yield a likelihood between 100 and 200 in order to prevent binnings which were too coarse or too fine. The selected binning is shown in Table 5.6 while the pull results for that binning are shown in Table 5.5.

	2 Track Len	>2 Track Len	1 Track Hits	2 Track Hits	>2 Track Hits
NEUT Water-In	178.6 mm	208.3 mm	4 Hits	4 Hits	5 Hits
NEUT Water-Out	277.8 mm	250.0 mm	4 Hits	10 Hits	6 Hits
GENIE Water-In	166.7 mm	227.3 mm	4 Hits	4 Hits	5 Hits
GENIE Water-Out	250 mm	208.3 mm	4 Hits	4 Hits	5 Hits

Table 5.6: Binning

5.11 Side Band Study

Ideally, if the detector is simulated perfectly in the Monte Carlo, then any difference between the Data and Monte Carlo would be attributed to physics quantities. However, since the simulation is not perfect, it can be important to do a comparison between Data and Monte Carlo to look for detector effects which may not be simulated correctly. In order to look for detector effects, we examined a side band sample defined as events in which there is no global track which uses TPC1. This is the exact opposite of the critera used for our samples. We use all other cuts described in Section 5.7 although we have no muon candidate to use so there is no cut regarding the muon candidate distance to the reconstructed vertex.

Figures 5.16, 5.17, 5.18, 5.19, and 5.20 show the same fit observables as will be used in the analysis although we do not use the longest contained track, but the 2nd longest contained track. We use the 2nd longest contained track because the Monte Carlo distrubtions in the signal and side band are more similar. In the side band sample, we have more particles which escape the containment (20% compare to 7% corresponding mostly to low energy muons) so the longest contained track can represent an escaped particle which are not as common in the signal sample. As a result, in the side band sample, the longest track distribution is wider with a peak at a longer length than in the signal Monte Carlo sample. However, the 2nd longest contained track has a peak in a similar location to the signal Monte Carlo sample so we will use that to look for detector effects. Tables C.1, C.2, C.3, and C.4 located in Appendix C show how the Data and Monte Carlo compare based on a χ^2 test as well as a Kolmogorov Smirnov (KS) test.

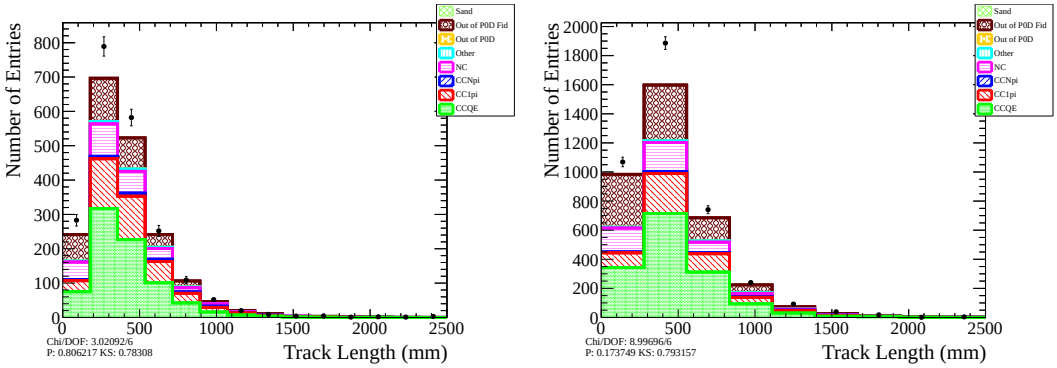

(a) NEUT Water-In

(b) NEUT Water-Out

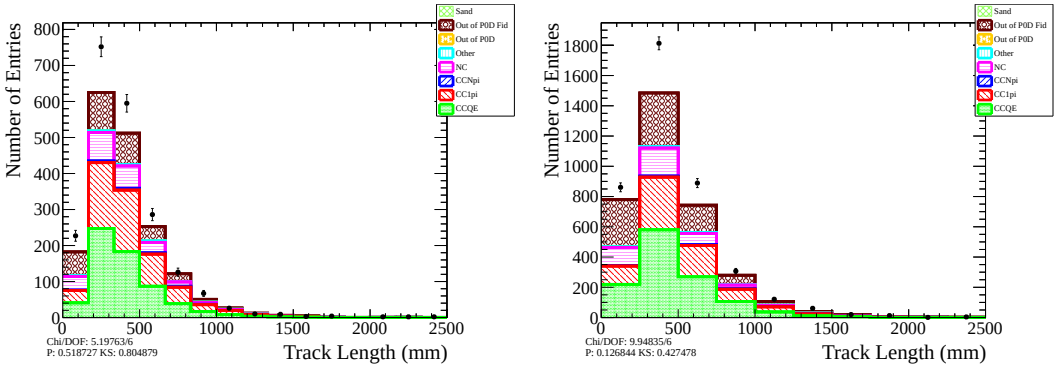

(c) GENIE Water-In

(d) GENIE Water-Out

Figure 5.16: Length of the 2nd longest track for side band events with 2 tracks.

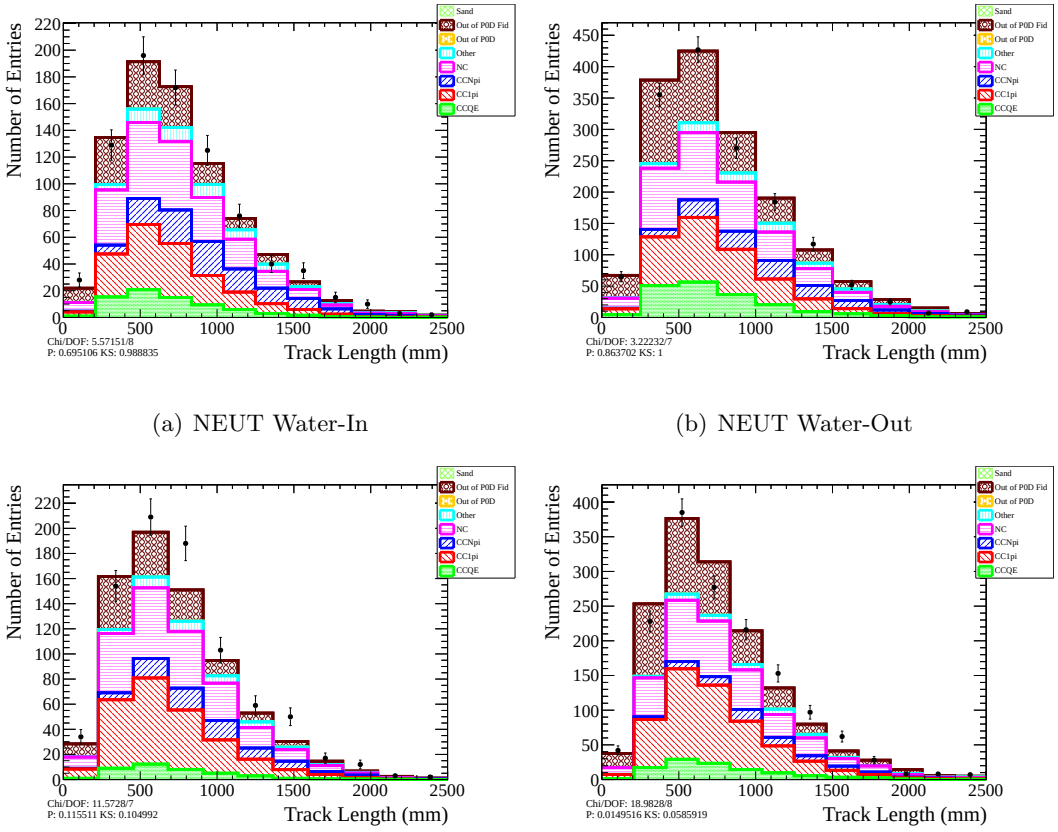

(a) NEUT Water-In

(b) NEUT Water-Out

(c) GENIE Water-In

(d) GENIE Water-Out

Figure 5.17: Length of the 2nd longest track for side band events with >2 tracks.

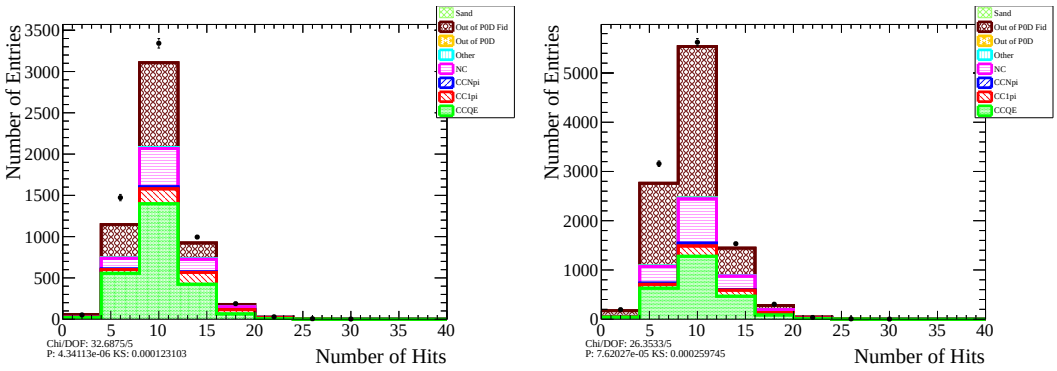

(a) NEUT Water-In

(b) NEUT Water-Out

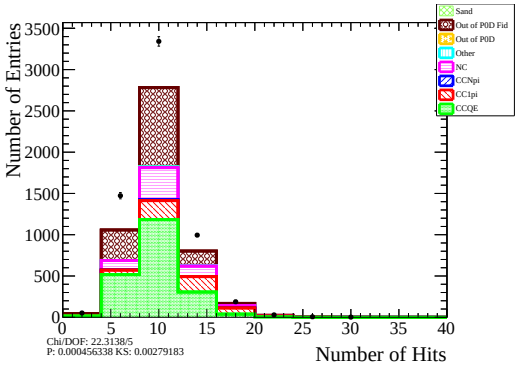

(c) GENIE Water-In

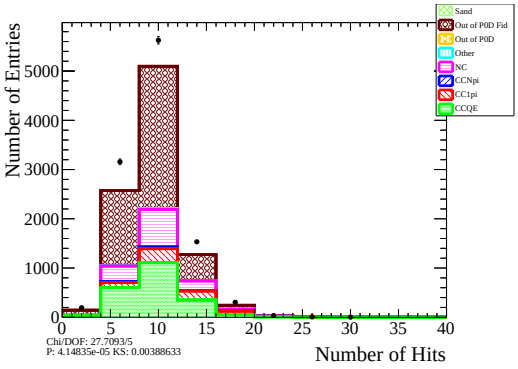

(d) GENIE Water-Out

Figure 5.18: Number of hits nearby the reconstructed vertex for side band events with 1 track

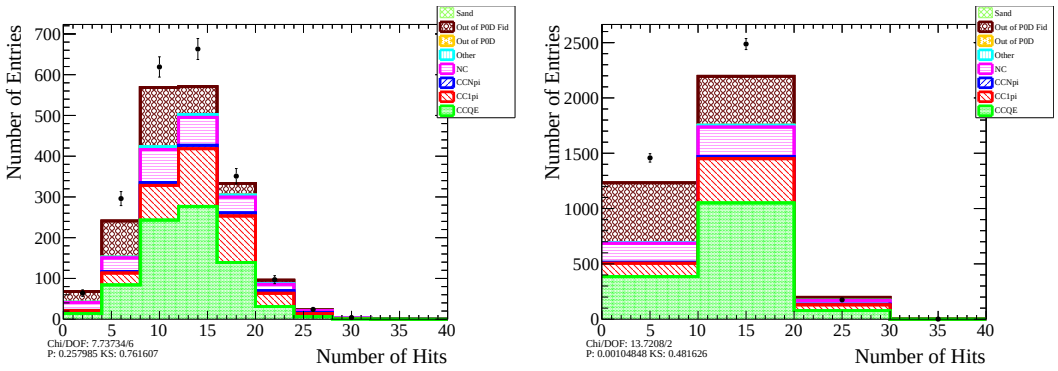

(a) NEUT Water-In

(b) NEUT Water-Out

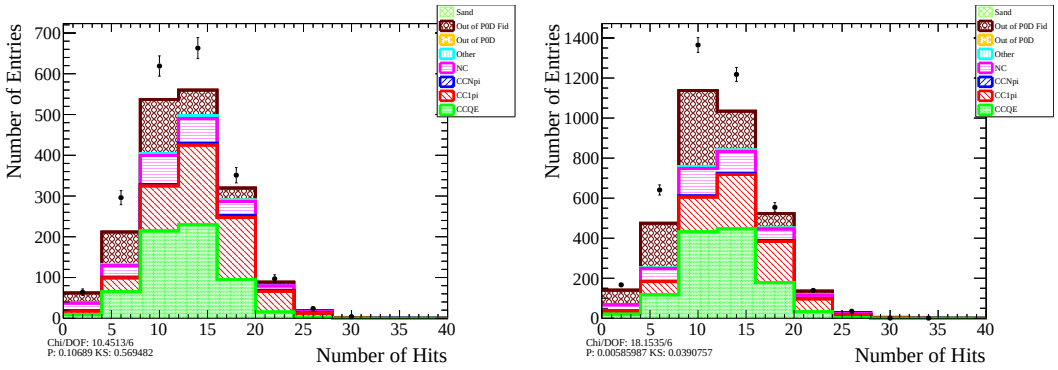

(c) GENIE Water-In

(d) GENIE Water-Out

Figure 5.19: Number of hits nearby the reconstructed vertex for side band events with 2 tracks

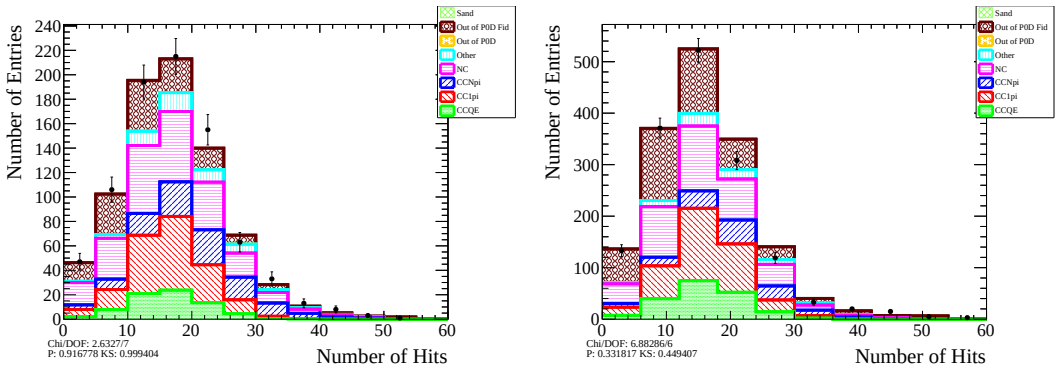

(a) NEUT Water-In

(b) NEUT Water-Out

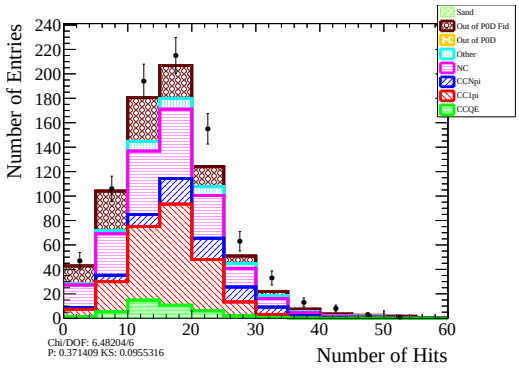

(c) GENIE Water-In

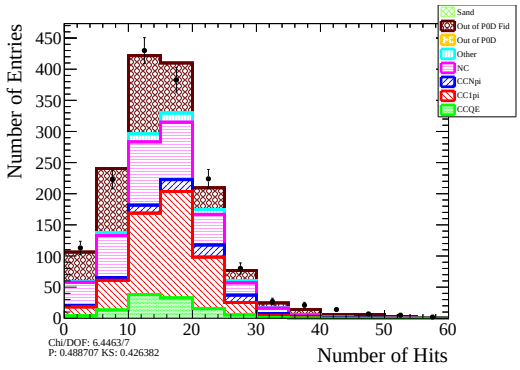

(d) GENIE Water-Out

Figure 5.20: Number of hits nearby the reconstructed vertex for side band events with >2 tracks

In general, we see no consistent Data to Monte Carlo shifts which might represent a detector systematic although the Data and Monte Carlo do not match up exactly. This descrepancy has been noticed by other analysises and has been linked to uncertainties in the neutral current (NC) models or incorrect simulation of certain backgrounds such as neutrons. Another example is that Data and Monte Carlo tend to disagree for the number of hits nearby the vertex for the 1 track sample. However, this discrepancy has been discovered by other analyses and is believed to be an effect of multi-nucleon ejection (np-nh). The Monte Carlo used in this analysis does not simulate multi-nucleon ejection which would result in several very short tracks compared to a single longer track. This effect would be most noticeable with a single track sample because the reconstruction would have difficulty reconstructing these very small tracks which may not deposit enough energy to be detected. As a result, the total number of hits would be expected to be less as these multiple nucleons would be below threshold for detection.

5.12 Data Results

Once the observables are picked with an unbiased fitter and proper binning, then the fit is run over actual data. We set the scaling factor for all initial templates to 1.0. We performed a scan using several different initial values, and found that the final result was insensitive to the choice of initial values. The data is shown in Figures 5.21, 5.22, 5.23, 5.24, and 5.25.

As a general trend, the data and Monte Carlo visually appear similar. Tables C.9, C.10, C.11, and C.12 located in Appendix C show how well the Data and Monte Carlo compare based on a χ^2 test as well as a Kolmogorov Smirnov (KS) test. In Figure 5.23, there is less Data and Monte Carlo for NEUT while GENIE is similar but with a slightly more Monte Carlo. This effect was noticed in previous analyses using NEUT both for cross section measurements and for the oscillation analysis and is largest for a CCQE sample vs a non-CCQE sample.

5.13 Fit Results

The results of the fit are shown in Table 5.7 with the correlation matrix in Figure 5.26. In addition to the scaling factors for the Monte Carlo templates, the Likelihood (L) before

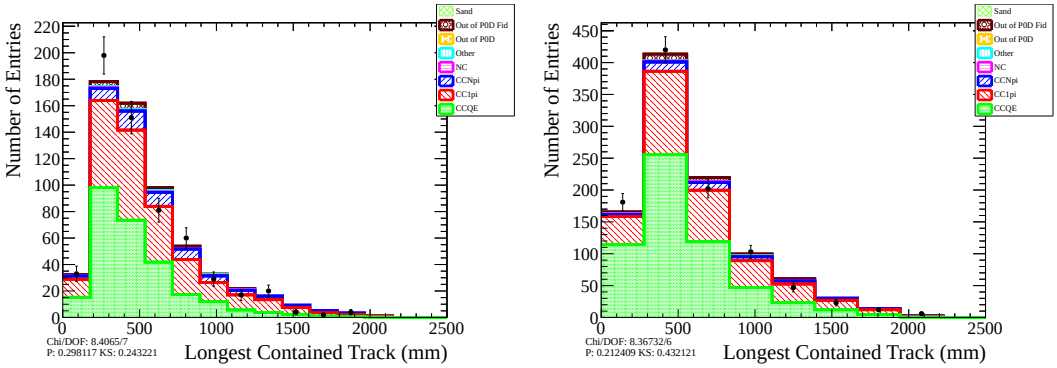

(a) NEUT Water-In

(b) NEUT Water-Out

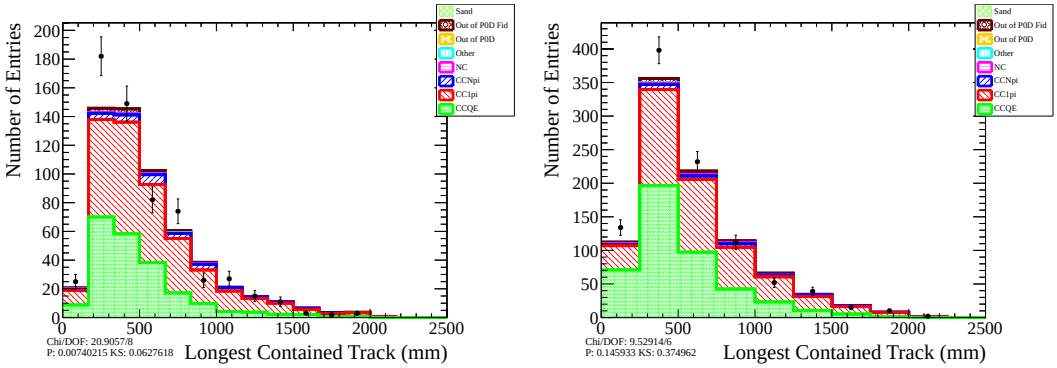

(c) GENIE Water-In

(d) GENIE Water-Out

Figure 5.21: Longest contained track for events with 2 tracks

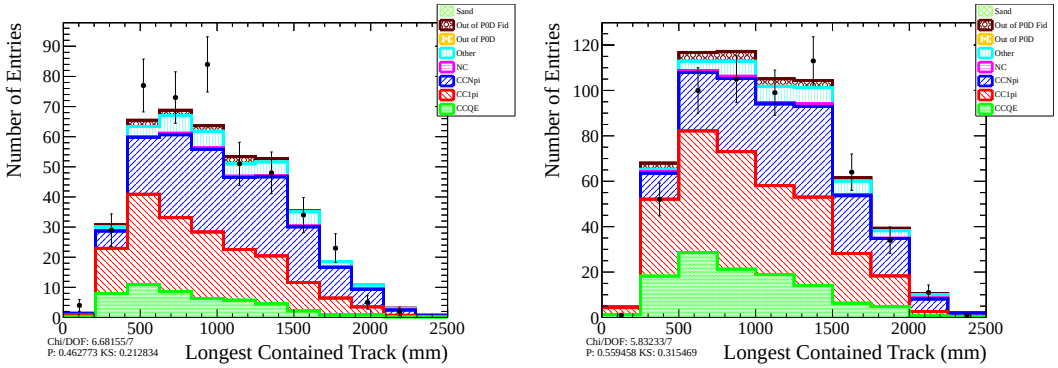

(a) NEUT Water-In

(b) NEUT Water-Out

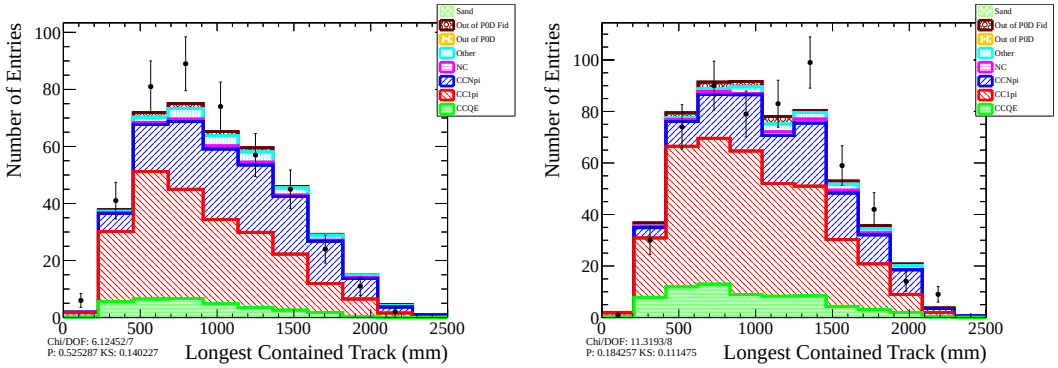

(c) GENIE Water-In

(d) GENIE Water-Out

Figure 5.22: Longest contained track for events with >2 tracks

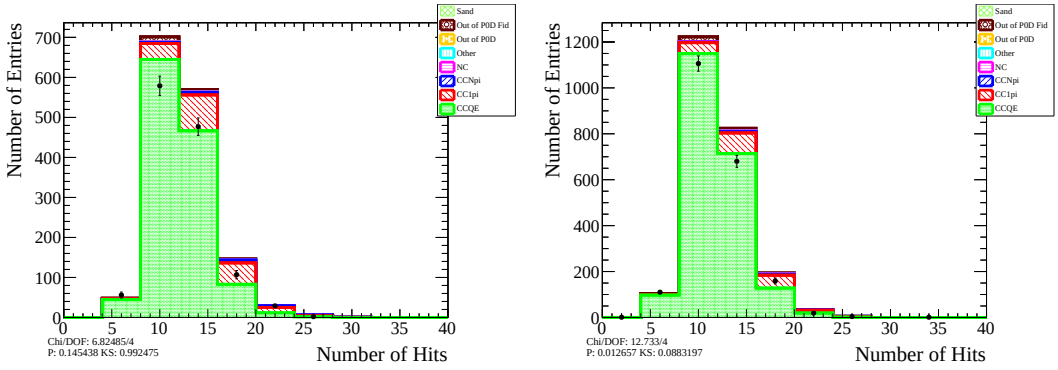

(a) NEUT Water-In

(b) NEUT Water-Out

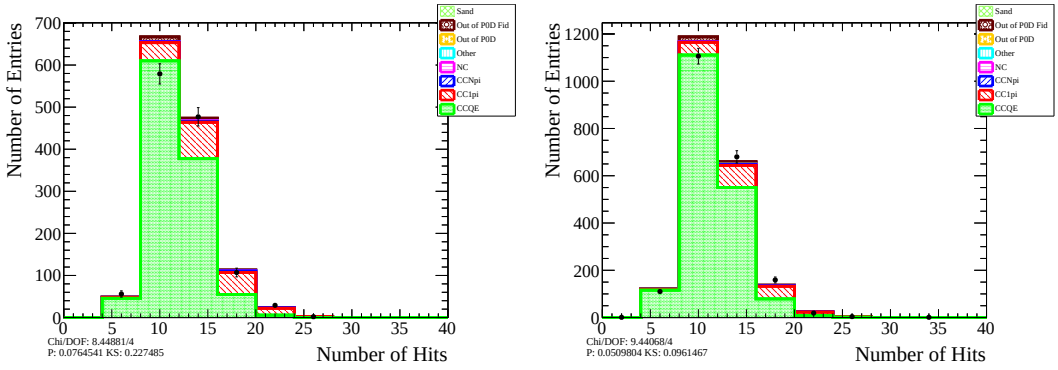

(c) GENIE Water-In

(d) GENIE Water-Out

Figure 5.23: Number of hits nearby the reconstruction vertex for events with 1 track

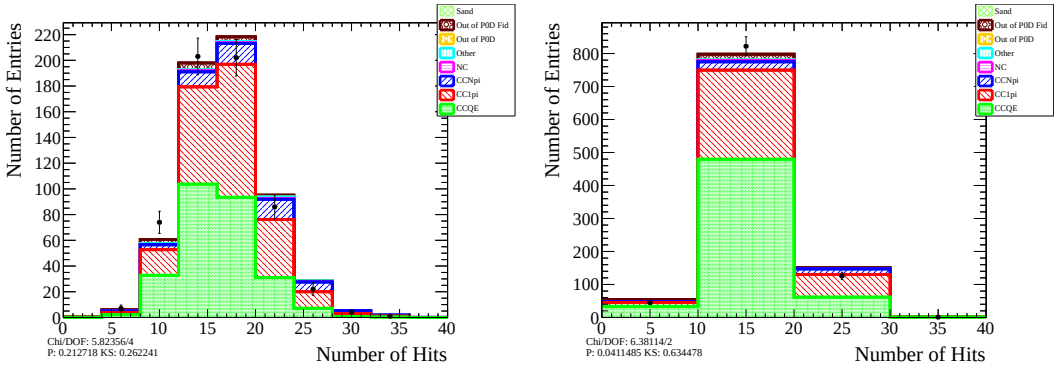

(a) NEUT Water-In

(b) NEUT Water-Out

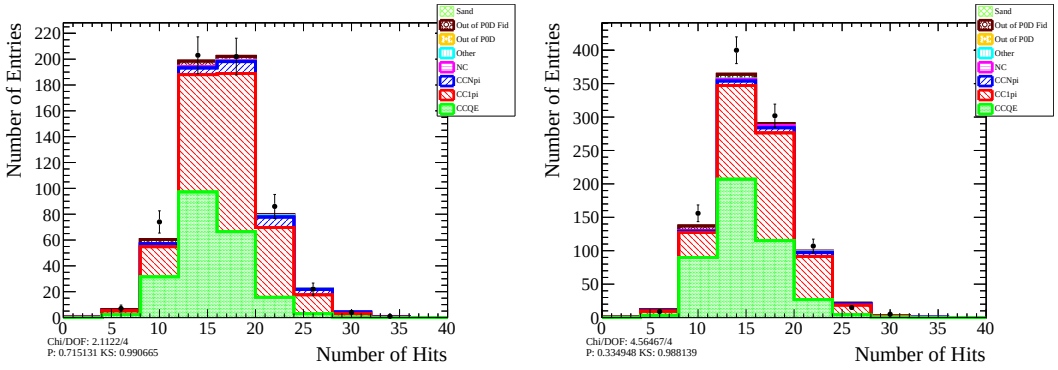

(c) GENIE Water-In

(d) GENIE Water-Out

Figure 5.24: Number of hits nearby the reconstruction vertex for events with 2 tracks

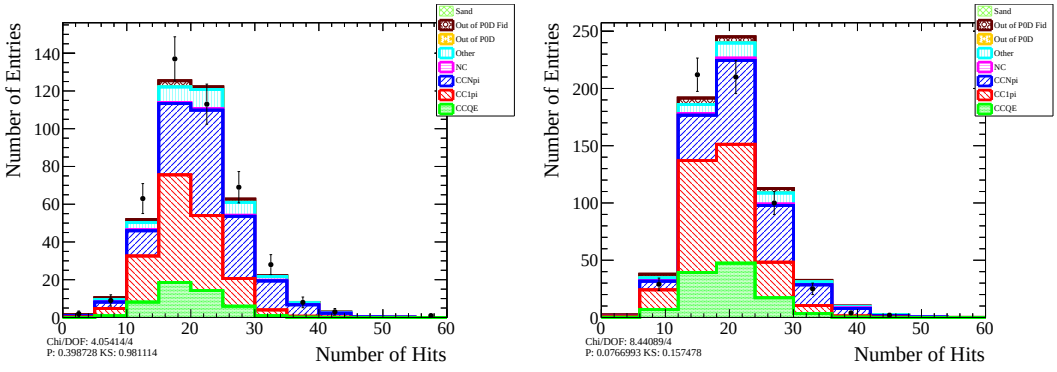

(a) NEUT Water-In

(b) NEUT Water-Out

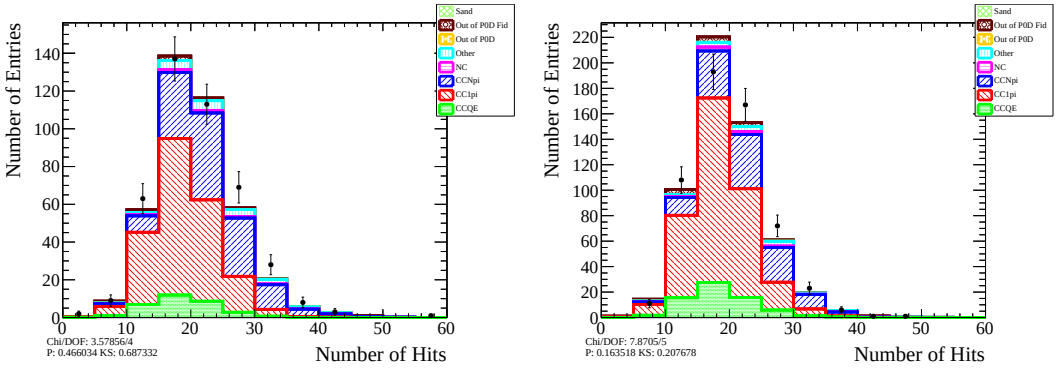

(c) GENIE Water-In

(d) GENIE Water-Out

Figure 5.25: Number of hits nearby the reconstruction vertex for events with >2 tracks

and after the fit is presented as well as the P value using the number of degrees of freedom from Section 5.10. In general, the templates from NEUT are improved by the fit, while the GENIE templates are very slightly improved. The P value is highest for fitted NEUT templates while the fitted GENIE templates still have a poor p value. Using the covariance matrix and the fit uncertainty on the scale factors, we can find the error on $R_{Data/MC}$ using Equation 5.9. The uncertainty depends on the change of $R_{Data/MC}$ while adjusting each scale factor, X_i as well as the error matrix, $Error_{i,j}$.

$$\Delta R_{Data/MC} = \sqrt{\sum_{i,j} \frac{\partial R_{Data/MC}}{\partial X_i} \frac{\partial R_{Data/MC}}{\partial X_j} Error_{ij}} \tag{5.9}$$

	NEUT Water-In	GENIE Water-In	NEUT Water-Out	GENIE Water-Out
R^{CCQE}	0.812±0.034	0.906±0.036	0.882±0.027	0.983±0.028
R^{CC1pi}	1.053±0.100	1.107±0.073	1.036±0.091	1.053±0.066
R^{CCNpi}	0.904±0.178	0.919±0.171	0.758±0.216	1.147±0.203
R^{Other}	1.455±0.628	1.362±0.588	0.958±0.663	0.811±0.522
$R_{Data/MC}$	1.001±0.192	0.934±0.170	0.834±0.233	1.143±0.200
Unfit L/NDof	236/185	235/176	149/108	197/153
Unfit P Value	0.006	0.002	0.005	0.008
Fit L/NDof	199/185	228/176	112/108	195/153
Fit P Value	0.206	0.005	0.357	0.011

Table 5.7: Fit Results

In Table 5.8, we use the results in Table 5.7 to look at the ratio of number of events predicted by NEUT and GENIE after being adjusted with the scaling factors from the fit. Ideally, the type of generator should not be important after being scaled by the data. However, NEUT and GENIE have different templates shapes which may cause the data adjusted number of events to be different due to one generator having a better or worse fit. Overall, most types of events have a ratio of 1.0 within errors, which represents the data

	NEUT/GENIE Water-In	NEUT/GENIE Water-Out
Number of CCQE Events	1.049±0.061	1.056±0.044
Number of CC1pi Events	0.804±0.093	0.824±0.089
Number of CCNpi Events	1.358±0.368	1.002±0.336
Number of Other Events	1.400±0.855	1.597±1.509
Number of CCInc Events	1.002±0.030	1.001±0.023

Table 5.8: Number of specific events in NEUT (adjusted by data) over the number of specific events in GENIE (adjusted by data).

adjusting NEUT and GENIE to the same numbers. This is especially noticable with all CCInc events in which the data adjusted NEUT and GENIE to the same values. However, for both Water-In and Water-Out CC1pi, the NEUT to GENIE ratio is outside the 1σ range for 1.0. This tends to suggest that there is a template shape difference between the NEUT and GENIE CC1pi templates which accounts for more GENIE adjusted events than NEUT.

Using the $R_{Data/MC}$ along with the true CCNpi/CCInc ratio from the Monte Carlo, we can find the adjusted CCNpi/CCInc ratio. This ratio is shown in Table 5.9 and other ratios such as CCQE/CCInc and CC1pi/CCInc are shown in Appendix E. The water-in and water-out adjusted ratios are consistent for both NEUT and GENIE and both water-in and water-out are consistent with each other with just fit errors.

	NEUT Water-In	GENIE Water-In	NEUT Water-Out	GENIE Water-Out
MC	0.126	0.107	0.125	0.106
Data Adjusted	0.126±0.024	0.100±0.018	0.104±0.029	0.121±0.021

Table 5.9: CCNpi/CCInc Ratio using only fit errors.

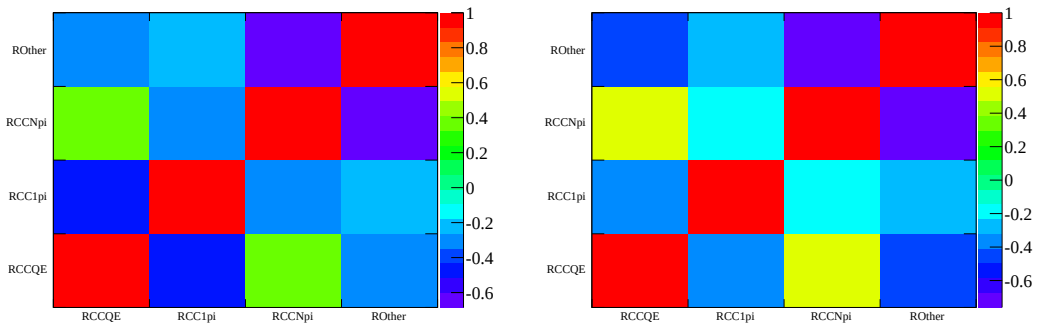

(a) NEUT Water-In

(b) NEUT Water-Out

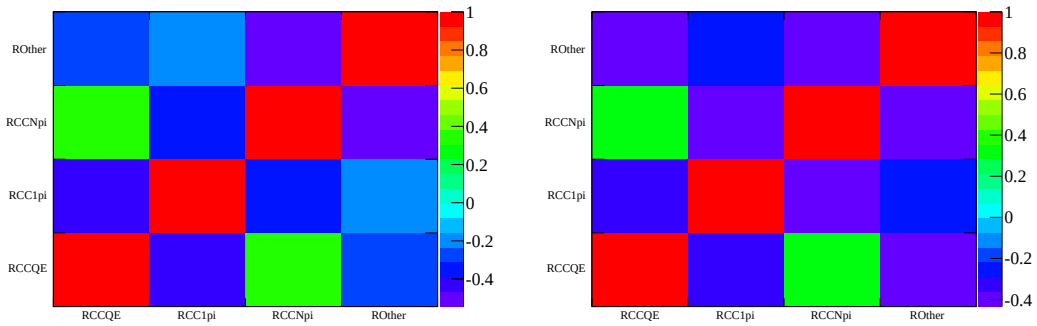

(c) GENIE Water-In

(d) GENIE Water-Out

Figure 5.26: Correlation Matrix.

5.14 Systematics

Systematic errors represent experimental decisions or uncertainty in parameters used in our Monte Carlo models. In general, we would like to determine the systematic uncertainty in two different ways. If possible, we would generate several toy Monte Carlo samples in which a parameter is allowed to vary within its uncertainty, and then look at the distribution of the adjusted CCNpi/CCInc ratio. However, some parameters are computationally intensive or represent threshold values. In that case, we will adjust a parameter by the 1σ equivalent and call the deviation of the new adjusted CCNpi/CCInc ratio from the nominal as the systematic uncertainty for that parameter. However, both of these systematic effects are affected by the overall finite Monte Carlo avaliable.

5.14.1 Finite Monte Carlo

In a perfect world, we would have an extremely large amount of Monte Carlo generated, so that the statistical error in our Monte Carlo templates would be very small. However, we have a finite amount of Monte Carlo available which is approximately 10 times greater than the data. The effect of a finite Monte Carlo samples means that if a parameter is changed, the resulting new CCNpi/CCInc ratio may be only a statistical fluctuation from the Monte Carlo, and not a systematic effect. The obvious solution is to generate more Monte Carlo. However, in our analysis, we are fitting a very diverse sample which makes generating more Monte Carlo difficult without a major production effort. With current computing resources, this could take up to a year to complete.

In order to get an idea of the expected statistical error from just Monte Carlo statistics, we allow the Monte Carlo templates bins to vary based on Poisson statistics, then fit the new template to data and plot a distribution of the new adjusted CCNpi/CCInc ratio. After doing 100,000 throws, the resulting distribution gives us an idea of the overall effect of the limited Monte Carlo. The distributions are shown in Figure 5.27 and the 1σ width of the distribution is shown in Table 5.10.

As a result of the finite Monte Carlo, any change due to changing a systematic could be a result of the statistics of the finite Monte Carlo or a result of the systematic change.

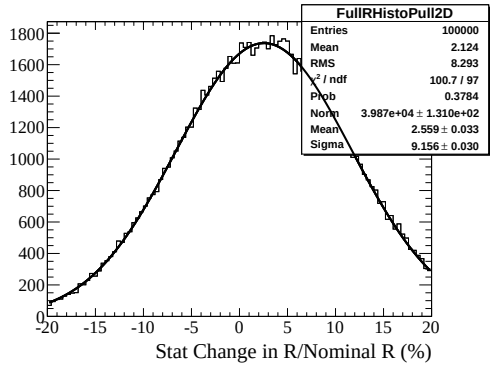

(a) Neut Water-In

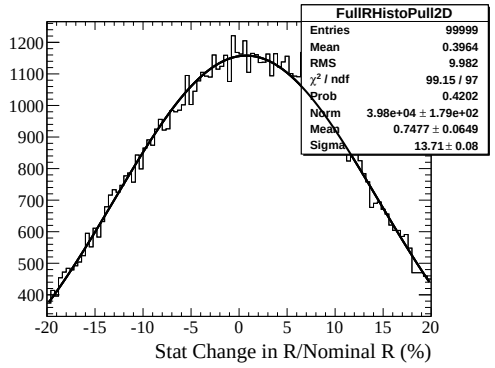

(b) Neut Water-Out

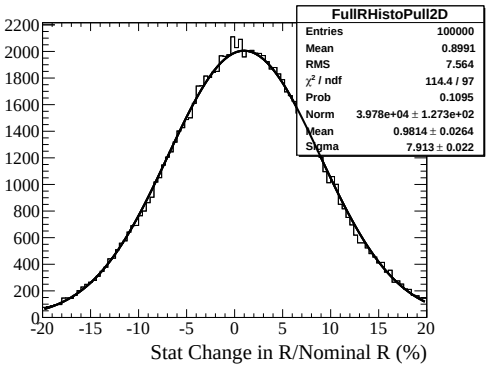

(c) Genie Water-In

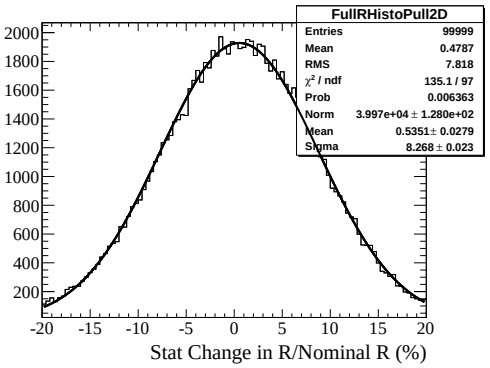

(d) Genie Water-Out

Figure 5.27: Distributions from varying the Monte Carlo template within statistical variation.

	-1σ width	+1σ width
Neut Water-In	-6.53%	11.79%
Genie Water-In	-8.88%	6.91%
Neut Water-Out	-14.39%	12.91%
Genie Water-Out	-8.81%	7.61%

Table 5.10: Monte Carlo statistics error.

Deconvolving these two effects is most easily done by having a large amount of Monte Carlo. Lacking the ability to generate more Monte Carlo in a timely manner, the consensus in the analysis group is to use a conservative approach in which all systematic effects are a combination of systematic variations and Monte Carlo statistics.

5.14.2 Physics Model Effects

As described in Section 5.2, the Monte Carlo physics model is based on several individual models with several parameters built into the models. These parameters can adjust the intrinsic cross section as well change the type and momentum distribution of the ejected particles. Ideally, each parameter in the physics model would be varied and the entire software chain would be rerun. However, this is computationally prohibitive, so a different method was created for the T2K collaboration. A software suite, called T2KReweight, was written to allow for event reweighting.

In event reweighting, the physics model calculations in NEUT or GENIE are preformed using a varied parameter and each event is giving a weight based on if the event would occur more often or less often. For example, if a parameter is changed which would cause the cross section for a particular event to decrease, then a weight less than one would be applied to that event. This procedure allows one to study how changes in the physics model would affect the final result, without needing to rerun the full Monte Carlo simulation and reconstruction. There are some deficiencies to this method, such as being unable to show how parameters such as momentum would change for a single event. However, with a large amount of events, the distributions do tend to change shape because the individual events have a different weight than normal. Also this method is unable to reweight events which do not occur for the nominal parameters, but would occur with the changed parameter.

There are many parameters which can be varied in both NEUT and GENIE as well as some parameters introduced by the T2K Neutrino Interaction Working Group (NIWG) to help match Monte Carlo predictions to data. For the NEUT generator, we have used a select set of parameters that were used for the 2012 ν_e oscillation analysis[4]. These parameters are

[4]TN–113 and TN–108

summarized in Table 5.11. GENIE was not used in the ν_e oscillation analysis, therefore we do not have the same parameters to vary as with NEUT. However, there were some initial studies which established uncertainties[5]. Initial studies using MaCCQE and MaCCRES show that the effect in GENIE appears to be similar to NEUT. As the NIWG parameters exist only for NEUT and are not avaliable for GENIE, we will use the NEUT uncertainity for GENIE.

Only two parameters in the NEUT model are directly varied: namely MaCCQE and MaRES which represent the axial mass used in the cross section model for either the CCQE model or the RES model which results in normalization changes in the cross section as well as changes in the other shape of distributions such as muon momentum. All other parameters represent adjustments to various internal NEUT parameters in order to provide comparisons to external data sets. For example, there are three CCQE normalization parameters which can be changed to allow the overall normalization of CCQE reactions to change within a certain neutrino energy range. There are similar parameters for CC1pi and CC coherent pion reactions. It is important to note that there is a very large error for CC coherent pion reactions because of conflicting reports about the existence of such process. There also exists a normalization parameter for multiple pion interactions, dismpishp. This parameter is not a flat normalization, but is an additional term added to the nominal normalization but inversely scales as the neutrino energy. In other words, the normalization is the nominal plus $\frac{x}{E_\nu}$ in which x corresponds to the parameter adjustment.

In addition, there are two parameters designed to allow fluctuations for the interaction nucleon momentum. On parameter, pf, allows the fermi momentum of the nucleons to vary while the other, sf, is a "switch" that attempts to replace the Fermi gas model of the nucleus with a spectral function model described in Section 5.2. NEUT does not have a spectral function model so a different generator, NuWro was used to establish the proper weights when switching from the Fermi gas to spectral function model.

Finally, there are three other parameters which are used to help match data to Monte Carlo, although the overall physics effects of these parameters are not entirely understood.

---

[5]TN–035

One parameter, DeltaMass, represents a way to adjust the pion momentum distribution from resonance interactions. The phase space distribution multiplied by a Breit-Wigner which is a function of the hadronic invariant mass. The peak is set at 1218 MeV and the width is allowed to vary based on the DeltaMass parameter. The nominal values were determined based on matching Monte Carlo to data. Another parameter, PilessDcy, represents a possible double counting effect in NEUT from π-less Δ decays. In this instance, the parameter represents removing the explicit π-less Δ decay (or Δ re-absorption) from NEUT as there is some data suggesting that the process is already accounted for in other models. In this case, then a -1 σ represents turning off the model to avoid double counting. Finally, the MiniBooNE data[17] suggests a discrepancy between data and Monte Carlo for single pion production. This discrepancy is added as a reweight parameter which changes the normalization of single pion events based on the neutrino energy. This parameter is an empirical function which when turned on will attempt to force data and Monte Carlo to agree with the MiniBooNE data.

In addition to these parameters, NEUT has parameters that can adjust the effect of FSI. Unlike the other parameters, the FSI parameters are not adjusted individually but are all adjusted simultaneously in order to fit external data sources. Base on external data sources, the NIWG has establish a set of 16 adjustments to 6 FSI parameters in order to represent the 1 σ boundary in the FSI space. The adjustments are shown in Table 5.12. The 6 parameters adjust how often pions are absorbed (FSIABS) at low energy, scattered quasi-elastically (FSIQE) at low energy, undergo charge exchange (FSICX) at low energy, quasi-elastic scattering (FSIQEH) at high energy, charge exchange (FSICXH) at high energy, and pion production via inelastic scattering (FSIINEL). In order to find the overall FSI systematic, we will average over the error found by each individual adjustment set as shown in Equation 5.10.

$$\sigma_{FSI} = \sqrt{\frac{1}{16}\sum_{i}^{16}(R_{nom}^{CCNpi/CCInc} - R_{i}^{CCNpi/CCInc})^2} \times \frac{1}{R_{nom}^{CCNpi/CCInc}} \tag{5.10}$$

The results of the Physics Model Reweight are shown in Table 5.13 for the NEUT generator. For the final systematic, we add in quadrature all negative errors for a -1σ

Systematic Changed	Description	Nominal Value	$\pm 1\sigma$
MaCCQE	CCQE Axial Mass	1.21 GeV	16.53%
MaRES	RES Axial Mass	1.21 GeV	16.53%
pf	Fermi Momentum	217 MeV	13.83%
ccqeE0	CCQE $E_\nu < 1.5$ GeV Norm	1.0	11.0%
ccqeE1	CCQE $1.5 < E_\nu < 3.5$ GeV Norm	1.0	30.0%
ccqeE2	CCQE $E_\nu > 3.5$ GeV Norm	1.0	30.0%
cc1piE0	CC1pi $E_\nu < 2.5$ GeV Norm	1.0	21.0%
cc1piE1	CC1pi $E_\nu > 2.5$ GeV Norm	1.0	21.0%
cccohE0	CC Coherent Pion Norm	1.0	100.0%
dismpishp	DIS Shape Change	0	0.4
DeltaMass	Adjust Pion Momentum Shape	87.7 MeV	52.0%
PilessDcy	Δ Re-absorption in Nucleus	0.2	0.2
sf	Use Spectral Function	0	1.0
mbcc1pienushp	Change 1pi E_ν Shape	0	0.5

Table 5.11: NEUT physics model systematic description.

Adj. Set	FSIQE	FSIQEH	FSIINEL	FSIABS	FSICX	FSICXH
Nominal	1.0	1.8	1.0	1.1	1.0	1.8
1	0.6	1.1	1.5	0.7	0.5	2.3
2	0.6	1.1	1.5	0.7	1.6	2.3
3	0.7	1.1	1.5	1.6	0.4	2.3
4	0.7	1.1	1.5	1.6	1.6	2.3
5	1.4	1.1	1.5	0.6	0.6	2.3
6	1.3	1.1	1.5	0.7	1.6	2.3
7	1.5	1.1	1.5	1.5	0.4	2.3
8	1.6	1.1	1.5	1.6	1.6	2.3
9	0.6	2.3	0.5	0.7	0.5	1.3
10	0.6	2.3	0.5	0.7	1.6	1.3
11	0.7	2.3	0.5	1.6	0.4	1.3
12	0.7	2.3	0.5	1.6	1.6	1.3
13	1.4	2.3	0.5	0.6	0.6	1.3
14	1.3	2.3	0.5	0.7	1.6	1.3
15	1.5	2.3	0.5	1.5	0.4	1.3
16	1.6	2.3	0.5	1.6	1.6	1.3

Table 5.12: NEUT FSI adjustments.

and add in quadrature all positive errors for a $+1\sigma$ error. Due to the constraints based on external data fits, there is a correlation between MaRES and some 1pi normalizations[6] which is included in the final error. As noted in Section 5.14.1, this systematic error also includes the effect of finite Monte Carlo systematics. Due to the complexity of removing the finite Monte Carlo effect, we have instead used a conservative approach in which we assume that finite Monte Carlo statistical error is independant for each parameter adjustment. As a result, our systematic error also includes the Monte Carlo statstical error as well.

Systematic Changed	Water-In -1σ	Water-In $+1\sigma$	Water-Out -1σ	Water-Out $+1\sigma$
MaCCQE	-1.73%	1.88%	-9.63%	9.42%
MaRES	4.26%	-4.37%	7.46%	-7.00%
pf	-0.71%	0.78%	-3.73%	4.12%
ccqeE0	3.22%	-2.94%	4.10%	-3.68%
ccqeE1	-4.59%	4.21%	-8.31%	7.77%
ccqeE2	-3.30%	3.11%	-6.80%	6.39%
cc1piE0	-1.44%	1.50%	-5.14%	4.83%
cc1piE1	-0.66%	0.93%	2.79%	-1.94%
cccohE0	-9.27%	8.48%	-14.89%	13.03%
dismpishp	-0.72%	0.46%	1.36%	-1.50%
DeltaMass	-0.56%	0.37%	-1.42%	1.33%
PilessDcy	4.04%	n/a	2.9%	n/a
sf	n/a	0.39%	n/a	-4.55%
mbcc1pienushp	n/a	5.79%	n/a	1.56%
FSI	-10.17%	10.17%	-18.31%	18.31%
Total	-15.90%	16.88%	-29.71%	28.44%

Table 5.13: NEUT physics model and finite Monte Carlo systematic error.

The largest errors for both Water-In and Water-Out tends to be the FSI systematic,

[6] TN–108

which allows event migration between the Monte Carlo templates and would be expected to have a large effect for shape fitting. The Water-Out fit has a much larger error due to MaCCQE than Water-In, but there is a larger percentage of CCQE events since there is less mass in the PØD to help contain CC1pi and CCNpi events. Therefore, adjustments to CCQE have a larger overall effect for Water-Out than Water-In.

The 2nd largest error comes from changing the normalization for CC coherent pion production. This was surprising as the cross section is very small. For example, in the Monte Carlo, coherent pion production makes up roughly 1.5% (2.3% of single pion events) of NEUT interactions or 0.5% (2.3% of single pion events) of GENIE interactions in the PØD fiducial before any cuts are applied. However, after performing the CCInc cuts, the percentage of coherent pion events of single pion events increases to about 14% in NEUT and 4% in GENIE. The remaining cuts increases the percentage to 17% in NEUT Water-In, 19% in NEUT Water-Out, 4% in GENIE Water-In, and 5% in GENIE Water-Out. Based on Figure 5.28, it appears that the muon from a coherent pion event tends to be more energetic and more forward going compared to other single pion events. Therefore, our selection criteria retains coherent pion events while removing other single pion events. As a result, our final samples have a large number of coherent pion events, which results in the sensitivity to changing the overall normalization which changes the overall shape of the CC1pi template as shown in Figure 5.29.

5.14.3 Fiducial Volume Effects

Our fiducial volume definition in X/Y is based on the fiducial volume used for the NCπ^0 analysis in the PØD group. This fiducial volume was defined to avoid edge effects in the detector or reconstruction if a vertex is too close to the edge of the PØD. We will vary this boundary by the detector resolution in to determine if there is any systematic effect from this particular boundary. Based on previous studies in the PØD[7], we will change the fiducial boundary in X and Y by 32 mm independently. We will define the systematic error as the largest positive and negative systematic error as shown in Table 5.14. As with the

[7] TN–131

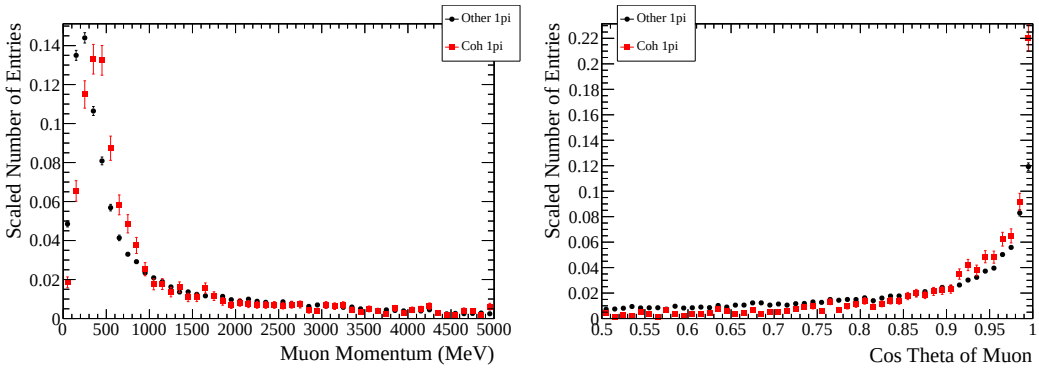

(a) True Muon Momentum (b) True Muon Angle

Figure 5.28: Muon momentum and angle relative to the beam axis in Monte Carlo for Coherent Pion interactions and all other single pion interactions. Plots are normalized to unit area.

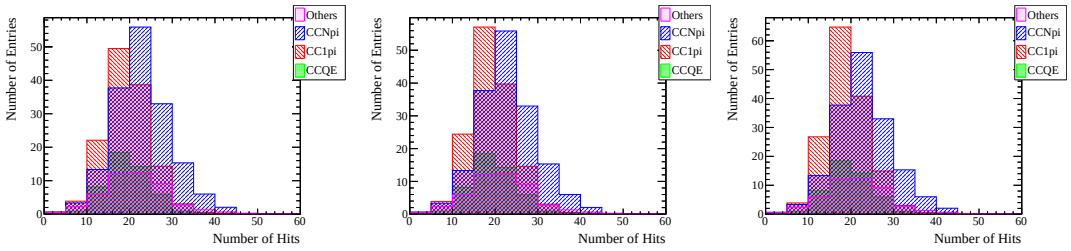

(a) -1σ (b) Nominal (c) $+1\sigma$

Figure 5.29: Effect of changing the coherent pion fraction on the Monte Carlo templates for the number of hits nearby the vertex for the > 2 track sample.

physics model, this error also contains contributions from the Monte Carlo statistical error.

	-1σ Systematic Error	+1σ Systematic Error
Neut Water-In	-5.70%	3.51%
Genie Water-In	-4.92%	3.73%
Neut Water-Out	-14.98%	6.52%
Genie Water-Out	-3.50%	1.42%

Table 5.14: Fiducial volume systematic.

5.14.4 Total Systematics

The total systematic error is shown in Table 5.15. As previously noted, this is not only the systematic effects, but also includes Monte Carlo statistical effects. We have taken a conservative approach to assume that the statistical error is independant in each measurment and is added without any correlations. Because this error includes Monte Carlo statistics, it is expected that the overall systematics error will decrease with more data and more Monte Carlo.

	-1σ Systematic Error	+1σ Systematic Error
Neut Water-In	-16.90%	17.24%
Genie Water-In	-16.65%	17.28%
Neut Water-Out	-33.28%	29.18%
Genie Water-Out	-29.92%	28.48%

Table 5.15: total systematic error.

5.15 Final Results

Using the fit results from Section 5.12 and the systematic errors from Section 5.14, the final measurement is shown in Table 5.16 and Figure 5.30. In order to compare these results

to the previous results mentioned in Section 5.1, we combine all the reported exclusive cross sections together assuming the errors are uncorrelated. As the previous measurements were not an inclusive CCNpi measurement, some interaction modes many not be included in this combination. For the ANL measurements[41], the neutrino energy uncertainty was taken as the average of the 3 exclusive measurements. For the BNL measurements[60], the exclusive measurements were combined based on the largest neutrino uncertainty. In other words, if two exclusive measurements overlap within another measurements neutrino energy uncertainty, all three measurements were added together into a single measurement with the largest neutrino energy uncertainty. In addition, the previous measurements were performed on deuterium and were not a flux inclusive measurement. Finally, our measurement is a relative ratio of CCNpi to CCInc. In order to get a direct cross section, we will multiple our ratio to the T2K CCInc flux integrated measurement[8], to get a direct cross section. The T2K CCInc flux integrated measurement was performed using the Tracker with the FDG being the target. As a result, the CCInc measurement was taken on a similar scintillator target, but does not have a water component. The comparison is shown in Figure 5.31.

	Neut Water-In	Genie Water-In	Neut Water-Out	Genie Water-Out
MC	0.126	0.107	0.125	0.106
Measured	$0.126 \pm 0.024^{+0.022}_{-0.021}$	$0.100 \pm 0.018^{+0.017}_{-0.017}$	$0.104 \pm 0.029^{+0.030}_{-0.035}$	$0.121 \pm 0.021^{+0.034}_{-0.036}$

Table 5.16: Measured CCNpi/CCInc Ratios.

Overall, this measurement is fairly consistent with previous measurements, although the other measurements are not flux integrated which makes a comparison somewhat nebulous. However, there appears to be no large deviations from previous experiments. Due to the large uncertainty in each measurement, it is not possible to distinguish between water-in and water-out measurements just yet, but future measurements made with more data and Monte Carlo should have better sensitivity. Instead, we will report our result not as a water measurement, but a measurement based on the type of target used.

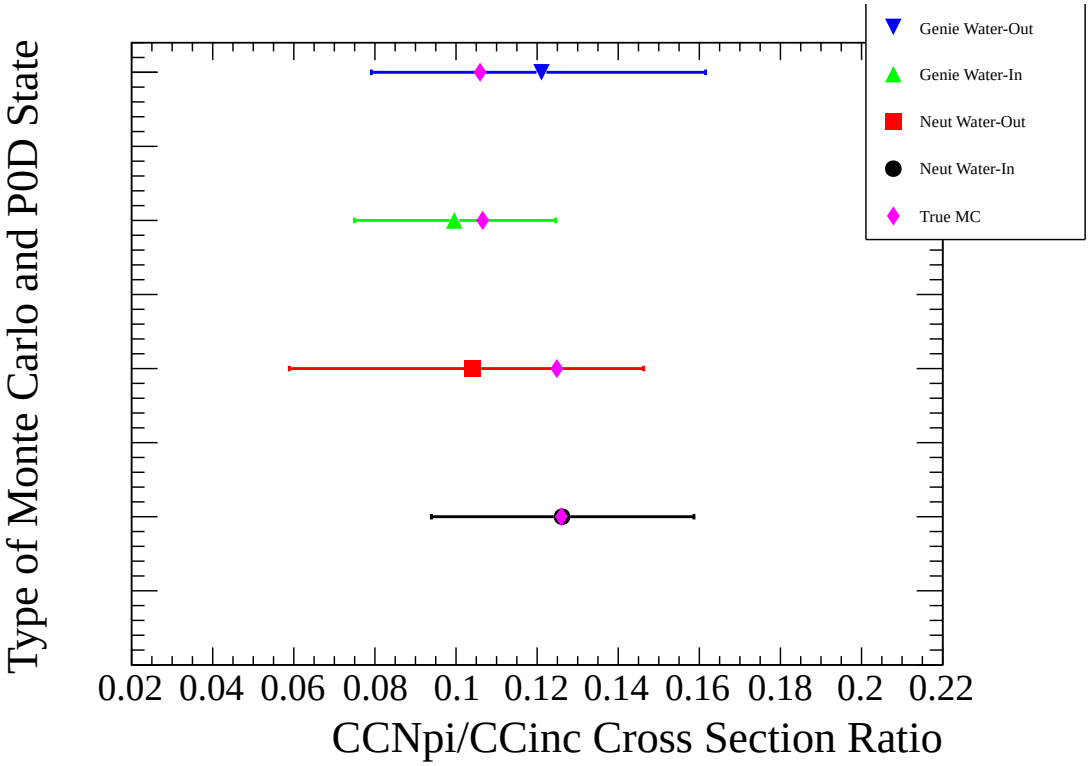

Figure 5.30: Measured CCNpi/CCInc ratio for different Monte Carlo generators.

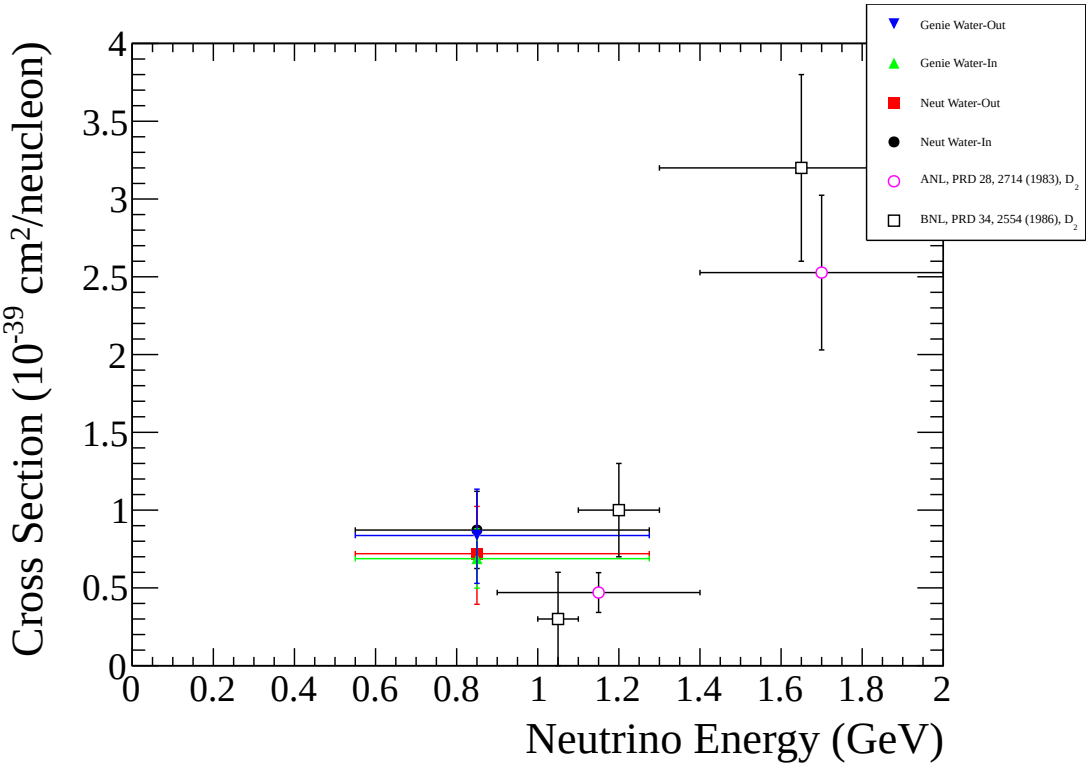

Figure 5.31: Comparison of CCNpi cross section to other measurements. The horizontal error bars for this measurement represent 68% of the flux away from the mean flux (not peak flux). See text for caveats.

Chapter 6

CONCLUSION AND FUTURE PROSPECTS

The discovery of neutrino oscillation has led to several experiments exploring this new area of particle physics. The T2K experiment was designed to produce a ν_μ beam which is relatively narrow in energy. Using Super-Kamiokande as a far detector, one can look for the appearance of ν_es and the disappearance of ν_μs to constrain the probability of oscillation and to look for CP violation in the future.

In order to help minimize the systematic errors on the analysis, the neutrino beam can be measured at a near detector complex to help with flux and Monte Carlo uncertainties. In particular, the PØD component was designed to look for the production of π^0s when neutrinos interact with water. In addition, one could use the PØD and other sub-detectors to look for other neutrino interactions in water.

The PØD was designed as a scintillator detector using triangular polystyrene doped scintillator bars read out use multi-pixel photon detectors (MPPCs). The scintillator layers are interweaved in the center of the PØD with HDPE water bags which are filled using a set of 50 pumps located outside of the PØD. The water bags are monitored using commercial depth sensors and binary level senors which are read out using a custom DAQ and interface software. The monitoring system allows us to measure the mass of water in the PØD to less than 1%.

Using the PØD, we can look at measuring the cross section for processes with and without water. In this thesis, we have measured the relative cross section ratio of charged-current inclusive multiple pion production to inclusive charged-current production from ν_μ. The analysis is preformed using a multi-variate template fit using two Monte Carlo neutrino generators, NEUT and GENIE. The relative ratio for NEUT(GENIE) is $0.126 \pm 0.024^{+0.022}_{-0.021}$($0.100 \pm 0.018^{+0.017}_{-0.017}$) for the Water-In configuration and $0.104 \pm 0.029^{+0.030}_{-0.035}$($0.121 \pm 0.021^{+0.034}_{-0.036}$) for the Water-Out configuration. As mentioned in Section 5.15, we are unable

to do a direct measurment on water using subtraction, but we are able to present our results based on the type of target which was used. At the current uncertainty, we can not determine a large difference between the cross sections measurements with Water-In and Water-Out although there appears to be no large deviation from the NEUT and GENIE Monte Carlo. Because there the relative ratio between the Water-In and Water-Out targets are similar within error, we can infer that either the ratio on water is similar to other heavier nuclei used in the PØD such as carbon within the uncertainty of our measurment.

6.0.1 Future Prospects

As this analysis is statistics limited, it is interesting to estimate the effect of additional data on the overall fit errors and on the finite Monte Carlo. If we were to use additional data and Monte Carlo, the errors associated with each should decrease. To get an estiamte on the effect, we attempted to simulate a larger amount of data and Monte Carlo. To simulate more data, each event in data and Monte Carlo had its weight multiplied by a factor of 5 to represent 5 times more data available. This simulation should account for about 3-4 more years or running assuming that the amount of POT increases with time (as expected). Run 4, which is not included in this analysis, has slightly more POT than runs 1 through 3 combined, so a factor of 5 is reasonable for an analysis in a few years.

	Nominal Fit(%)	5x Fit(%)	Nominal MC (%)	5x MC (%)
Neut Water-In	19.2	8.7	$^{+11.8}_{-6.5}$	$^{+5.73}_{-3.88}$
Genie Water-In	18.2	8.2	$^{+6.9}_{-8.9}$	$^{+4.0}_{-3.3}$
Neut Water-Out	27.9	12.7	$^{+12.9}_{-14.4}$	$^{+8.35}_{-7.39}$
Genie Water-Out	17.5	7.8	$^{+7.6}_{-8.8}$	$^{+3.5}_{-3.9}$

Table 6.1: Effect of 5x POT based on simple scaling.

The results of the scaling for the fit error and finte Monte Carlo are shown in Table 6.1. It is important to note that scaling is just an estimate, because we are assuming that there is no shape change when we have more data and Monte Carlo, which is most likely not

true. Because we have limited statistics to begin with, it is very possible that our current data has fluctuations which will be smoothed out with more actual data and Monte Carlo. However, as a rough estimate, scaling will be sufficent.

With the increase of statistics, it may be possible to do a proper subtraction method. One possible way is to do a similar analysis as outlined here, but instead of fitting Water-In and Water-Out histograms separately one could fit histograms from the subtraction of the two. Appendix B shows some examples. The statistical fluctuations in the subtraction may be small enough for a robust fit with more data. A second method would be to follow other analyses and use a more traditional counting method for an absolute measurement. Such an analysis would most likely still need to use some form of likelihood fit to a set of pdfs in order to get a large purity with reasonable efficency, but such an analysis would improve with more data.

In addition, our method for finding systematics becomes more robust as the amount of Monte Carlo increases. As the Monte Carlo statistical variation decreases, then the systematic shift from our parameter variation becomes more robust and less affected by possible Monte Carlo fluctuations. As a result, our systematic studies will become more independant, and we will have the ability to further identify areas for improvement.

Finally, the neutrino generators and reconstruction software is in constant development with new versions already in existance. Both GENIE and NEUT are refining the physics parameters as well as adding new parameters such as multi-nucleon effects. The new parameters may fit data better and could lead to the removal of other parameters which were introduced simply as empirical corrections resulting in a more robust model. In addition, we were unable to perform GENIE specific systematic variations because the parameters used in NEUT were unavaliable in the reweight package for GENIE. We expect that the reweight package will have more parameters avaliable for GENIE in the future, which will allow the GENIE physics model systematics to be evaluated.

The new reconstruction software could introduce better fitting results, which could result in better identification of short pion tracks resulting in better separation between reactions. The new reconstruction also contains improvements to calibration and detector simulation, which will also help match Monte Carlo to Data. One key improvement that is currently in

testing for the next release is improved matching between sub-detectors. Instead of looking for tracks only in the PØD, we would be able to look for tracks which leave the PØD and are matched well to tracks in other subdetectors such as the ECals and Tracker. If the matching is robust, then a muon candidate may be found from tracks in the surrounding ECals or SMRD, which would vastly increase the acceptance angle for muon candidates. In addition, we currently only accept a vertex in the USWT in order to allow the event to develop within the PØD (see Section 5.7). However, if we can robustly match tracks between subdetectors and use the entire length through several subdetectors, then we are able to accept a vertex which is in the whole Water Target instead of only half. This would increase the avaliable statistics for the analysis as well.

The measurements reported here represent the first measurements of multiple pion production in the PØD, but with additional data and the upcoming software improvements these measurements can be refined with smaller uncertainity. Also, the additonal of more data should allow a subtraction measurement in order to properly measure multiple pion production on water.

Appendix A

UNIT AREA NORMALIZED MONTE CARLO FIT OBSERVABLES

The Monte Carlo templates used to fit to data are described in Section 5.9. In this section, we present the Monte Carlo templates in which each interaction mode is normalized to a unit area in order to show shape differences between each mode.

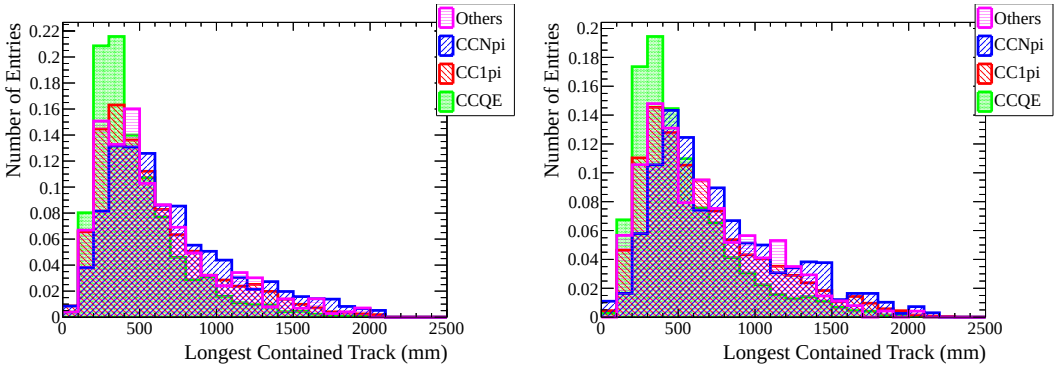

(a) NEUT Water-In

(b) NEUT Water-Out

(c) GENIE Water-In

(d) GENIE Water-Out

Figure A.1: Longest contained track for events with 2 tracks in which all modes are normalized

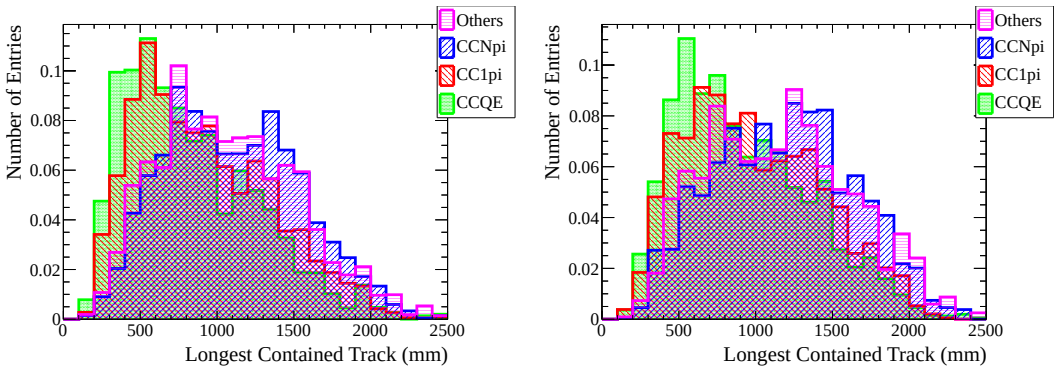

(a) NEUT Water-In

(b) NEUT Water-Out

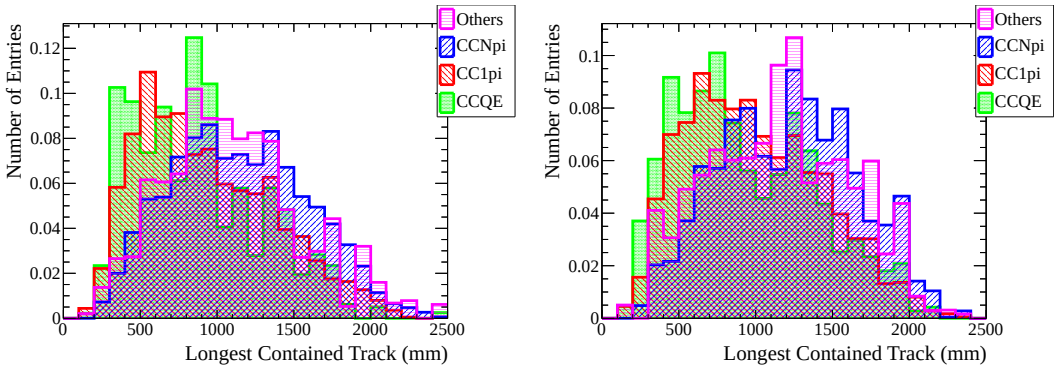

(c) GENIE Water-In

(d) GENIE Water-Out

Figure A.2: Longest contained track for events with >2 tracks in which all modes are normalized

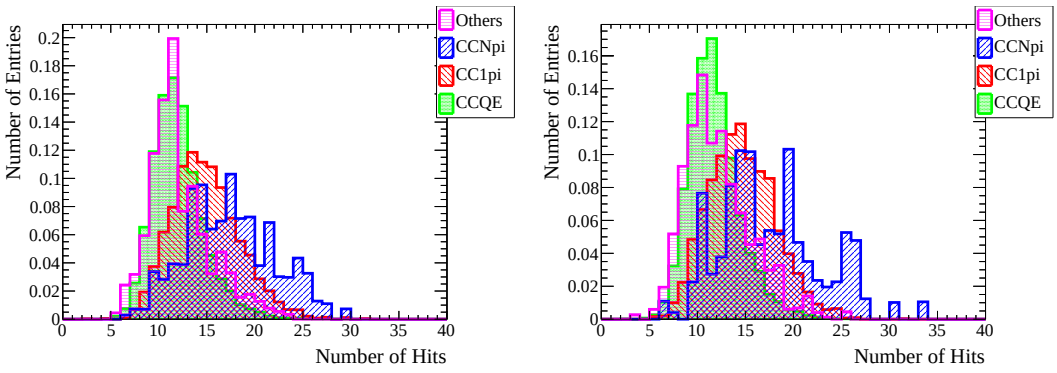

(a) NEUT Water-In

(b) NEUT Water-Out

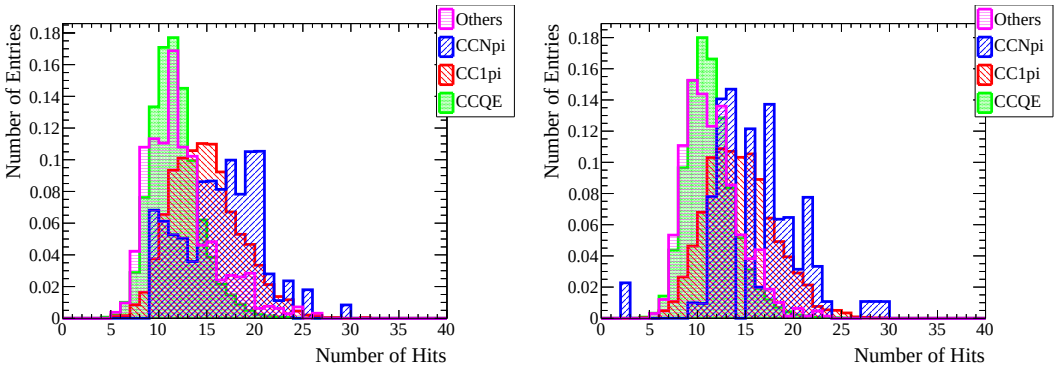

(c) GENIE Water-In

(d) GENIE Water-Out

Figure A.3: Number of hits nearby the reconstruction vertex for events with 1 track in which all modes are normalized

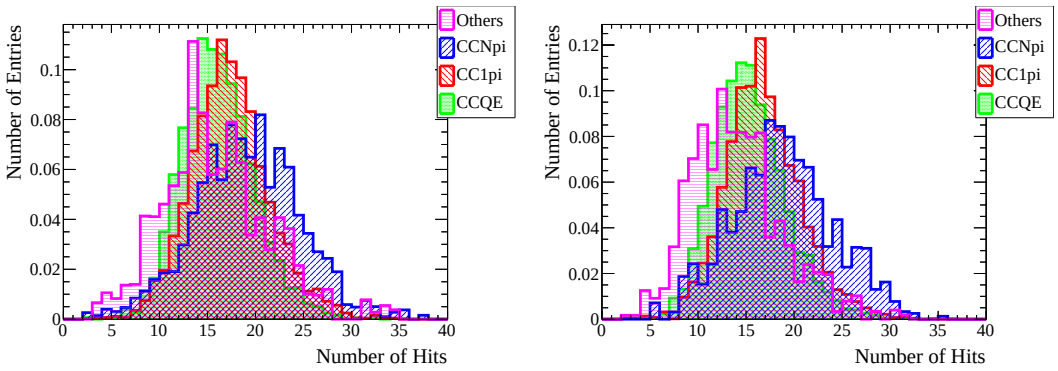

(a) NEUT Water-In

(b) NEUT Water-Out

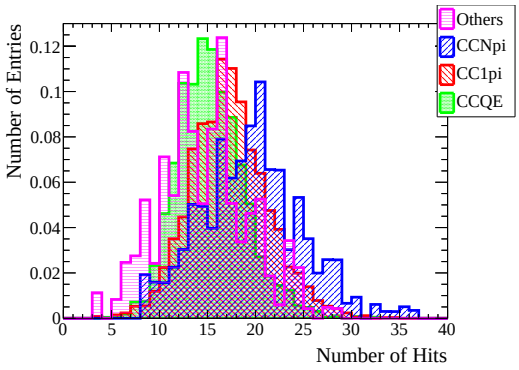

(c) GENIE Water-In

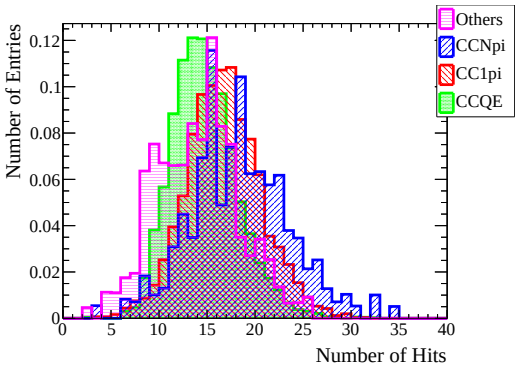

(d) GENIE Water-Out

Figure A.4: Number of hits nearby the reconstruction vertex for events with 2 tracks in which all modes are normalized

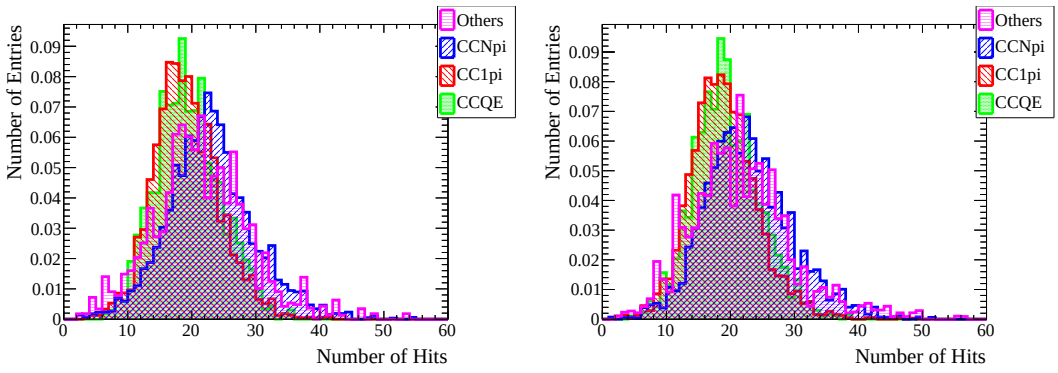

(a) NEUT Water-In

(b) NEUT Water-Out

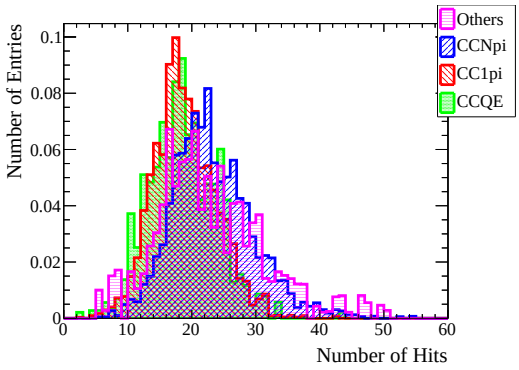

(c) GENIE Water-In

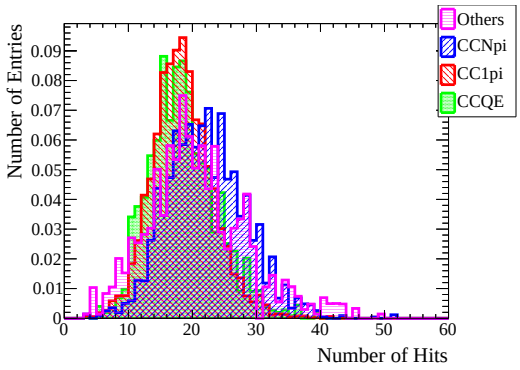

(d) GENIE Water-Out

Figure A.5: Number of hits nearby the reconstruction vertex for events with >2 tracks in which all modes are normalized

Appendix B

WATER-IN MINUS WATER-OUT PLOTS

In our analysis, we fit the Water-In and Water-Out samples separately due to poor statistics. However, with more statistics, it may be possible to fit sample in which the Water-In is subtracted by the Water-Out. These templates should represent the effect from interactions on water if properly scaled for POT. Some example plots are presented below in which we have scaled the Water-Out to match the Water-In POT.

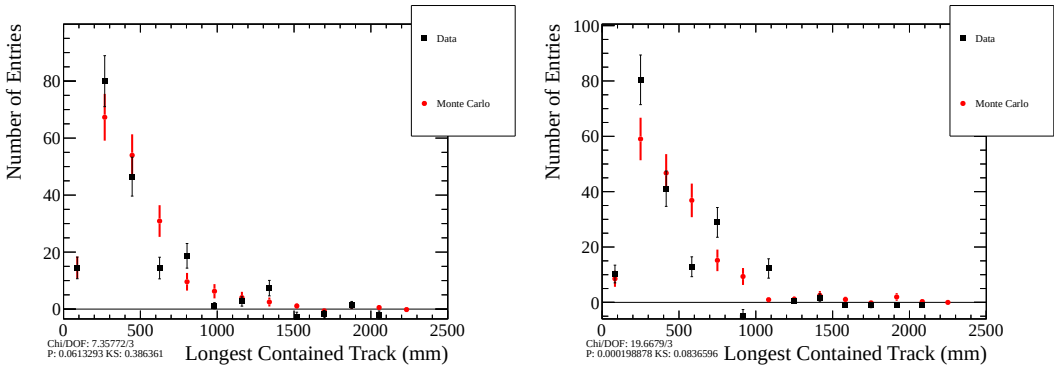

(a) NEUT (b) GENIE

Figure B.1: Longest contained track for events with 2 tracks

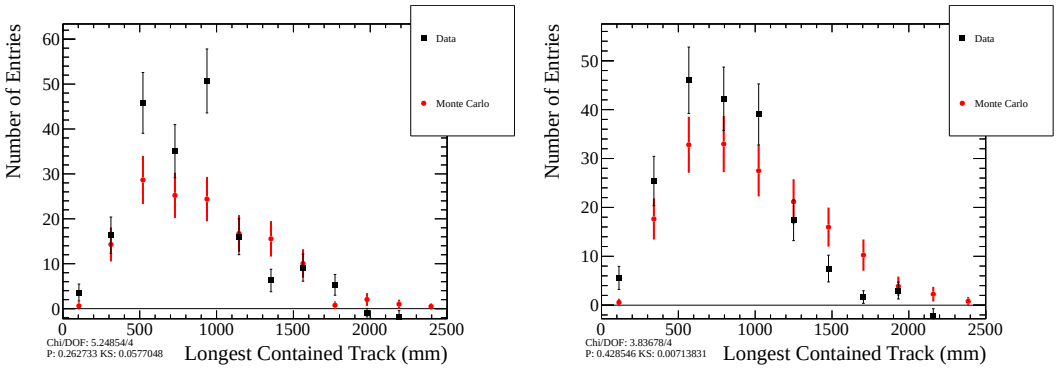

(a) NEUT (b) GENIE

Figure B.2: Longest contained track for events with >2 tracks

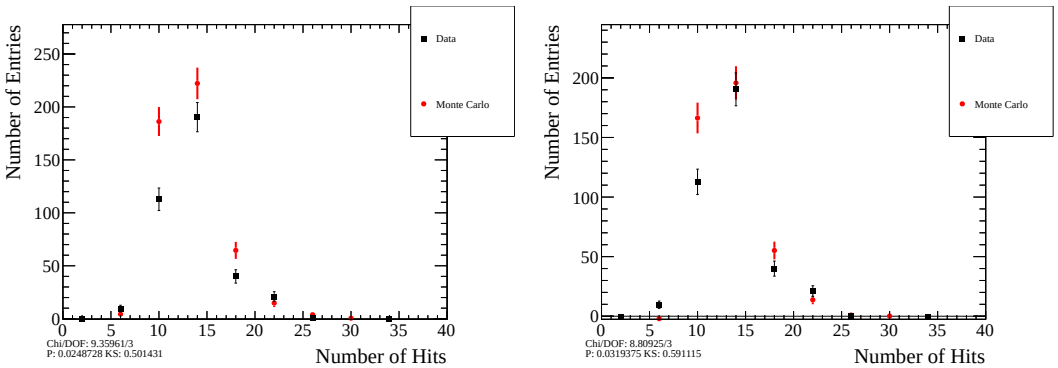

(a) NEUT (b) GENIE

Figure B.3: Number of hits nearby the reconstruction vertex for events with 1 track

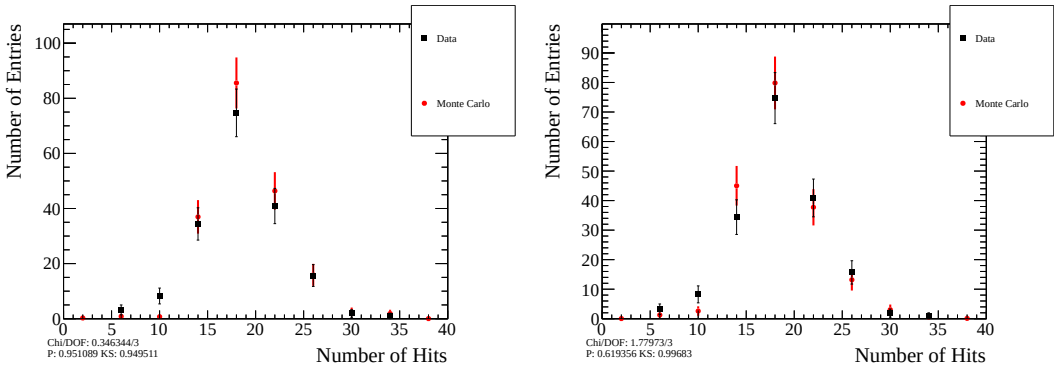

(a) NEUT (b) GENIE

Figure B.4: Number of hits nearby the reconstruction vertex for events with 2 tracks

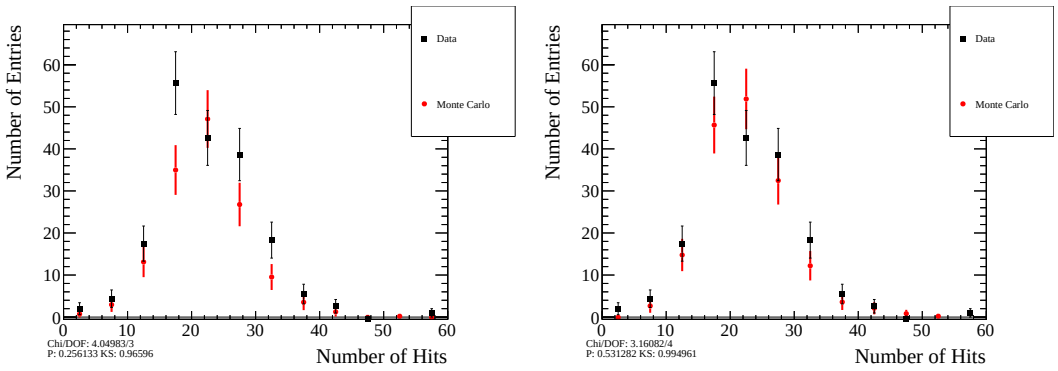

(a) NEUT (b) GENIE

Figure B.5: Number of hits nearby the reconstruction vertex for events with >2 tracks

Appendix C

χ^2 AND KS TESTS

Fit Observable	Sample	χ^2/DoF	P Value	KS Prob
Length	2 tracks	3.02/6	0.806	0.783
Length	>2 tracks	5.57/8	0.695	0.989
Num of Hits	1 track	32.69/5	4.34e-6	1.23e-4
Num of Hits	2 tracks	7.74/6	0.258	0.762
Num of Hits	>2 tracks	2.63/7	0.917	0.999

Table C.1: Data and Monte Carlo comparisons for the NEUT Water-In side band sample

Fit Observable	Sample	χ^2/DoF	P Value	KS Prob
Length	2 tracks	10.09/6	0.121	0.722
Length	>2 tracks	9.02/6	0.172	0.999
Num of Hits	1 track	26.35/5	7.62e-5	2.61e-4
Num of Hits	2 tracks	17.92/6	0.006	0.095
Num of Hits	>2 tracks	10.80/7	0.147	0.607

Table C.2: Data and Monte Carlo comparisons for the NEUT Water-Out side band sample

Fit Observable	Sample	χ^2/DoF	P Value	KS Prob
Length	2 tracks	5.20/6	0.519	0.805
Length	>2 tracks	11.57/7	0.116	0.105
Num of Hits	1 track	22.31/5	4.56e-4	0.003
Num of Hits	2 tracks	10.45/6	0.107	0.569
Num of Hits	>2 tracks	6.48/6	0.371	0.096

Table C.3: Data and Monte Carlo comparisons for the GENIE Water-In side band sample

Fit Observable	Sample	χ^2/DoF	P Value	KS Prob
Length	2 tracks	9.95/6	0.127	0.427
Length	>2 tracks	18.98/8	0.015	0.059
Num of Hits	1 track	27.71/5	4.15e-5	0.004
Num of Hits	2 tracks	18.15/6	0.06	0.039
Num of Hits	>2 tracks	6.45/7	0.489	0.426

Table C.4: Data and Monte Carlo comparisons for the GENIE Water-Out side band sample

Fit Observable	Sample	χ^2/DoF	P Value	KS Prob
Length	2 tracks	8.41/7	0.298	0.243
Length	>2 tracks	6.68/7	0.463	0.213
Num of Hits	1 track	6.82/4	0.145	0.992
Num of Hits	2 tracks	5.82/4	0.213	0.262
Num of Hits	>2 tracks	4.05/4	0.399	0.981

Table C.5: Data and Monte Carlo comparisons for the unfitted NEUT Water-In sample

Fit Observable	Sample	χ^2/DoF	P Value	KS Prob
Length	2 tracks	8.37/6	0.212	0.432
Length	>2 tracks	5.83/7	0.559	0.315
Num of Hits	1 track	12.73/4	0.013	0.088
Num of Hits	2 tracks	6.38/2	0.041	0.634
Num of Hits	>2 tracks	8.44/4	0.077	0.157

Table C.6: Data and Monte Carlo comparisons for the unfitted NEUT Water-Out sample.

Fit Observable	Sample	χ^2/DoF	P Value	KS Prob
Length	2 tracks	20.91/8	0.007	0.063
Length	>2 tracks	6.12/7	0.525	0.140
Num of Hits	1 track	8.45/4	0.076	0.227
Num of Hits	2 tracks	2.11/4	0.715	0.991
Num of Hits	>2 tracks	3.58/4	0.047	0.687

Table C.7: Data and Monte Carlo comparisons for the unfitted GENIE Water-In sample.

Fit Observable	Sample	χ^2/DoF	P Value	KS Prob
Length	2 tracks	9.53/6	0.146	0.375
Length	>2 tracks	11.32/8	0.184	0.111
Num of Hits	1 track	9.44/4	0.051	0.096
Num of Hits	2 tracks	4.56/4	0.335	0.988
Num of Hits	>2 tracks	7.87/5	0.164	0.208

Table C.8: Data and Monte Carlo comparisons for the unfitted GENIE Water-Out sample.

Fit Observable	Sample	χ^2/DoF	P Value	KS Prob
Length	2 tracks	9.54/7	0.216	0.117
Length	>2 tracks	6.56/7	0.477	0.193
Num of Hits	1 track	9.52/4	0.049	0.702
Num of Hits	2 tracks	6.96/4	0.138	0.159
Num of Hits	>2 tracks	3.62/4	0.460	0.999

Table C.9: Data and Monte Carlo comparisons for the fitted NEUT Water-In sample

Fit Observable	Sample	χ^2/DoF	P Value	KS Prob
Length	2 tracks	9.68/6	0.139	0.294
Length	>2 tracks	7.46/6	0.280	0.130
Num of Hits	1 track	15.19/4	0.004	0.039
Num of Hits	2 tracks	6.47/2	0.039	0.584
Num of Hits	>2 tracks	6.76/4	0.149	0.414

Table C.10: Data and Monte Carlo comparisons for the fitted NEUT Water-Out sample.

Fit Observable	Sample	χ^2/DoF	P Value	KS Prob
Length	2 tracks	21.83/8	0.005	0.036
Length	>2 tracks	5.37/7	0.614	0.196
Num of Hits	1 track	6.39/4	0.172	0.710
Num of Hits	2 tracks	2.53/4	0.639	0.980
Num of Hits	>2 tracks	4.10/4	0.393	0.541

Table C.11: Data and Monte Carlo comparisons for the fitted GENIE Water-In sample.

Fit Observable	Sample	χ^2/DoF	P Value	KS Prob
Length	2 tracks	10.49/6	0.105	0.271
Length	>2 tracks	11.07/8	0.198	0.135
Num of Hits	1 track	8.40/4	0.078	0.169
Num of Hits	2 tracks	5.80/4	0.215	0.853
Num of Hits	>2 tracks	7.15/5	0.209	0.293

Table C.12: Data and Monte Carlo comparisons for the fitted GENIE Water-Out sample.

Appendix D

FITTED AND UNFITTED DATA AND MONTE CARLO 2D PLOTS

The Monte Carlo templates fitted to Data in Section 5.8 are a series of two dimensional histograms, with the length of the longest contained track on the x axis and the total number of hits nearby the reconstructed vertex on the y axis. In this appendix, we present the Data histograms as well as the Monte Carlo histograms before and after fitting.

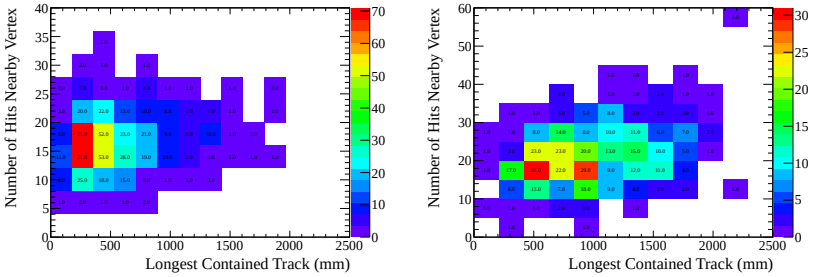

(a) 2 Tracks sample (b) >2 Tracks sample

Figure D.1: Data Water-In

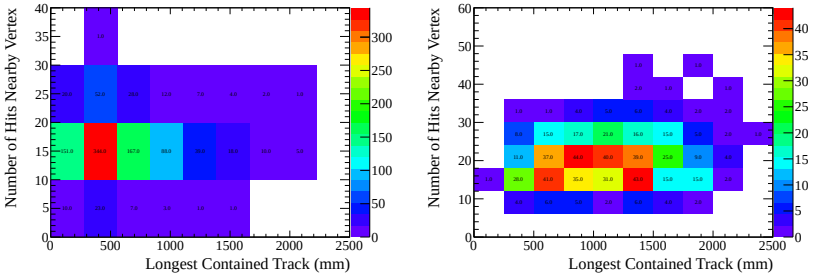

(a) 2 Tracks sample (b) >2 Tracks sample

Figure D.2: Data Water-Out

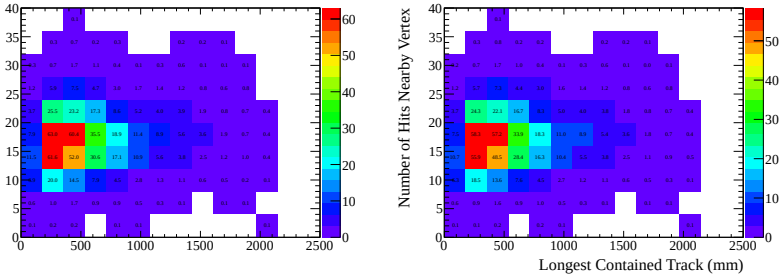

(a) Unfitted (b) Fitted

Figure D.3: NEUT Water-In 2 tracks sample

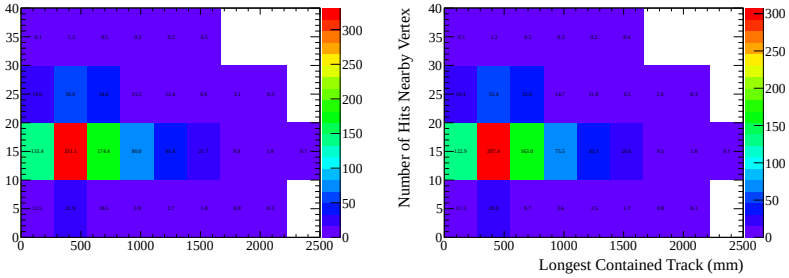

(a) Unfitted (b) Fitted

Figure D.4: NEUT Water-Out 2 tracks sample

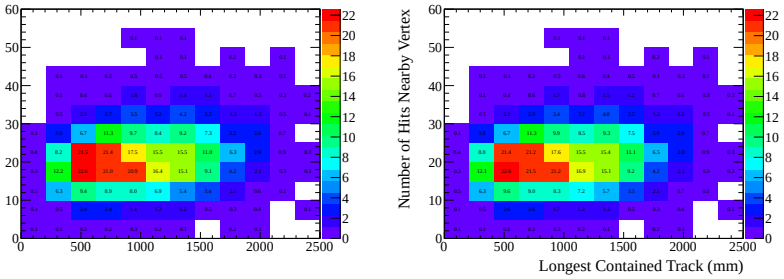

(a) Unfitted (b) Fitted

Figure D.5: NEUT Water-In >2 tracks sample

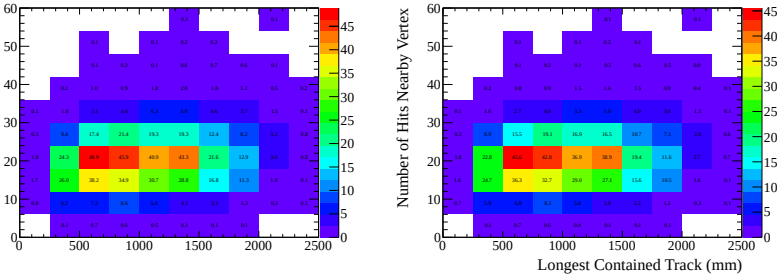

(a) Unfitted (b) Fitted

Figure D.6: NEUT Water-Out >2 tracks sample

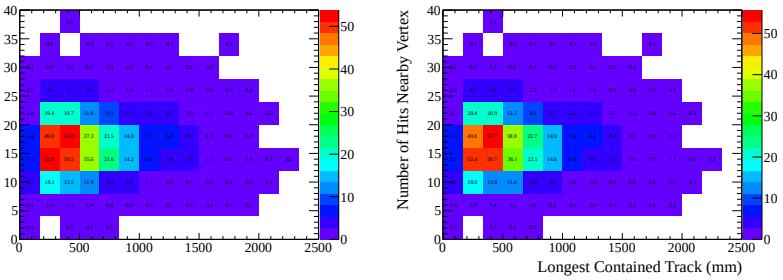

(a) Unfitted (b) Fitted

Figure D.7: GENIE Water-In 2 tracks sample

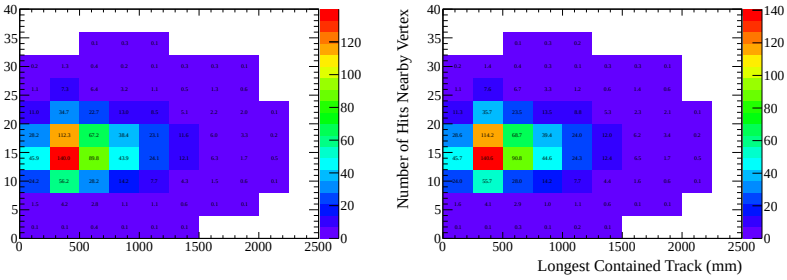

(a) Unfitted (b) Fitted

Figure D.8: GENIE Water-Out 2 tracks sample

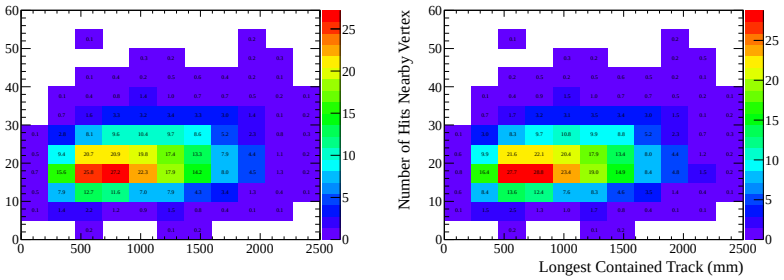

(a) Unfitted (b) Fitted

Figure D.9: GENIE Water-In >2 track sample

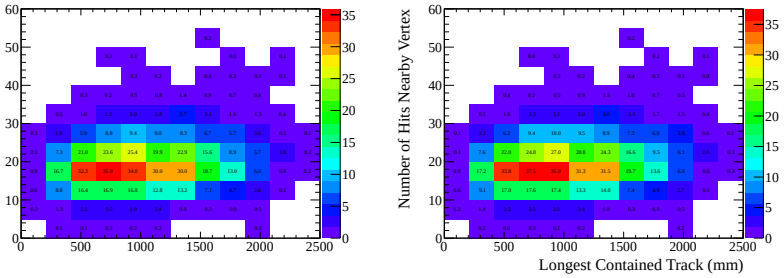

(a) Unfitted (b) Fitted

Figure D.10: GENIE Water-Out >2 track sample

Appendix E

CCQE/CCINC AND CC1PI/CCINC ADJUSTED RATIO

Because we are fitting CCQE and CC1pi templates, we could measure the ratio of CCQE/CCInc as well as the ratio of CC1pi/CCInc. As this analysis was designed to look for the more difficult CCNpi/CCInc ratio, it is not optimized to measure these other ratios, but we will present the results with only fit errors and no systematic studies.

	Neut Water-In	Genie Water-In	Neut Water-Out	Genie Water-Out
MC CCQE/CCInc	0.614	0.563	0.622	0.569
Adjusted CCQE/CCInc	0.552±0.020	0.514±0.017	0.604±0.015	0.557±0.013
MC CC1pi/CCInc	0.215	0.297	0.208	0.291
Adjusted CC1pi/CCInc	0.250±0.023	0.334±0.020	0.237±0.020	0.305±0.018

Table E.1: CCQE/CCInc and CC1pi/CCInc Ratios using only Fit Errors.

As seen in Table E.1, the CCQE/CCInc ratios are fairly consistent between Water-In and Water-Out, even without considereing systematic errors. The CC1pi/CCInc ratios are not consistent within fit errors, but may be with systematic errors.

Appendix F

BEST REWEIGHT FIT

A higher ΔP Value represents a better fit while a higher $\Delta(-2lnL)$ represents an increase in $-2lnL$ corresponding to a worse fit.

Overall, the fit is worse with FSI variations, tends not prefer the spectral function model used in T2KReweight. The Water-Out sample has larger changes in likelihood which tends to prefer coherent pion production over no coherent pion production, and keeping Pionless Δ decay.

Systematic Changed	$\Delta(-2lnL)(-1\sigma)$	$\Delta(-2lnL)(+1\sigma)$	ΔP Value(-1σ)%	ΔP Value$(+1\sigma)$%
MaCCQE	2.99	-1.82	-23.00%	16.42%
MaRES	1.63	-0.38	-35.21%	33.96%
pf	1.19	-0.99	-0.99%	8.68%
ccqeE0	1.97	-1.29	-23.46%	11.48%
ccqeE1	0.58	0.07	-4.81%	-9.33%
ccqeE2	-1.31	1.81	11.64%	-14.50%
cc1piE0	0.11	0.25	-9.64%	-2.13%
cc1piE1	-0.38	0.85	-14.19%	11.35%
cccohE0	0.278	1.78	6.89%	-5.89%
dismpishp	-0.35	0.42	-6.03%	15.43%
DeltaMass	-0.20	0.13	1.72%	18.12%
PilessDcy	-0.55	n/a	4.72%	n/a
sf	n/a	3.88	n/a	-28.98%
mbcc1pienushp	n/a	1.54	n/a	5.16%
FSI 1/2	8.14	11.66	-61.91%	-66.80%
FSI 3/4	3.9	7.49	-53.15%	-59.31%
FSI 5/6	8.15	0	-69.73%	-24.69%
FSI 7/8	2.77	13.30	-52.95%	-89.77%
FSI 9/10	-4.14	1.59	18.25%	-20.77%
FSI 11/12	-1.70	-0.92	-12.30%	-1.27%
FSI 13/14	4.46	5.02	-50.65%	-42.32%
FSI 15/16	5.15	10.13	-53.88%	-72.45%

Table F.1: Change in $-2lnL$ and P Value with physics model systematic for NEUT Water-In.

Systematic Changed	$\Delta(-2lnL)(-1\sigma)$	$\Delta(-2lnL)(+1\sigma)$	ΔP Value(-1σ)%	ΔP Value$(+1\sigma)$%
MaCCQE	3.32	-1.57	-23.80%	12.53%
MaRES	-0.41	0.34	3.21%	5.45%
pf	0.99	-0.27	-15.05%	-5.85%
ccqeE0	3.48	-2.24	-24.83%	26.85%
ccqeE1	-1.41	2.35	11.21%	-17.24%
ccqeE2	-2.16	2.88	17.45%	-20.84%
cc1piE0	-1.26	1.57	10.03%	-11.74%
cc1piE1	-2.25	2.45	18.24%	-17.96%
cccohE0	16.49	-7.46	-80.51%	55.72%
dismpishp	-0.40	0.50	3.15%	-3.81%
DeltaMass	0.23	-0.19	-1.80%	1.45%
PilessDcy	3.95	n/a	-27.85%	n/a
sf	n/a	12.65	n/a	-69.65%
mbcc1pienushp	n/a	3.96	n/a	-21.09%
FSI 1/2	6.96	6.57	-50.74%	-48.82%
FSI 3/4	9.40	8.10	-57.09%	-56.08%
FSI 5/6	1.99	0.00	-21.92%	-7.89%
FSI 7/8	10.02	6.68	-64.08%	-54.55%
FSI 9/10	-1.21	1.21	9.57%	-9.15%
FSI 11/12	5.38	4.45	-42.60%	-37.34%
FSI 13/14	-2.66	-0.50	13.01%	3.93%
FSI 15/16	8.638	4.82	229.05%	-45.30%

Table F.2: Change in $-2lnL$ and P Value with physics model systematic for NEUT Water-Out.

Appendix G

VARYING RECONSTRUCTION PARAMETERS

For most cross section analysies, a change in reconstruction parameters may make small changes in the total number of events in Monte Carlo and data, but should have a fairly small systematic effect since hopefully the reconstruction treats data and Monte Carlo equally. However, it is difficult to find the appropriate amount to vary the reconstruction parameters because they are often tuned in a way in which there is no real 1 σ variation possible. A good example the number of layers to skip in the track reconstruction. Changing the parameter from 1 to 2 to 3 may not demonstrate a true 1 σ variation but may instead just simply lead to back reconstruction effects.

In addition, in order to test the reconstruction parameters, we could not use the full Monte Carlo set due to the amount of time needed to reprocess the Monte Carlo. This smaller Monte Carlo sample would have a much larger statistical error which would dominate the analysis. Therefore, we do not include a true reconstruction systematic error to our analysis. However, we will provide the effects of vary the parameters slightly for reference.

For the reconstruction systematic, we have concentrated on the road following algorithm used for track reconstruction. This algorithm uses seed coming from a Hough transform and then adds hits by following a "road" from the seeds. The new track is then fit by either a Kalman fit or a parametric fit as described in Section 5.4. By changing parameters in the road following algorithm, we can change the number of tracks which appear which can cause event migration between the 1, 2, or >2 track samples. If this migration is not the same between data and Monte Carlo or changes then Monte Carlo templates extensively, then there may be a large systematic error in the final result.

The road following algorithm has three parameters we will concentrate: the road width, the road angle, and number of skipped layers. The road width defines how many bars in a single later the algorithm looks for hits, the road angle defines a maximum scattering

angle allowed, and the number of skipped layers defines how many layers the algorithm can skip before finding another hit to add to the track. Based on conversations within the PØD group, a deviation of 25% for the road width and angle and a deviation of 1 layer for the skipped layers was used. The best way to evaluate this systematic was to change the parameters by the uncertainty, then rerun the Reconstruction code. As this process if very computationally intensive, it was only done for the data for Run 1 and 2, with water in the PØD and only for a smaller section of NEUT Monte Carlo corresponding to 3 times the amount of data available. The effects are shown in Table G.1.

Parameter	Nominal Value	Variation	-1σ	$+1\sigma$
Road Width	80 mm	$\pm$20 mm	13.14%	10.12%
Road Angle	0.55 rad	$\pm$0.125 rad	-5.33%	6.62%
Number of Layers	2	$\pm$1	11.26%	8.07%
Total	n/a	n/a	-5.33%	18.52%

Table G.1: Reconstruction Effect

In order to examine the large systematic effect from the reconstruction systematics, we will examine the difference between the nominal analysis and each parameter alteration. In general, changing the reconstruction parameters changes the overall normalization after out cuts by about 1% but has a larger effect between samples. The migration between bins in Data and Monte Carlo is shown in TableG.2 with the largest changes in the > 2 track sample except for setting the number of skipped layers to 1 in the data vs Monte Carlo.

As the fitter is attempting to match Monte Carlo to Data, if a change in the reconstruction affects Data more than Monte Carlo, that may lead to variations from the Monte Carlo which could appear to be changes in the templates. However, it is possible that changes in reconstruction may also cause a worse fit, which would make the fit results suspect. Therefore, we report the fit parameters and likelihood in Table G.3.

Reducing the road width makes a significantly worse fit and increasing the road width and varying the road angle tends to make a slightly worse fit. Changing the number of layers

Parameter	Sample Type	1 Track	2 Track	> 2 Track
60mm Width	MC	-1.6%	2.2%	8.9%
60mm Width	Data	-1.4%	3.0%	5.7%
100mm Width	MC	0.1%	0.2%	-3.8%
100mm Width	Data	0.1%	-0.2%	-6.9%
0.425 Angle	MC	0.1%	0.5%	4.0%
0.425 Angle	Data	-0.1%	0.0%	0.2%
0.675 Angle	MC	0.1%	-0.7%	-0.8%
0.675 Angle	Data	0.2%	-0.3%	-4.4%
1 Layer	MC	0.1%	1.3%	16.3%
1 Layer	Data	-11.6%	1.0%	13.1%
3 Layers	MC	0.1%	-1.3%	-8.4%
3 Layers	Data	0.0%	-1.2%	-6.0%

Table G.2: Change in number of events in each sample after changing a reconstruction parameter.

	60mm Width	100mm Width	0.4125 angle	0.6875 angle	1 layer	3 layers
RCCQE	0.855	0.846	0.843	0.836	0.723	0.841
RCC1pi	1.039	1.080	1.057	1.141	1.121	1.073
RCCNpi	1.122	1.085	0.943	1.054	1.032	1.079
ROther	0.912	0.737	1.262	0.620	0.520	1.210
Likelihood	491	374	381	361	355	336

Table G.3: Fit parameters based on reconstruction variations.

tends to make a slightly better fit. The worse fits tends to suggest that the separation power with the Monte Carlo templates is reduced in efficiency or that the Monte Carlo template shapes are not matching the Data well. This is reinforced by the fitter as changing the reconstruction parameters results in a large variation between the scaling for the CCNpi template and Other template. In effect, the shape difference between the CCNpi and Other templates are not robust with respect to reconstruction parameters. Because the overall event rate is not changed significantly by changing the reconstruction parameters, this effect would be reduced in a measurement which counts events instead of template fitting.

Appendix H

SYSTEMATIC STUDIES USING MONTE CARLO TEMPLATE VARIATION

In this appendix, we will attempt to examine the effect of Monte Carlo template variations on the systematics shown in Section 5.14. In this case, we will vary a paramter as previously in order to establish a new Monte Carlo templates. Then, similar to Section 5.14.1, we will allow the new templates to vary within the Monte Carlo statistical error before scaling to match data POT. We repeat this procedure 10,000 times and plot the resulting $R_{Data/MC}$. In this case, we will assume the systematic error is the deviation of the mean of the distribution from the mean of the nominal result. By using the mean, we are attempting to use the most probable value for our systematic although the true systematic is within the actual distrubution.

Systematic Changed	Water-In -1σ	Water-In +1σ	Water-Out -1σ	Water-Out +1σ
MaCCQE	-1.18%	1.57%	-7.35%	7.69%
MaRES	4.90%	-5.17%	8.16%	-7.50%
pf	-0.45%	0.57%	-2.98%	3.57%
ccqeE0	3.39%	-2.85%	4.54%	-3.70%
ccqeE1	-4.72%	4.47%	-7.87%	7.42%
ccqeE2	-3.52%	2.42%	-6.68%	6.20%
cc1piE0	-1.15%	1.28%	-3.95%	4.30%
cc1piE1	-0.32%	0.79%	2.76%	-1.75%
cccohE0	-8.56%	8.33%	-12.92%	12.60%
dismpishp	-0.99%	0.79%	0.95%	-1.16%
DeltaMass	-0.23%	0.33%	-0.89%	0.79%
PilessDcy	3.12%	n/a	3.28%	n/a
sf	n/a	1.81%	n/a	-1.73%
mbcc1pienushp	n/a	5.60%	n/a	2.02%
FSI	-8.92%	8.92%	-14.46%	14.46%
Total	-14.99%	16.02%	-25.02%	25.31%

Table H.1: NEUT physics model systematic error using distribution mean.

	-1σ Systematic Error	+1σ Systematic Error
Neut Water-In	-4.50%	2.80%
Genie Water-In	-4.92%	3.73%
Neut Water-Out	-8.09%	5.63%
Genie Water-Out	-3.50%	1.42%

Table H.2: Fiducial volume systematic using distribution mean.

	-1σ Systematic Error	+1σ Systematic Error
Neut Water-In	-15.65%	16.26%
Genie Water-In	-15.14%	16.37%
Neut Water-Out	-26.30%	25.92%
Genie Water-Out	-25.17%	25.33%

Table H.3: Total systematic error using distribution mean.

BIBLIOGRAPHY

[1] MINERvA Technical Design Report. 2006.

[2] K. Abe, T. Abe, H. Aihara, Y. Fukuda, Y. Hayato, et al. Letter of Intent: The Hyper-Kamiokande Experiment — Detector Design and Physics Potential —. 2011. arXiv:1109.3262 [hep-ex].

[3] K. Abe et al. Indication of Electron Neutrino Appearance from an Accelerator-produced Off-axis Muon Neutrino Beam. *Phys.Rev.Lett.*, 107:041801, 2011.

[4] K. Abe et al. The T2K Experiment. *Nucl.Instrum.Meth.*, A659:106–135, 2011.

[5] K. Abe et al. First Muon-Neutrino Disappearance Study with an Off-Axis Beam. *Phys.Rev.*, D85:031103, 2012.

[6] K. Abe et al. Evidence of Electron Neutrino Appearance in a Muon Neutrino Beam. *Phys.Rev.*, D88:032002, 2013.

[7] K. Abe et al. Measurement of neutrino oscillation parameters from muon neutrino disappearance with an off-axis beam. *Phys. Rev. Lett.*, 111:211803, Nov 2013.

[8] K. Abe et al. Measurement of the Inclusive NuMu Charged Current Cross Section on Carbon in the Near Detector of the T2K Experiment. *Phys.Rev.*, D87:092003, 2013.

[9] K. Abe et al. Observation of Electron Neutrino Appearance in a Muon Neutrino Beam. *Phys.Rev.Lett.*, 112:061802, 2013.

[10] K. Abe et al. The T2K Neutrino Flux Prediction. *Phys.Rev.*, D87:012001, 2013.

[11] N Abgrall et al. Measurements of Cross Sections and Charged Pion Spectra in Proton-Carbon Interactions at 31 GeV/c. *Phys.Rev.*, C84:034604, 2011.

[12] N. Abgrall et al. Time Projection Chambers for the T2K Near Detectors. *Nucl.Instrum.Meth.*, A637:25–46, 2011.

[13] P. Adamson et al. Measurement of the neutrino mass splitting and flavor mixing by MINOS. *Phys.Rev.Lett.*, 106:181801, 2011.

[14] S. Agostinelli et al. GEANT4: A Simulation toolkit. *Nucl.Instrum.Meth.*, A506:250–303, 2003.

[15] A.A. Aguilar-Arevalo et al. Bringing the SciBar detector to the booster neutrino beam. 2006. arXiv:0601022 [hep-ex].

[16] A.A. Aguilar-Arevalo et al. The MiniBooNE Detector. *Nucl.Instrum.Meth.*, A599:28–46, 2009.

[17] A.A. Aguilar-Arevalo et al. Measurement of Neutrino-Induced Charged-Current Charged Pion Production Cross Sections on Mineral Oil at Enu 1 GeV. *Phys.Rev.*, D83:052007, 2011.

[18] Q.R. Ahmad et al. Measurement of the rate of nu/e + d to p + p + e- interactions produced by B-8 solar neutrinos at the Sudbury Neutrino Observatory. *Phys.Rev.Lett.*, 87:071301, 2001.

[19] J.K. Ahn et al. Observation of Reactor Electron Antineutrino Disappearance in the RENO Experiment. *Phys.Rev.Lett.*, 108:191802, 2012.

[20] J. Altegoer et al. The NOMAD experiment at the CERN SPS. *Nucl.Instrum.Meth.*, A404:96–128, 1998.

[21] P.-A. Amaudruz. The T2K Fine-Grained Detectors. *Nucl.Instrum.Meth.*, A696:1–31, 2012.

[22] I. Ambats et al. The MINOS Detectors Technical Design Report. 1998.

[23] F.P. An et al. Observation of electron-antineutrino disappearance at Daya Bay. *Phys.Rev.Lett.*, 108:171803, 2012.

[24] Analog Devices. 8-Channel, 10- and 12-Bit ADCs with I2C-Compatible Interface in 20-Lead TSSOP. `http://www.analog.com`.

[25] C. Anderson, M. Antonello, B. Baller, T. Bolton, C. Bromberg, et al. The ArgoNeuT Detector in the NuMI Low-Energy beam line at Fermilab. *JINST*, 7:P10019, 2012.

[26] C. Andreopoulos, A. Bell, D. Bhattacharya, F. Cavanna, J. Dobson, et al. The GENIE Neutrino Monte Carlo Generator. *Nucl.Instrum.Meth.*, A614:87–104, 2010.

[27] S. Aoki, G. Barr, M. Batkiewicz, J. Blocki, J.D. Brinson, et al. The T2K Side Muon Range Detector. *Nucl.Instrum.Meth.*, A698:135–146, 2013.

[28] G. Arnison et al. Experimental Observation of Isolated Large Transverse Energy Electrons with Associated Missing Energy at s**(1/2) = 540-GeV. *Phys.Lett.*, B122:103–116, 1983.

[29] G. Arnison et al. Experimental Observation of Lepton Pairs of Invariant Mass Around 95-GeV/c**2 at the CERN SPS Collider. *Phys.Lett.*, B126:398–410, 1983.

[30] S. Assylbekov, G. Barr, B.E. Berger, H. Berns, D. Beznosko, et al. The T2K ND280 Off-Axis Pi-Zero Detector. *Nucl.Instrum.Meth.*, A686:48–63, 2012.

[31] D.S. Ayres et al. NOvA: Proposal to build a 30 kiloton off-axis detector to study nu(mu) to nu(e) oscillations in the NuMI beamline. 2004. arXiv:0503053 [hep-ex].

[32] J. Beringer et al. Review of particle physics. *Phys. Rev. D*, 86:010001, Jul 2012.

[33] Dmitriy Beznosko. Novel Multi-pixel Silicon Photon Detectors and Applications in T2K. 2009. arXiv:0910.4429 [physics.ins-det].

[34] A Bodek and U.K. Yang. Higher twist, xi(omega) scaling, and effective LO PDFs for lepton scattering in the few GeV region. *J.Phys.*, G29:1899–1906, 2003.

[35] R. Brun and F. Rademakers. ROOT: An object oriented data analysis framework. *Nucl.Instrum.Meth.*, A389:81–86, 1997.

[36] B.T. Cleveland, Timothy Daily, Jr. Davis, Raymond, James R. Distel, Kenneth Lande, et al. Measurement of the solar electron neutrino flux with the Homestake chlorine detector. *Astrophys.J.*, 496:505–526, 1998.

[37] C.L. Cowan, F. Reines, F.B. Harrison, H.W. Kruse, and A.D. McGuire. Detection of the free neutrino: A Confirmation. *Science*, 124:103–104, 1956.

[38] G. Danby, J.M. Gaillard, Konstantin A. Goulianos, L.M. Lederman, Nari B. Mistry, et al. Observation of High-Energy Neutrino Reactions and the Existence of Two Kinds of Neutrinos. *Phys.Rev.Lett.*, 9:36–44, 1962.

[39] Jr. Davis, Raymond, Don S. Harmer, and Kenneth C. Hoffman. Search for neutrinos from the sun. *Phys.Rev.Lett.*, 20:1205–1209, 1968.

[40] R. Davis. Solar neutrinos. II: Experimental. *Phys.Rev.Lett.*, 12:303–305, 1964.

[41] D. Day, R. Ammar, D. Coppage, R. Davis, N. Kwak, et al. Study of neutrino D charged current two pion production in the threshold region. *Phys.Rev.*, D28:2714–2720, 1983.

[42] E. Eskut et al. The CHORUS experiment to search for muon-neutrino to tau-neutrino oscillation. *Nucl.Instrum.Meth.*, A401:7–44, 1997.

[43] Gary J. Feldman and Robert D. Cousins. A Unified approach to the classical statistical analysis of small signals. *Phys.Rev.*, D57:3873–3889, 1998.

[44] E. Fermi. An attempt of a theory of beta radiation. 1. *Z.Phys.*, 88:161–177, 1934.

[45] Alfredo Ferrari, Paola R. Sala, Alberto Fasso, and Johannes Ranft. FLUKA: A multi-particle transport code (Program version 2005). 2005.

[46] J. A. Formaggio and G. P. Zeller. From ev to eev: Neutrino cross sections across energy scales. *Rev. Mod. Phys.*, 84:1307–1341, Sep 2012.

[47] Y. Fukuda et al. Evidence for oscillation of atmospheric neutrinos. *Phys.Rev.Lett.*, 81:1562–1567, 1998.

[48] Y. Fukuda et al. The Super-Kamiokande detector. *Nucl.Instrum.Meth.*, A501:418–462, 2003.

[49] I. Giomataris, R. De Oliveira, S. Andriamonje, S. Aune, G. Charpak, et al. Micromegas in a bulk. *Nucl.Instrum.Meth.*, A560:405–408, 2006.

[50] Global Water Inc. The WL400 Water Level Sensor. `http://www.globalw.com`.

[51] M. Gluck, E. Reya, and A. Vogt. Dynamical parton distributions revisited. *Eur.Phys.J.*, C5:461–470, 1998.

[52] Richard Gran. K2K cross section results. *Nucl.Phys.Proc.Suppl.*, 221:98–102, 2011.

[53] Kaoru Hagiwara, Takayuki Kiwanami, Naotoshi Okamura, and Ken-ichi Senda. Physics potential of neutrino oscillation experiment with a far detector in Oki Island along the T2K baseline. *JHEP*, 1306:036, 2013.

[54] D.A. Harris et al. Neutrino scattering uncertainties and their role in long baseline oscillation experiments. 2004. arXiv:0410005 [hep-ex].

[55] Mark Hartz. Commissioning of the T2K Beamline. *AIP Conf.Proc.*, 1222:327–331, 2010.

[56] Y. Hayato. NEUT. *Nucl.Phys.Proc.Suppl.*, 112:171–176, 2002.

[57] Atsuko K. Ichikawa. Status of the T2K long baseline neutrino oscillation experiment. *J.Phys.Conf.Ser.*, 203:012104, 2010.

[58] F. James and M. Roos. Minuit: A System for Function Minimization and Analysis of the Parameter Errors and Correlations. *Comput.Phys.Commun.*, 10:343–367, 1975.

[59] Jean-Luc Biord. QDevelop : Free cross-platform Development Environment for Qt4. `http://biord-software.org/qdevelop/`, 2013.

[60] T. Kitagaki, H. Yuta, S. Tanaka, A. Yamaguchi, K. Abe, et al. Charged current exclusive pion production in neutrino deuterium interactions. *Phys.Rev.*, D34:2554–2565, 1986.

[61] L. Bellantoni, P. Rubinov. Bench test of first Trip-T prototypes. `https://plone4.fnal.gov/P1/AFEIIUpgrade/tript/`, 2005.

[62] C.H. Llewellyn Smith. Neutrino Reactions at Accelerator Energies. *Phys.Rept.*, 3:261–379, 1972.

[63] Ziro Maki, Masami Nakagawa, and Shoichi Sakata. Remarks on the unified model of elementary particles. *Prog.Theor.Phys.*, 28:870–880, 1962.

[64] Kevin Scott McFarland. MINERvA: A Dedicated neutrino scattering experiment at NuMI. *Nucl.Phys.Proc.Suppl.*, 159:107–112, 2006.

[65] S.P. Mikheyev and A. Yu. Smirnov. Resonant neutrino oscillations in matter. *Prog.Part.Nucl.Phys.*, 23:41–136, 1989.

[66] Omega, Inc. Low Flow Polypropylene and TFE Liquid Flowmeters. `http://www.omega.com/ppt/pptsc.asp?ref=FPR301_302_303_304&Nav=gref06`, 2013.

[67] Yuichi Oyama. K2K (KEK to Kamioka) neutrino - oscillation experiment at KEK PS. 1998. arXiv:9803014 [hep-ex].

[68] B. Pontecorvo. Mesonium and anti-mesonium. *Sov.Phys.JETP*, 6:429, 1957.

[69] B. Pontecorvo. Neutrino Experiments and the Problem of Conservation of Leptonic Charge. *Sov.Phys.JETP*, 26:984–988, 1968.

[70] Dieter Rein and Lalit M. Sehgal. Neutrino Excitation of Baryon Resonances and Single Pion Production. *Annals Phys.*, 133:79–153, 1981.

[71] Dieter Rein and Lalit M. Sehgal. Coherent pi0 Production in Neutrino Reactions. *Nucl.Phys.*, B223:29, 1983.

[72] D. Renker and E. Lorenz. Advances in solid state photon detectors. *JINST*, 4:P04004, 2009.

[73] S. Ritt, P. Amaudruz, K. Olchanski. MIDAS (Maximum Integration Data Acquisition System). `http://midas.psi.ch`, 2001.

[74] Tetsuro Sekiguchi. Neutrino beamline for T2K. *AIP Conf.Proc.*, 981:275–277, 2008.

[75] Torbjorn Sjostrand, Patrik Eden, Christer Friberg, Leif Lonnblad, Gabriela Miu, et al. High-energy physics event generation with PYTHIA 6.1. *Comput.Phys.Commun.*, 135:238–259, 2001.

[76] Roman Tacik. The T2K near detectors. *AIP Conf.Proc.*, 1405:237–242, 2011.

[77] Trolltech. Qt Designer Manual. `http://qt-project.org/doc/qt-4.8/designer-manual.html`, 2013.

[78] Trolltech. Qt Project. `http://qt-project.org/`, 2013.

[79] M. Tzanov et al. Precise measurement of neutrino and anti-neutrino differential cross sections. *Phys.Rev.*, D74:012008, 2006.

[80] Uwe Rathmann and Josef Wilgen. Qwt User's Guide. `http://qwt.sourceforge.net/index.html`, 2013.

[81] R. Wendell et al. Atmospheric neutrino oscillation analysis with sub-leading effects in Super-Kamiokande I, II, and III. *Phys.Rev.*, D81:092004, 2010.

[82] L. Wolfenstein. Neutrino Oscillations in Matter. *Phys.Rev.*, D17:2369–2374, 1978.